



Horizon 2020  
Programme

**CORTEX**

*Research and Innovation Action (RIA)*

This project has received funding from the European Union's Horizon 2020 research and innovation programme under grant agreement No 754316.

Start date : 2017-09-01 Duration : 48 Months  
<http://cortex-h2020.eu>



---

**Final validation report**

---

Authors : Mr. Paolo VINAI (Chalmers), Klemen AMBROZIC (EPFL), Alberto BRIGHENTI (CEA), Christophe DEMAZIÈRE (CHALMERS), Baptiste GASSE (CEA), Damian GINESTAR (UPV), Mathieu HURSIN (EPFL), Sebastian HÜBNER (TUD), Alexander KNOSPE (TUD), Vincent LAMIRAND (EPFL), Carsten LANGE (TUD), Axel LAUREAU (EPFL), Rafael MACIAN (TUM), Antonios MYLONAKIS (CHALMERS), Oskari PAKARI (EPFL), Adolfo RAIS (EPFL), Amélie ROUCHON (CEA), Simone SANTANDREA (CEA), Zarko STANKOVSKI (CEA), Gumersindo VERDÚ (UPV), Antoni VIDAL-FERRÀNDIZ (UPV), Toshihiro YAMAMOTO (KyotoU), Huaqian YI (CHALMERS), Soobeen YUM (TUM), Igor ZMIJAREVIC (CEA), Andrea ZOIA (CEA)

CORTEX - Contract Number: 754316

Project officer: Marco Carbini

Document title	Final validation report
Author(s)	Mr. Paolo VINAI, Klemen AMBROZIC (EPFL), Alberto BRIGHENTI (CEA), Christophe DEMAZIÈRE (CHALMERS), Baptiste GASSE (CEA), Damian GINESTAR (UPV), Mathieu HURSIN (EPFL), Sebastian HÜBNER (TUD), Alexander KNOSPE (TUD), Vincent LAMIRAND (EPFL), Carsten LANGE (TUD), Axel LAUREAU (EPFL), Rafael MACIAN (TUM), Antonios MYLONAKIS (CHALMERS), Oskari PAKARI (EPFL), Adolfo RAIS (EPFL), Amélie ROUCHON (CEA), Simone SANTANDREA (CEA), Zarko STANKOVSKI (CEA), Gumersindo VERDÚ (UPV), Antoni VIDAL-FERRÀNDIZ (UPV), Toshihiro YAMAMOTO (KyotoU), Huaqian YI (CHALMERS), Soobeen YUM (TUM), Igor ZMIJAREVIC (CEA), Andrea ZOIA (CEA)
Number of pages	66
Document type	Deliverable
Work Package	WP02
Document number	D2.5
Issued by	Chalmers
Date of completion	2021-08-30 09:16:16
Dissemination level	Public

---

## Summary

In the CORTEX project, neutron noise solvers are developed, and neutron noise experiments are carried out in the AKR-2 reactor at TUD and in the CROCUS reactor at EPFL. In this report the validation of the solvers based on the experiments is discussed.

---

## Approval

Date	By
2021-08-30 09:18:39	Mr. Mathieu HURSIN (EPFL)
2021-08-30 09:27:22	Pr. Christophe DEMAZIERE (Chalmers)

---

# Table of Contents

<b>1</b>	<b>Introduction .....</b>	<b>7</b>
<b>2</b>	<b>Strategy of the validation work .....</b>	<b>7</b>
2.1	Post-processing of measurements .....	8
2.2	Power Spectrum Density from simulations .....	10
<b>3</b>	<b>Neutron noise solvers.....</b>	<b>10</b>
3.1	CORE SIM+ .....	10
3.2	FEMFUSSION .....	10
3.3	Neutron noise methodology based on PARCS.....	11
3.4	TRIPOLI-4®.....	11
3.5	KU Monte Carlo solver .....	11
3.6	APOLLO-3®.....	11
3.7	NOISE-SN .....	12
<b>4</b>	<b>AKR-2 experiments and simulations .....</b>	<b>12</b>
4.1	Experiments .....	12
4.1.1	Case 1 – Absorber of Variable Strength.....	15
4.1.2	Case 2 – Vibrating Absorber .....	18
4.2	CORE SIM+ modelling .....	20
4.2.1	Modelling of the reactor.....	20
4.2.2	Modelling of the neutron noise sources .....	22
4.2.3	Model verification .....	23
4.3	Modelling for the KU Monte Carlo solver .....	25
4.3.1	Modelling of neutron noise sources in the 1 <sup>st</sup> campaign .....	25
4.3.2	Modelling of neutron noise sources in the 2 <sup>nd</sup> campaign .....	27
4.3.3	Neutron noise simulation scheme.....	28
4.3.4	Detector arrangement and modelling.....	29
4.4	Comparison between simulations and measurements.....	29
4.4.1	Simulations of experiments from the 1 <sup>st</sup> campaign .....	30
4.4.2	Simulations of experiments from the 2 <sup>nd</sup> campaign.....	31
4.4.3	Simulations of experiments from the 3 <sup>rd</sup> campaign .....	31
4.5	Uncertainty analysis for the CORE SIM+ simulations.....	32
4.5.1	Uncertainty analysis for the 1 <sup>st</sup> campaign .....	33
4.5.2	Uncertainty analysis for the 2 <sup>nd</sup> campaign.....	34
<b>5</b>	<b>COLIBRI experiments and simulations .....</b>	<b>36</b>
5.1	COLIBRI experiments .....	36
5.1.1	CROCUS reactor .....	36
5.1.2	COLIBRI device.....	36
5.1.3	First experimental campaign .....	37
5.1.4	Second experimental campaign .....	39
5.2	CORE SIM+ modelling .....	41
5.2.1	Modelling of the reactor and neutron noise source .....	41
5.2.2	Model verification .....	42
5.3	FEMFFUSION and PARCS modelling .....	43
5.4	TRIPOLI-4® modelling.....	44
5.4.1	Model description and simulation parameters .....	44
5.4.2	Criticality calculations: the fundamental flux.....	46
5.4.3	Noise calculations: the first harmonic.....	47
5.4.4	Noise calculations: the second harmonic.....	48
5.5	APOLLO3® – IPK modelling.....	50
5.5.1	Comparison between simulations and measurements for experiments 12 and 13 in COLIBRI campaign 1 .....	50
5.5.2	Effects of the higher frequency on noise amplitude .....	52



5.5.3	Analysis and reconstruction of COLIBRI movement.....	53
<b>5.6</b>	<b>NOISE-SN modelling.....</b>	<b>56</b>
<b>5.7</b>	<b>Comparison between simulations and measurements.....</b>	<b>56</b>
5.7.1	Results for the 1 <sup>st</sup> campaign.....	56
5.7.2	Results for the 2 <sup>nd</sup> campaign.....	58
<b>5.8</b>	<b>Uncertainty analysis for the CORE SIM+ simulations.....</b>	<b>59</b>
5.8.1	Results for the 1 <sup>st</sup> campaign.....	59
5.8.2	Results for the 2 <sup>nd</sup> campaign.....	61
<b>5.9</b>	<b>Sensitivity analysis of the CORE SIM+ model.....</b>	<b>62</b>
5.9.1	Methodology for sensitivity analysis – sensitivity indices.....	62
5.9.2	Methodology for sensitivity analysis – grouping parameters.....	62
5.9.3	Results for the CORE SIM+ simulation of a COLIBRI experiment.....	63
<b>6</b>	<b>Conclusions.....</b>	<b>64</b>
<b>7</b>	<b>References.....</b>	<b>65</b>

## Index of Tables

Table 1:	Selected cases for comparisons between experiments and simulations.....	14
Table 2:	Estimated standard deviation of the CPSD peak area of the first harmonic divided by the mean value for measurement M02 of the third AKR-2 campaign.....	15
Table 3:	Estimated standard deviation of the CPSD peak area of the first harmonic divided by the mean value for measurement M17 of the third AKR-2 campaign.....	15
Table 4:	Uncertainties for selected input and modelling parameters for the simulations related to the 1st experimental campaign in AKR-2.....	33
Table 5:	Uncertainties for selected input parameters in the simulations for the second AKR-2 experimental campaign.....	35
Table 6:	Measurement no. 12 from 1st COLIBRI campaign; spectral power ratio with respect to detector 5.....	38
Table 7:	Measurement no. 12 from 1 <sup>st</sup> COLIBRI campaign; phase angle difference with respect to detector 5.....	38
Table 8:	Measurement no. 13 from 1 <sup>st</sup> COLIBRI campaign; spectral power ratio with respect to detector 5.....	39
Table 9:	Measurement no. 13 from 1st COLIBRI campaign; phase angle difference with respect to detector 5.....	39
Table 10:	Measurement no. 7 from 2nd COLIBRI campaign; spectral power ratio with respect to detector 12.....	40
Table 11:	Measurement no. 7 from 2nd COLIBRI campaign; phase angle difference with respect to detector 12.....	40
Table 12:	Measurement no. 8 from 2nd COLIBRI campaign; spectral power ratio with respect to detector 12.....	41
Table 13:	Measurement no. 8 from 2nd COLIBRI campaign; phase angle difference with respect to detector 12.....	41
Table 14:	Parameters used for TRIPOLI-4® simulations.....	45
Table 15:	Selected input and modelling parameters and their uncertainties for the simulations of the experiments in the 1 <sup>st</sup> COLIBRI campaign.....	60
Table 16:	Parameters for the neutron noise source and their uncertainties for the simulations of the 2 <sup>nd</sup> COLIBRI campaign.....	61



## Table of Figures

Figure 1: Detectors and their positions in the first measurement campaign at AKR-2. ....	13
Figure 2: Detectors and their positions in the second AKR-2 measurement campaign.....	13
Figure 3: Detectors and their positions in the third measurement campaign at AKR-2. ....	14
Figure 4: Relative peak area of the detector signals w.r.t detector 1 in the second measurement campaign for case 1.....	16
Figure 5: Relative peak area of the detector signals w.r.t detector 4 in the third measurement campaign for case 1.....	16
Figure 6: Relative phase of the detector signals w.r.t detector 1 in the second measurement campaign for case 1.....	17
Figure 7: Relative phase of the detector signals w.r.t detector 4 in the third measurement campaign for case 1.....	17
Figure 8: Relative peak area of the detector signals w.r.t detector 1 in the second measurement campaign for case 2.....	18
Figure 9: Relative peak area of the detector signals w.r.t detector 4 in the third measurement campaign for case 2.....	19
Figure 10: Relative phase of the detector signals w.r.t detector 1 in the second measurement campaign for case 2.....	19
Figure 11: Relative phase of the detector signals w.r.t detector 4 in the third measurement campaign for case 2.....	20
Figure 12: CORE SIM+ model of AKR-2. ....	21
Figure 13: Vibrating absorber model in CORE SIM+. ....	21
Figure 14: Rotating absorber model in CORE SIM+. ....	22
Figure 15: Real and imaginary parts of the noise source model for the rotating absorber. ....	22
Figure 16: Real and imaginary parts of the noise source model for the vibrating absorber; 1 <sup>st</sup> campaign on the left and 2 <sup>nd</sup> and 3 <sup>rd</sup> campaign on the right.....	23
Figure 17: Comparison of the static fluxes computed with CORE SIM+ and with Serpent (fast group on the left and thermal group on the right; the fluxes are taken along the red line shown in the reactor drawing at the top). ....	24
Figure 18: Comparison of the static fluxes computed with CORE SIM+ and with Serpent (fast group on the left and thermal group on the right; the fluxes are taken along the red line shown in the reactor drawing at the top). ....	24
Figure 19: AKR-2 point-kinetic zero-power reactor transfer function; comparison between CORE SIM+ and the expected analytical solution. ....	25
Figure 20: Rotating absorber.....	26
Figure 21: $\delta\Sigma_x(r, \omega)$ as a function of $\theta$ .....	26
Figure 22: Movement of the vibrating absorber in the first campaign.....	27
Figure 23: $\delta\Sigma_x(x, \omega)$ as a function of $x$ . ....	27
Figure 24: Schematic view of the vibrating absorber; A = amplitude and W = thickness of the absorber. ....	28
Figure 25: $\text{Re}[\delta\Sigma_x(x, \omega)]$ as a function of $x$ for the case of $k=1$ and a vibration with frequency = 2 Hz and amplitude = 3 cm.....	28
Figure 26: Detector arrangement in the MCNP model for the first campaign.....	29
Figure 27: Detector arrangement in the MCNP model for the 2 <sup>nd</sup> campaign.....	29
Figure 28: Experiment 7 (rotating absorber) in the first campaign at AKR-2; neutron noise amplitude (left) and phase (right).....	30
Figure 29: Experiment 22 (vibrating absorber) in the first campaign at AKR-2; neutron noise amplitude (left) and phase (right). ....	30

Figure 30: Experiment 1 (rotating absorber) in the second campaign at AKR-2; neutron noise amplitude (left) and phase (right). .....	31
Figure 31: Experiment 20 (vibrating absorber) in the second campaign at AKR-2; neutron noise amplitude (left) and phase (right). For detector 3, the experimental power ratio is equal to 5.8. ....	31
Figure 32: Experiment M02 (rotating absorber) in the third campaign at AKR-2; neutron noise amplitude (left) and phase (right). .....	32
Figure 33: Experiment M17 (vibrating absorber) in the third campaign at AKR-2; neutron noise amplitude (left) and phase (right). .....	32
Figure 34: Experiment 7 (rotating absorber) in the 1 <sup>st</sup> campaign at AKR-2; uncertainties of neutron noise amplitude (left) and phase (right) calculated with CORE SIM+. ....	34
Figure 35: Experiment 22 (vibrating absorber), in the 1 <sup>st</sup> campaign at AKR-2; uncertainties of neutron noise amplitude (left) and phase (right) calculated with CORE SIM+. ....	34
Figure 36: Experiment 1 (rotating absorber) in the 2nd campaign at AKR-2; uncertainties of neutron noise amplitude (left) and phase (right) calculated with CORE SIM+. ....	35
Figure 37: Experiment 20 (vibrating absorber) in the 2nd campaign at AKR-2; uncertainties of neutron noise amplitude (left) and phase (right) calculated with CORE SIM+. ....	35
Figure 38: CAD view of the COLIBRI device with the close-up of fuel holding and moving part. ...	36
Figure 39: COLIBRI cable position in time for 1Hz and 1mm amplitude oscillation. ....	37
Figure 40: COLIBRI inductive captor signal at 1 Hz oscillation. ....	37
Figure 41: Detectors and their position in the first CROCUS campaign; the fuel rods oscillating with COLIBRI are in green. ....	38
Figure 42: Detectors and their position in the second CROCUS campaign; the fuel rods oscillating with COLIBRI are in green. ....	40
Figure 43: Radial cross-section of the reactor model (left) and neutron noise sources (right). ....	42
Figure 44: CROCUS zero-power reactor transfer function; comparison between CORE SIM+ and the expected analytical solution. ....	42
Figure 45: Uniform refined mesh for the CROCUS reactor. ....	43
Figure 46: Locally refined mesh around the vibrating cluster of fuel rods, for the CROCUS reactor. ....	43
Figure 47: Radial cut of the reactor specifications (left) and of the corresponding TRIPOLI-4® model (right) for the COLIBRI experimental campaigns in CROCUS. Top: configuration in the first experimental campaign; bottom: configuration in the second experimental campaign. ....	44
Figure 48: The critical neutron flux for the fast (left) and thermal (right) energy group, in arbitrary units. Top: overall spatial distribution. Bottom: zoom over the region of the 18 vibrating fuel rods. ....	46
Figure 49: The first harmonic component of the (normalised) absolute value of the neutron noise field for the fast (left) and thermal (right) energy group. Top: vibration at amplitude 1.5 mm and frequency 0.1 Hz (2nd campaign, experiment 7). Bottom: vibration at amplitude 1.5 mm and frequency 0.97 Hz (2nd campaign, experiment 8). ....	47
Figure 50: The first harmonic component of the phase of the neutron noise field for the fast (left) and thermal (right) energy group. Top: vibration at amplitude 1.5 mm and frequency 0.1 Hz (2nd campaign, experiment 7). Bottom: vibration at amplitude 1.5 mm and frequency 0.97 Hz (2nd campaign, experiment 8). ....	48
Figure 51: Comparison between the second harmonic component of the absolute value of the neutron noise field (cut at the center of the core) for the fast (left) and thermal (right) energy group. Top: vibration at amplitude 1.5 mm and frequency 0.1 Hz (2nd campaign, experiment 7). Bottom: vibration at amplitude 1.5 mm and frequency 0.97 Hz (2nd campaign, experiment 8). ....	49
Figure 52: Comparison between the second harmonic component of the phase of the neutron noise field (cut at the center of the core) for the fast (left) and thermal (right) energy group. Top:	

vibration at amplitude 1.5 mm and frequency 0.1 Hz (2nd campaign, experiment 7). Bottom: vibration at amplitude 1.5 mm and frequency 0.97 Hz (2nd campaign, experiment 8).....	50
Figure 53 : $CPSD_{x,5}$ amplitudes for experiments 12 (a) and 13 (b).....	51
Figure 54: $CPSD_{x,5}$ relative phases for experiments 12 (a) and 13 (b). ....	51
Figure 55: Magnitude of critical CROCUS reactor transfer function, when using classical point-kinetics with parameters from [39]. The frequency range of interest (0.1 Hz – 2.0 Hz) is highlighted in green.....	52
Figure 56: $CPSD_{x,5}$ with various $\omega_c$ and a fixed oscillation amplitude of 1.85 mm. ....	53
Figure 57. Time segments of raw top (blue) and bottom (orange) COLIBRI plates signals for experiment 13 in the first campaign ( $A = 2.0$ mm, $\omega_c = 0.972$ Hz). ....	53
Figure 58. Frequency spectrum of top (blue) and bottom (orange) COLIBRI plates signals for experiment 13 in the first campaign ( $A = 2.0$ mm, $\omega_c = 0.972$ Hz). ....	54
Figure 59. Bottom plate reconstructed (blue solid line) and monochromatic (dashed black line) signals for experiment 13 in COLIBRI campaign 1. Equally spaced discrete points are included (red squares). ....	54
Figure 60. Comparison of measures and computed $CPSD_{x,5}$ amplitudes for experiment 12 (a) and 13 (b). Results obtained from reconstructed and ideal signal [23] are reported as orange bars and black stars, respectively. ....	55
Figure 61. Comparison of measures and computed relative (to pair 6&5) $CPSD_{x,5}$ phases for experiment 12 (a) and 13 (b). Results obtained from reconstructed and ideal signal [23] are reported as orange bars and black stars, respectively. ....	55
Figure 62: Experiment 12 in the 1 <sup>st</sup> COLIBRI campaign; relative noise amplitude (left) and noise phase (right). The detector 5 is used as reference. ....	57
Figure 63: Experiment 12 in the 1 <sup>st</sup> COLIBRI campaign; relative noise amplitude (left) and noise phase (right) predicted by diffusion-based solvers and FEMFFUSION-SP3. The detector 5 is used as reference. ....	57
Figure 64: Experiment 13 in the 1 <sup>st</sup> COLIBRI campaign; relative noise amplitude (left) and noise phase (right). The detector 5 is used as reference. ....	57
Figure 65: Experiment 13 in the 1 <sup>st</sup> COLIBRI campaign; relative noise amplitude (left) and noise phase (right) predicted by diffusion-based solvers and FEMFFUSION-SP3. The detector 5 is used as reference. ....	58
Figure 66: Experiment 7 in the 2 <sup>nd</sup> COLIBRI campaign; relative noise amplitude (left) and noise phase (right) predicted by diffusion-based solvers and FEMFFUSION-SP3. The detector 12 is used as reference. ....	58
Figure 67: Experiment 8 in the 2 <sup>nd</sup> COLIBRI campaign; relative noise amplitude (left) and noise phase (right) predicted by diffusion-based solvers and FEMFFUSION-SP3. The detector 12 is used as reference. ....	59
Figure 68: Experiments 12 (red) and 13 (blue) in the first COLIBRI campaign; neutron noise relative amplitude (left) and phase (right). ....	61
Figure 69: Experiments 7 (red) and 8 (blue) in the 2 <sup>nd</sup> COLIBRI campaign; neutron noise relative amplitude (left) and phase (right). ....	62
Figure 70: Experiment 13 in the 1st COLIBRI campaign; comparison of neutron noise uncertainties obtained from the different groups of input and modelling parameters (left: APSD amplitude, and right: CPSD phase). ....	63
Figure 71: Experiment 13 in the 1st COLIBRI campaign; sensitivity indices and the 95% confidence intervals between the noise source data and the noise APSD amplitude (left) and CPSD phase (right) at the detector locations.....	64

## Abbreviations

APSD	Auto Power Spectrum Density
AVS	Absorber of Variable Strength
CEA	The French Alternative Energies and Atomic Energy Commission
CMFD	Coarse Mesh Finite Difference (method)
COLIBRI	Crocus Oscillator for Lateral Increase Between u metal Rods and Inner zone
CORTEX	CORe monitoring Techniques and EXperimental validation and demonstration
CPSD	Cross Power Spectrum Density
DAQ	Data Acquisition System
EPFL	École Polytechnique Fédérale de Lausanne
FEM	Finite Element Method
GMRES	Generalized Minimal RESidual (method)
GRS	Gesellschaft für Anlagen und Reaktorsicherheit
IPK	Improved Point Kinetics (model)
JFNK	Jacobian Free Newton-Krylov (method)
KU	Kyoto University
MCNP	Monte Carlo N-Particle (code)
PARCS	Purdue Advanced Reactor Core Simulator
PCC	Pearson's Correlation Coefficient
PSD	Power Spectrum Density
TUD	Technische Universität Dresden
UPV	Universitat Politècnica de València
VA	Vibrating Absorber
VCM	Variance-Covariance Matrix

## Summary

In the CORTEX project, neutron noise solvers are developed, and neutron noise experiments are carried out in the AKR-2 reactor at TUD and in the CROCUS reactor at EPFL. In this report the validation of the solvers based on the experiments is discussed.

# 1 Introduction

In the CORTEX project [1], core monitoring and diagnostics techniques have been developed to identify anomalous patterns in a nuclear reactor from the analysis of the neutron noise, so that appropriate actions can be taken at an early stage and prevent potentially dangerous situations from escalating. For this purpose, a crucial task is to model the reactor transfer function that describes the core response to a possible perturbation. Knowing the reactor transfer function allows to retrieve information about the perturbations from the neutron flux measurements via an inversion algorithm, which can be based on advanced signal processing techniques or machine learning, see, e.g., [2-4].

For the modelling of the reactor transfer function, various solvers have been developed in the CORTEX project and are based on different approaches, such as lower- and higher-order deterministic methods and stochastics methods [5-6]. These solvers need to be verified and validated so that they can be reliable when applied to core monitoring and diagnostics. For the validation, neutron noise experiments have been performed in the AKR-2 reactor at TUD and in the CROCUS reactor at EPFL [7-9].

In the AKR-2 reactor, neutron noise experiments are performed using two different types of neutron noise source. The first type is an absorber of variable strength obtained from the rotation of a thermal neutron absorber whose absorption reaction rate varies with respect to the rotation angle. In these experiments, the frequency may be taken between 0.1 and 4 Hz. The second type is a vibrating neutron absorber that moves linearly back and forth inside the reactor core. The maximum amplitude of the vibration may be 15 cm and the maximum frequency 7 Hz.

In the CROCUS reactor, the COLIBRI program investigates the neutron noise induced by the vibration of fuel rods. For the purpose, the reactor is equipped with the COLIBRI device that can oscillate a fuel rod or a group of fuel rods (up to a maximum of 18 fuel rods) in the core periphery. The amplitude of the oscillation may be selected between the values  $\pm 0.5$  and  $\pm 2.0$  mm and the frequency between 0.1 and 2 Hz.

Different neutron noise solvers have been used to simulate the AKR-2 and CROCUS experiments, i.e.:

- The diffusion-based solver CORE SIM+
- The diffusion-based solver FEMFFUSION
- The diffusion-based code PARCS
- The stochastic solver in the Monte Carlo code TRIPOLI-4®
- The Monte Carlo solver developed by Kyoto University – KU
- The APOLLO3® – IPK solver
- The solver NOISE-SN based on a discrete ordinate method

The code FEMFFUSION can perform neutron noise calculations in the time and the frequency domain, although only results obtained from the time-dependent approach are presented in the current report. The codes PARCS and APOLLO3® computes the time-dependent solution of the neutron transport equation. The other solvers make use of the formulation of the neutron noise equation in the frequency domain and thus evaluate the neutron noise as a complex quantity.

From the comparison between calculated and experimental values, the validity of the computational models is explored and assessed.

The report is structured as follows. In section 2, the strategy of the validation work is discussed. In section 3, the solvers used to simulate the experiments are briefly described. In sections 4 and 5, the modelling of the AKR-2 and COLIBRI experiments are respectively presented, and the experimental and calculated neutron noise are compared. In section 6, conclusions are provided.

## 2 Strategy of the validation work

The measurements and the calculation results are post-processed so that they can be compared in terms of Power Spectrum Density – PSD.



## 2.1 Post-processing of measurements

The method presented hereafter was developed at EPFL with the contribution of TUD to obtain Quantities of Interest (QoI) from the measurements performed in the neutron noise experiments. The quantities of interest are the spectral power and the phase angle with respect to a reference detector. The reference detector is usually selected as the one furthest away from the neutron noise source (i.e., the perturbation), being least susceptible to the local effects of the perturbation.

Apart from the oscillations due to the noise source, the neutron flux changes during the reactor transients. These transients are assumed to be longer than the oscillations, whose frequency is usually within 0.1 Hz to 10 Hz. The detector response to the induced oscillations is proportional to the reactor power at that time. It is therefore desirable, to eliminate the power drift and to normalize the detector response independent of the reactor power. A detector signal normalization is performed as:

$$S_N(t) = \frac{S(t) - S_{ave,N}(t)}{S_{ave,N}(t)} \quad (1)$$

where  $S$  is the original detector signal,  $S_N(t)$  the normalized signal, and  $S_{ave,N}(t)$  the detector signal averaged by a moving average. The moving average is calculated by convolution of the detector signal with a box window function of size  $N$  samples with the original signal  $S$  and being extended by interpolating boundary values. The size of the window function  $N$  can be adjusted. In the current work, the window of 10 oscillation lengths proved to give good results. The quantities are defined in the frequency domain and the above-mentioned normalization induces changes in the spectral response. However, these cancel out when performing relative comparisons.

The next step is the Fourier analysis of the normalized signal to obtain the spectral power and the phase shift compared to the reference detector. Both quantities are derived from the calculation of the periodogram, i.e.:

$$Per_{i,j}(v) = FFT(S_{N,j}(t)) \cdot FFT(S_{N,i}(t))^* \quad (2)$$

where  $Per_{i,j}(v)$  is the frequency-dependent periodogram of the normalized signals  $S_{N,i}(t)$  and  $S_{N,j}(t)$  of detectors  $i$  and  $j$ , respectively.

The spectral power density  $PSD$  is calculated by averaging a number  $N$  of absolute values of periodograms as:

$$PSD_{i,j}(v) = \frac{1}{N} \sum_{k=1}^N |Per_{k,i,j}(v)| \quad (3)$$

The phase angle is given by:

$$\varphi_{i,j}(v) = \frac{1}{N} \sum_{k=1}^N \arg(Per_{k,i,j}(v)) \quad (4)$$

In Eqs. (3) and (4),  $k$  denotes the number of evaluations,  $PSD_{i,j}$  the power spectral density and  $\varphi_{i,j}(v)$  the phase angle between normalized detector signals of detectors  $i$  and  $j$ .

Individual periodogram evaluations are usually performed on  $k$  sections of the original signals using the Welch's method. Instead of the Welch's estimate by sectioning the signal, a bootstrapping technique is applied, where the normalized detector signals are sectioned by individual oscillations and a proxy signal generated by random selection from those samples. Apart from retaining the spectral resolution of the original signal, additional advantages include:

- The spectral response of averaging periodograms this way is 1 at the base frequency and higher harmonics, and 0 elsewhere. This removes the unwanted noise at frequencies unrelated to the oscillator.
- By sectioning the original signal according to the oscillator shape one can account for the frequency dispersion of the response, which cannot be achieved by sectioning the data using a static section size.
- Co-variances between individual (and most notably consecutive) oscillation responses get scrambled and an average co-variance estimate remains.

Due to the fact that the response of detectors comes from a common source of noise (the perturbation device), high correlations between responses of individual detectors exist.

The spectral power  $PS$  is defined as the integral of the spectral power density over a frequency range corresponding to the frequency ranges of base or higher harmonic frequencies, i.e.

$$PS_{i,j,m} = \int_{\nu_{m,min}}^{\nu_{m,max}} PSD_{i,j}(\nu) d\nu = \sum_{n=m_{min}}^{m_{max}} PSD_{i,j}(\nu_n) \delta\nu \quad (5)$$

where  $m$  is the number of the harmonic with frequency ranging from  $\nu_{m,min}$  to  $\nu_{m,max}$ , which translates to  $m_{min}$  and  $m_{max}$  when dealing with discrete data.

For the harmonic  $m$ , the relative spectral power  $\widetilde{PS}_{m,i,j,ref}$  and the phase angle difference  $\tilde{\phi}_{m,i,j,ref}$  of detector  $i$  with intermediate detector  $j$  and with respect to the reference detector  $ref$  are respectively obtained from:

$$\widetilde{PS}_{m,i,j,ref} = \frac{PS_{j,i,m}}{PS_{j,ref,m}} \quad (6)$$

$$\tilde{\phi}_{m,i,j,ref} = \phi_{i,j,m} - \phi_{j,ref,m} \quad (7)$$

The use of an intermediate detector  $j$  allows for a statistical estimate of the true  $\widetilde{PS}_{m,i,ref}$  and  $\tilde{\phi}_{m,i,ref}$  with their uncertainties. The final Qol's are then given by a weighted sum of all the intermediate estimates:

$$Qol_{m,i,ref} = \sum_j w_{ij} \widetilde{Qol}_{m,i,j,ref} \quad (8)$$

The weights are derived from the variance  $\sigma_{i,j}^2$  of the distribution of the Qol's as:

$$\tilde{w}_{i,j} = \frac{1}{\sigma_{i,j}^2} \quad (9)$$

$$w_{i,j} = \frac{\tilde{w}_{i,j}}{\sum_j \tilde{w}_{i,j}} \quad (10)$$

Two uncertainty estimates are provided: the propagated uncertainty and the weighted mean uncertainty of the underlying data. For the propagated uncertainty, a covariance matrix is constructed, with defined diagonal terms and with non-diagonal terms that are estimated by a fixed correlation coefficient to satisfy the  $\chi^2$  test. Since large discrepancies between propagated uncertainty estimates and the uncertainty of the mean values usually occur, an additional step based on a pure statistical analysis without any assumptions was developed.

Ranges from  $\nu_{m,min}$  to  $\nu_{m,max}$  need to be determined for the estimation of the quantities of interest. The bootstrapping is repeated for these frequency ranges (the use of the entire spectral range would not be possible because of computational constraints), but, instead of Eqs. (3) and (4), results for each iteration are tallied separately and a probability density function is derived. The statistics of the Qol is treated in the same manner, using Eqs. 6 and 7 on the obtained statistics. Here the maximum likelihood and the desired percentile boundaries (68.27% to conform with  $1\sigma$  from normal distribution) are provided.

In summary, the post-processing developed for the neutron noise measurements is three-fold:

- The relative spectral power  $\widetilde{PS}$  and phase  $\tilde{\phi}$  are estimated from as many estimates as detector's number. This allows statistical estimate for the purpose of uncertainty quantification.
- The preliminary  $PSD$  is computed from the averaging of resampled signals using bootstrapping. This allows maintaining spectral resolution. Uncertainties are given in form of the standard deviations or quantiles of the sampled distributions.
- Frequency ranges are used for a full statistical analysis, obtaining maximum likelihood and percentile boundary values, without assuming distribution shapes.

## 2.2 Power Spectrum Density from simulations

The neutron noise solvers used in this work are based on the time-dependent neutron transport equation or on the frequency-domain neutron transport equation. The modeling of the detectors may be included so that the reaction rates of the detectors are evaluated. If the detectors are not modeled, the calculated thermal neutron noise is analyzed since the detectors are mainly sensitive to thermal neutrons.

In the case of time-dependent simulations, the results are post-processed to extract the neutron noise amplitude and phase according to Eqs. (1) to (4).

In the case of frequency-domain calculations and no modeling of detectors, the relative thermal neutron noise at the fundamental frequency  $\omega_0$  of the noise source and at the locations of the detectors can be used to estimate the Auto Power Spectrum Densities – APSD of the detectors and the Cross Power Spectrum Densities – CPSD between detectors, i.e.

$$PSD_{i,j,\omega_0} = \left( \frac{\delta\phi_{th,\omega_0}}{\phi_{0,th}} \right)_i \left( \frac{\delta\phi_{th,\omega_0}}{\phi_{0,th}} \right)_j^* \quad (11)$$

In the equation above,  $\delta\phi_{th,\omega_0}$  is the absolute thermal neutron noise induced at the fundamental frequency  $\omega_0$ ,  $\phi_{0,th}$  is the static thermal neutron flux,  $i$  and  $j$  identifies the detectors and their locations, and the symbol  $*$  is for the complex conjugate value. If  $i = j$ , the APSD of detector  $i$  is obtained. If  $i \neq j$ , Eq. (11) gives the CPSD between detector  $i$  and detector  $j$ . The same approach can be followed to determine PSD values using the calculated reaction rates of the detectors instead of the relative thermal neutron noise.

## 3 Neutron noise solvers

The solvers used in the validation work based on the neutron noise experiments are briefly introduced, namely CORE SIM+, FEMFFUSION, PARCS, TRIPOLI-4®, the KU Monte Carlo solver, APOLLO3® and NOISE-SN.

### 3.1 CORE SIM+

The core simulator CORE SIM+ [10] developed by Chalmers University of Technology is a flexible diffusion-based solver for neutron noise calculations. It relies on a two-energy group diffusion model and was designed with the purpose of providing fast numerical solutions for a variety of neutron noise problems. A capability that allows the use of non-uniform computational meshes is available so that the discretization of the domain can be optimized with respect to the characteristics of the neutron noise sources. The neutron noise source is modelled as small fluctuations of macroscopic neutron cross sections in a critical nuclear system, and the calculation of the induced neutron noise consists of two steps. In the first step, the static neutron equations are solved via the power iteration method accelerated by Chebyshev polynomials or by a Jacobian Free Newton-Krylov (JFNK) technique. Alternatively, a pure JFNK method can be selected for the solution of the criticality problem. In the second step, the neutron noise equations are solved in the frequency domain, using the static neutron flux and the multiplication factor previously evaluated and assuming no deviation of the perturbed system from criticality. The numerical solution of the linear systems generated from the power iteration algorithm and from the neutron noise equations is obtained from the GMRES method which is accelerated with one from a variety of algebraic preconditioners. Often the numerical solution of complex-valued linear systems raised by noise problems is particularly demanding [11]. For this reason, a multigrid acceleration method was developed for the noise solver of CORE SIM+ [12]. The simulator can also generate neutron noise databases for nuclear power reactors via Green's function method in a fully automated manner.

### 3.2 FEMFFUSION

FEMFFUSION is an open-source general time-domain code that solves the multigroup time-dependent neutron diffusion equation developed by UPV – Universitat Politècnica de València,



available at [13]. This code uses a spatial discretization based on a continuous Galerkin finite element method (FEM) and it can deal with different types of geometries and any problem dimension (1D, 2D and 3D problems). FEMFUSION can solve transients associated to several types of perturbations, as rod ejections accidents and reactivity insertions. Also, it is possible to solve generic changes in the reactor characterized by a custom set of time-dependent cross-sections. Recently, it was updated to simulate neutron noise perturbations in the time domain as generic absorbers of variable strength and vibrating fuel assemblies [14]. Neutron noise problems are local problems and require that the numerical solvers used are set to low tolerances in order to accurately reproduce the small fluctuations of the neutron flux. In addition, the code allows to analyze neutron noise problems in the frequency domain.

### 3.3 Neutron noise methodology based on PARCS

The Purdue Advanced Reactor Core Simulator (PARCS) [15] is a nuclear core simulator that solves the time-dependent two-group neutron diffusion equation in three-dimensional Cartesian geometry using nodal methods and finite difference methods to obtain the transient neutron flux distribution. For the modeling of vibrating fuel assemblies, an external module was developed to permit the user to provide custom time-dependent cross sections. The methodology used for these simulations is described in [5]. Considering problems with no strong variation in the spatial neutron flux distribution, the Coarse Mesh Finite Difference module (CMFD) can be used to perform efficient transient calculations. The temporal discretization is performed using the theta method with an exponential transformation of the group. The time-dependent neutron flux is post processed using a numerical Fourier Transform so that amplitude and phase of the neutron noise can be obtained at the frequencies of interest.

### 3.4 TRIPOLI-4®

A stochastic noise solver in the frequency domain has been implemented in the development version of the Monte Carlo TRIPOLI-4® at CEA [16-17]. The noise equations are solved by transporting particles carrying two statistical weights, one for the real part and one for the imaginary part of the noise field. Particle flights are sampled from an exponential distribution, as for the regular Boltzmann equation, whereas the collision events are modified by the presence of complex operators in the noise equations (an additional imaginary absorption cross section and a complex delayed neutron yield). Such terms are dealt with by correspondingly modifying the particle weights. If required, the noise source term is preliminarily computed by running a power iteration and sampling from the frequency-dependent distributions.

### 3.5 KU Monte Carlo solver

The algorithm that is adopted in the Monte Carlo solver developed by Kyoto University is fundamentally the same as that in TRIPOLI-4®. The main difference from TRIPOLI-4® is that a special term in the frequency-domain neutron noise transport equation,  $i\omega\phi/v$ , is dealt with by changing a complex-valued particle weight continuously during each flight distance. However, this treatment for the special term is mathematically equivalent to the method in TRIPOLI-4®. Special functions for frequency domain calculation using complex-valued weights are installed into MCNP version 4. The details of the Monte Carlo algorithm are presented in [18-19].

### 3.6 APOLLO-3®

The APOLLO3® IPK model used for the simulation of neutron noise is developed starting from the flux and precursors concentration equations:

$$\left( \frac{1}{v} \partial_t + \hat{\Omega} \cdot \nabla + \hat{\Sigma}_t(\vec{r}, E, t) \right) \psi = H\psi + \frac{F_p}{k_{dyn}} \phi + \frac{F_d \vec{C}}{k_{dyn}} \quad (12)$$

$$\partial_t C_i(\vec{r}, t) = -\bar{\lambda}_i C_i(\vec{r}, t) + \beta_i \int_E dE' v \Sigma_f(\vec{r}, E', t) \phi(\vec{r}, E', t) \quad (13)$$

where  $\vec{r}$  is the spatial coordinate,  $E$  is the energy group,  $\Omega$  is the direction angle,  $t$  the time,  $\tilde{\Sigma}_t(\vec{r}, E, t)$  is the total cross section accounting for the  $DB^2$  coefficient,  $\psi = \psi(\vec{r}, E, \Omega, t)$  is the angular flux,  $\phi = \phi(\vec{r}, E, t)$  is the scalar flux,  $k_{dyn}$  is the dynamic eigenvalue [20],  $\Sigma_f$  is the macroscopic fission cross section,  $\nu$  is the average number of neutrons produced by fission,  $\beta_i$  is the fraction of delayed neutron for family  $i$ . The prompt and delayed fission sources are identified by  $F_p$  and  $F_d \vec{C} = \sum_{i=1}^{N_d} \chi_{d,i} \lambda_i C_i$ , where  $C_i$  contains the convolution integral for the  $i$ -th precursor concentration whose decay constant is  $\lambda_i$ . Differently from the traditional point-kinetics approach [21-22], the angular flux is factorized with the shape  $S(\vec{r}, E, \Omega, t)$  and power  $P(E, t)$  functions that preserve their energy dependence. By adopting a suitable normalization condition for all energy groups  $N_G$  and after some manipulations, the final form of the point-kinetics equation is:

$$\partial_t P + \frac{1}{\nu} \langle \partial_t S \rangle P + \frac{J^+ - J^-}{\langle S/\nu \rangle} P + \langle \tilde{\Sigma}_t S \rangle P - \langle HS \rangle P = \frac{1}{k_{dyn}} \langle F_p S \rangle P + \frac{1}{k_{dyn}} \langle F_d \vec{C} \rangle \quad (14)$$

where  $\langle \dots \rangle$  indicates the scalar product for space and angle. More details on the IPK model formulation and the leakage model used to estimate the  $DB^2$  coefficient can be found in [23] and [24], respectively.

### 3.7 NOISE-SN

The neutron noise solver NOISE-SN developed by Chalmers University of Technology is based on the finite diamond difference method for the spatial discretization, the discrete ordinates method for the angular discretization, and the multi-energy group formalism [6, 25]. The Chebyshev-Legendre quadrature is used to construct the scalar neutron flux from the angular neutron flux. The iterative scheme is accelerated using a Coarse Mesh Finite Difference – CMFD technique. Considering a critical nuclear system with a perturbation described as small fluctuations of the macroscopic neutron cross sections, the solver first calculates the neutron flux and the multiplication factor associated with the static problem. Then the neutron noise equations are solved in the frequency domain, so that the amplitude and the phase of the neutron noise are determined according to the prescribed neutron noise source and the estimated static solution.

## 4 AKR-2 experiments and simulations

The diffusion-based neutron noise solver CORE SIM+ and the stochastic neutron noise solver developed by Kyoto University in the code MCNP have been used to simulate neutron noise experiments from 3 campaigns carried out in the research reactor AKR-2 (TUD).

### 4.1 Experiments

Three measurement campaigns to produce high quality experimental neutron noise data were conducted at AKR-2. A detailed list of experiments and the experimental setup of the measurements is described in detail in [7-9]. Throughout these campaigns, the measurements were improved in numerous ways including: the use of a high precision perturbation linear motor axis; the application of new scintillator technology based on optical fibres, which was developed by EPFL (see [26] for more details); and the development of a robust and consistent postprocessing to allow for the estimation of experimental uncertainties in the quantities of interest (see section 2.1).

In the first experimental campaign at AKR-2, the data acquisition systems (DAQs) available at TUD and EPFL were compared with the industry grade ISTec Sigma system. It was found that the TUD and EPFL data acquisition systems can safely be used for the acquisition times in question [7]. The DAQ used in the first AKR-2 measurement campaign relied on a mix of permanently installed as well as mobile detectors. An overview of the detector arrangement can be seen in Figure 1.

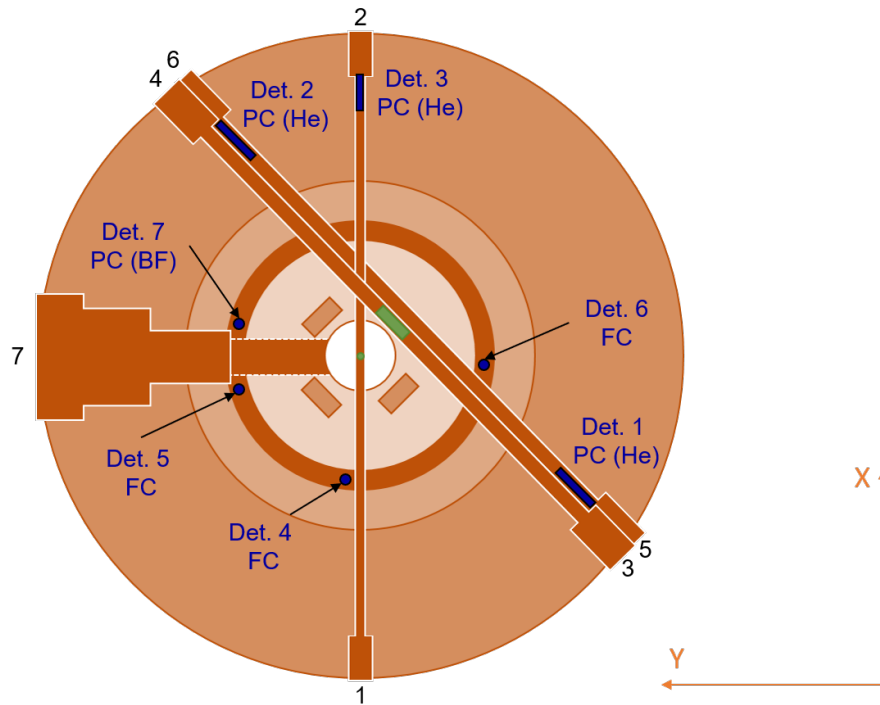


**Figure 1: Detectors and their positions in the first measurement campaign at AKR-2.**

The arrangement of the detectors for the second and third campaigns is shown in Figures 2 and 3, respectively. Different types of detectors were used, and the strategy was to provide signals without electronic filtering and to perform measurements closer to the core region. For this reason, a set of three miniature scintillators developed and operated by EPFL were used in the second campaign [26]. These detectors were not available in the third measurement campaign because of the travel restrictions in the COVID-19 pandemic. As an alternative, one fission chamber was placed in the center of channel 3-4. Synchronization between the different DAQs presented a challenge in the second measurement campaign and was addressed by using a single DAQ in the third campaign.

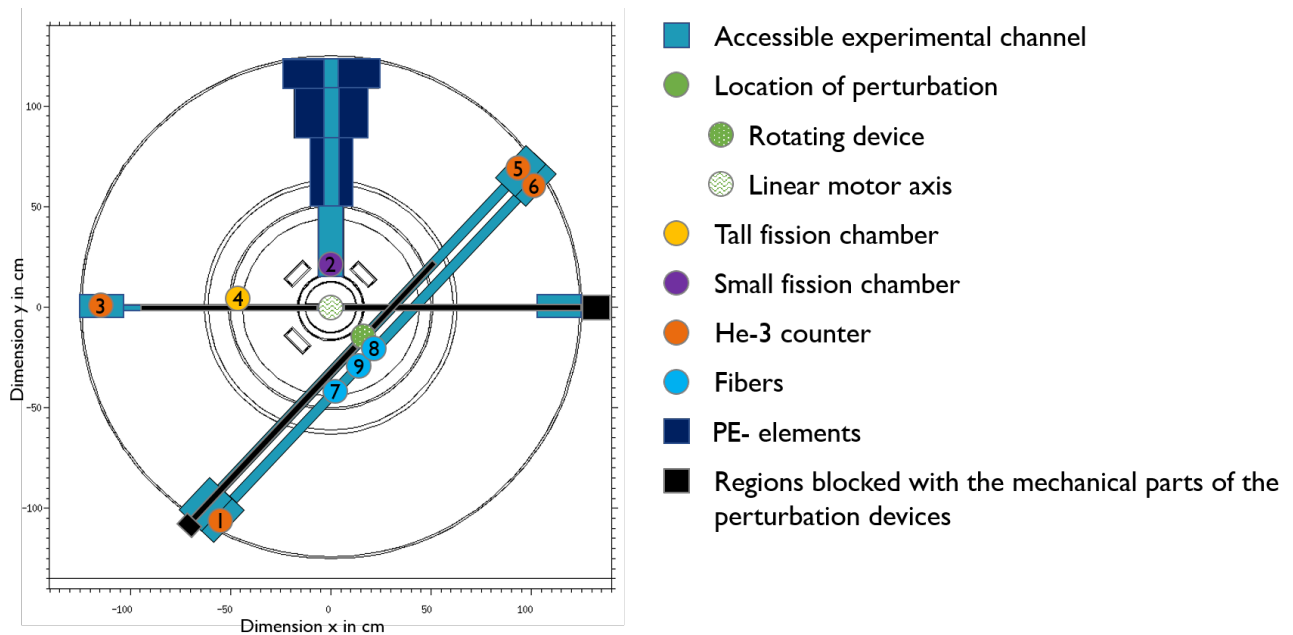


**Figure 2: Detectors and their positions in the second AKR-2 measurement campaign.**

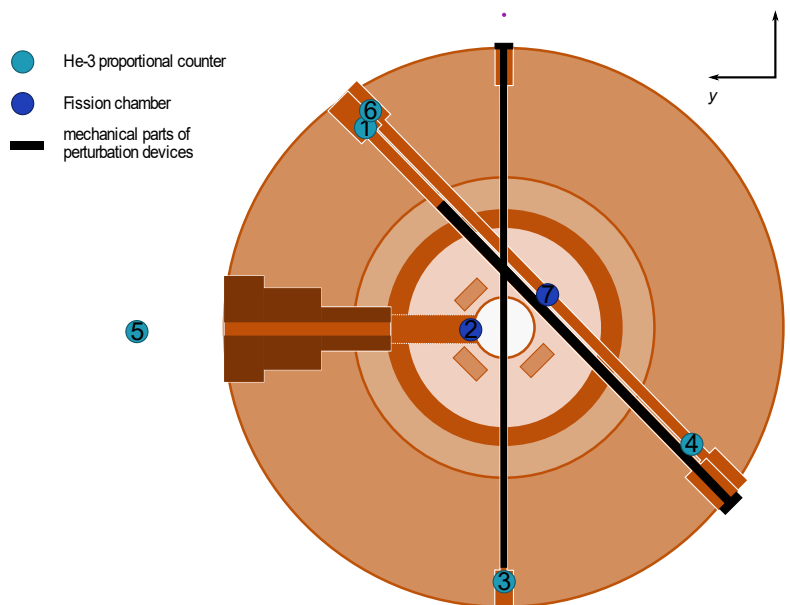


**Figure 3: Detectors and their positions in the third measurement campaign at AKR-2.**

The current discussion is mainly focused on 2 cases that were selected for the comparison with the simulations. The first case is the Absorber of Variable Strength (AVS) driven at a rotation frequency of 2 Hz. The second case is an off-center perturbation with the Vibrating Absorber (VA) with an amplitude of  $\pm 3$  cm and an oscillation frequency of 2 Hz. Both cases were repeated in multiple experiments and a list of the relevant measurements is given in Table 1.

**Table 1: Selected cases for comparisons between experiments and simulations**

Case	Perturbation device	Frequency	Location of oscillation w.r.t. core center	Amplitude	Designation of experiments
Case 1	AVS – Absorber of Variable Strength	2 Hz	N/A	N/A	2 <sup>nd</sup> campaign: M08, M14, M21 3 <sup>rd</sup> campaign: M02, M12, M34
Case 2	VA – Vibrating Absorber	2 Hz	5.5 cm	3 cm	2 <sup>nd</sup> campaign: M20 3 <sup>rd</sup> campaign: M17, M29, M46

In order to evaluate the relative neutron noise, the peak area of the absolute value of the normalized detector signals were evaluated together with their uncertainty estimate. The uncertainty estimates via the post-processing of the experiments of the second campaign in case 1 have a range of approximately 5% and 25% depending on the noise level of the detectors and the experiment. These uncertainties were reduced in the third campaign to a range of approximately 3% to 18%. Two examples of the estimated uncertainties are summarized in Table 2 for measurement M02 of the third campaign (case 1, absorber of variable strength) and in Table 3 for measurement M17 of the third campaign (case2, vibrating absorber). For case 2, the uncertainties are generally lower due to a higher signal-to-noise ratio than for case 1. The detectors with lower count rates, like for example the fission chambers, show higher uncertainty due to the lower signal-to-noise ratio of these detectors.

**Table 2: Estimated standard deviation of the CPSD peak area of the first harmonic divided by the mean value for measurement M02 of the third AKR-2 campaign**

	det 01	det 02	det 03	det 04	det 05	det 06	det 07
det 01	0.04333	0.098153	0.090253	0.034872	0.035854	0.035037	0.083338
det 02	0.098153	0.183104	0.129845	0.099505	0.100988	0.100172	0.125762
det 03	0.090253	0.129845	0.166885	0.090679	0.091632	0.091027	0.11811
det 04	0.034872	0.099505	0.090679	0.050145	0.037519	0.037094	0.084181
det 05	0.035854	0.100988	0.091632	0.037519	0.052453	0.037989	0.084839
det 06	0.035037	0.100172	0.091027	0.037094	0.037989	0.050023	0.084683
det 07	0.083338	0.125762	0.11811	0.084181	0.084839	0.084683	0.154546

**Table 3: Estimated standard deviation of the CPSD peak area of the first harmonic divided by the mean value for measurement M17 of the third AKR-2 campaign**

	det 01	det 02	det 03	det 04	det 05	det 06	det 07
det 01	0.027726	0.054641	0.016812	0.019854	0.019579	0.019503	0.067671
det 02	0.054641	0.103831	0.053561	0.054325	0.05422	0.054357	0.084099
det 03	0.016812	0.053561	0.017518	0.016542	0.015866	0.016187	0.066826
det 04	0.019854	0.054325	0.016542	0.027431	0.019384	0.019376	0.06769
det 05	0.019579	0.05422	0.015866	0.019384	0.02585	0.018924	0.067328
det 06	0.019503	0.054357	0.016187	0.019376	0.018924	0.026578	0.067539
det 07	0.067671	0.084099	0.066826	0.06769	0.067328	0.067539	0.128842

All CPSD peak area values and phases are used in order to estimate the quantities of interest,  $FFT_i/FFT_{ref} = CPSD_{ji}/CPSD_{j,ref}$  and  $\arg(FFT_i) - \arg(FFT_{ref})$ , where  $i$  and  $j$  denote generic detectors and  $ref$  designates a reference detector, which is detector 1 for the 2nd campaign and detector 4 for the 3rd campaign. These quantities can be compared to the simulations, as discussed in section 2.1. For the estimation of the mean values and the uncertainties, all histograms of all CPSDs are taken into account. Uncertainties are estimated with the 5% and 95% percentile of the distribution for all AKR-2 data.

#### 4.1.1 Case 1 – Absorber of Variable Strength

Results for the relative peak area for case 1 (AVS) are shown in Figures 4 (second campaign) and 5 (third campaign). The results and estimated uncertainties are consistent within the repeated experiments. The uncertainties are generally higher for lower signal-to-noise ratios which means that the fission chambers have higher uncertainties, and the uncertainty is lower in the He-3 proportional counters for the third campaign than for the second campaign.

Phase values are presented in Figures 6 (second campaign) and 7 (third campaign). Despite being consistent within different measurements, measurements in the second campaign show a high phase difference between detectors of the two different DAQs (detectors 1, 2, 3, 5, 6 vs. detectors 7, 8, 9). This may be a hint to a synchronization issue during these measurements. If this is the case for these experiments cannot be said for certain at this point. For this reason, all neutron noise signal were captured with only one DAQ in the third campaign. Uncertainty estimates of the phase are low and repetitions are consistent for the third campaign measurements.

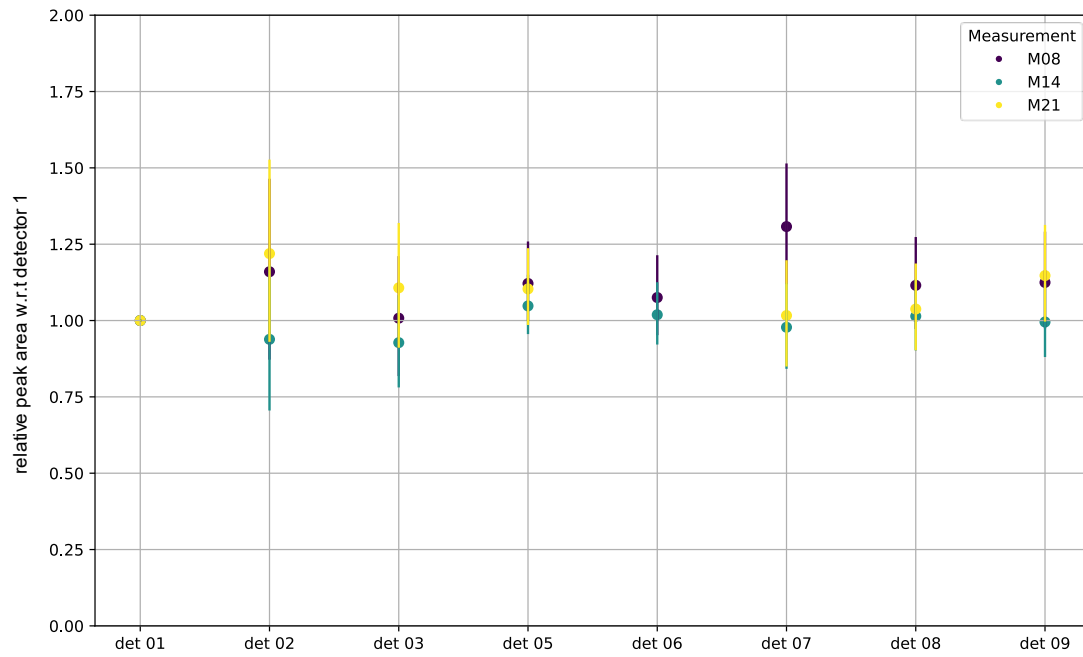


**Figure 4: Relative peak area of the detector signals w.r.t detector 1 in the second measurement campaign for case 1.**

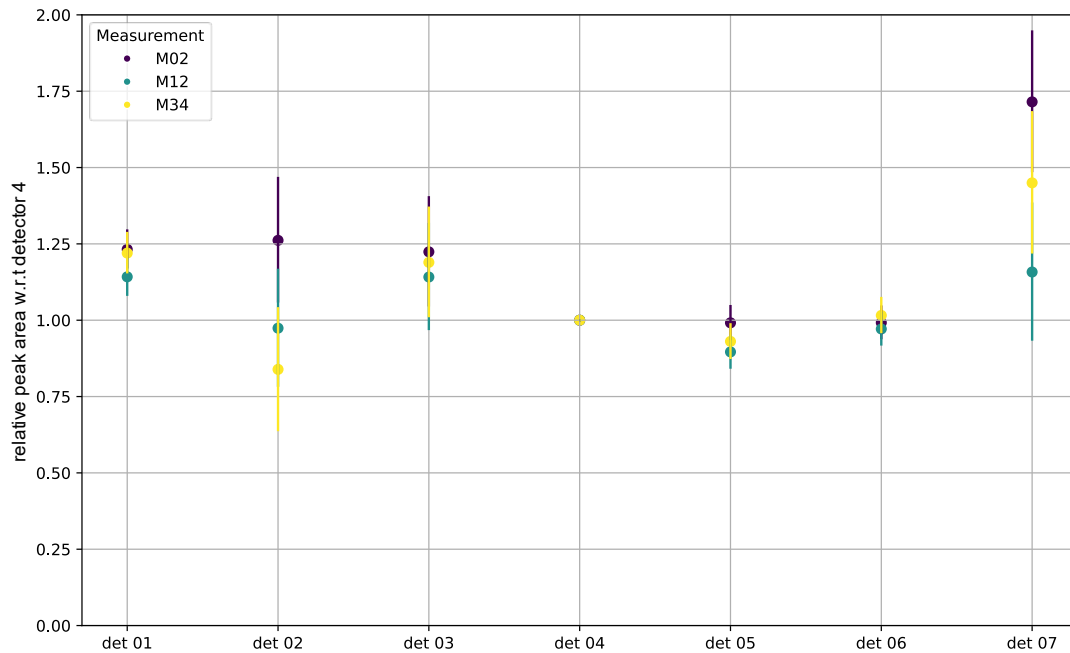


**Figure 5: Relative peak area of the detector signals w.r.t detector 4 in the third measurement campaign for case 1.**

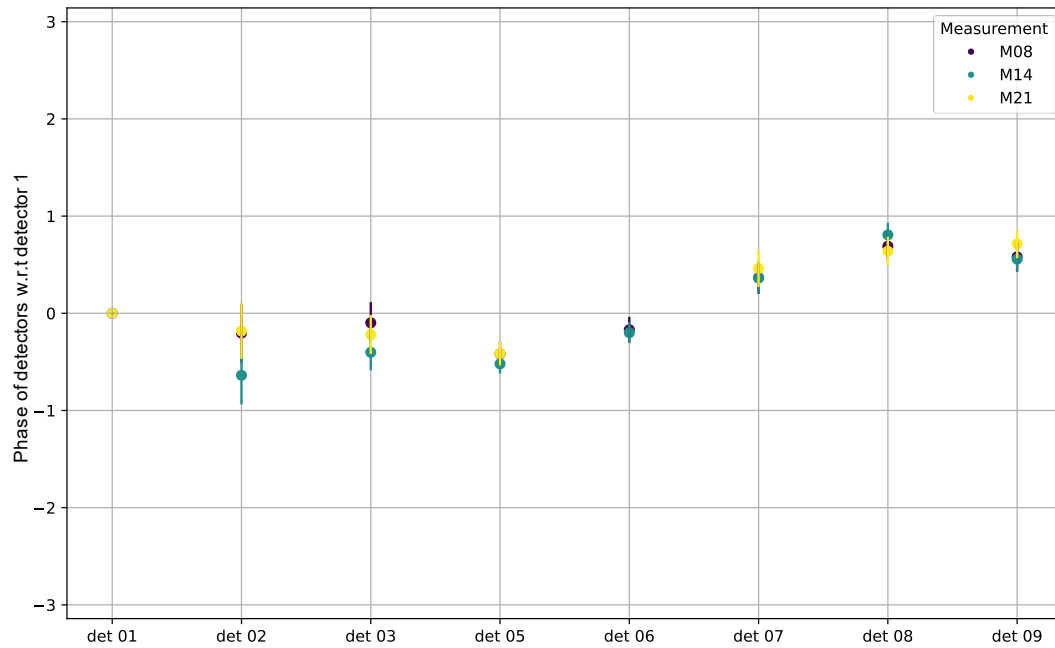


**Figure 6: Relative phase of the detector signals w.r.t detector 1 in the second measurement campaign for case 1.**

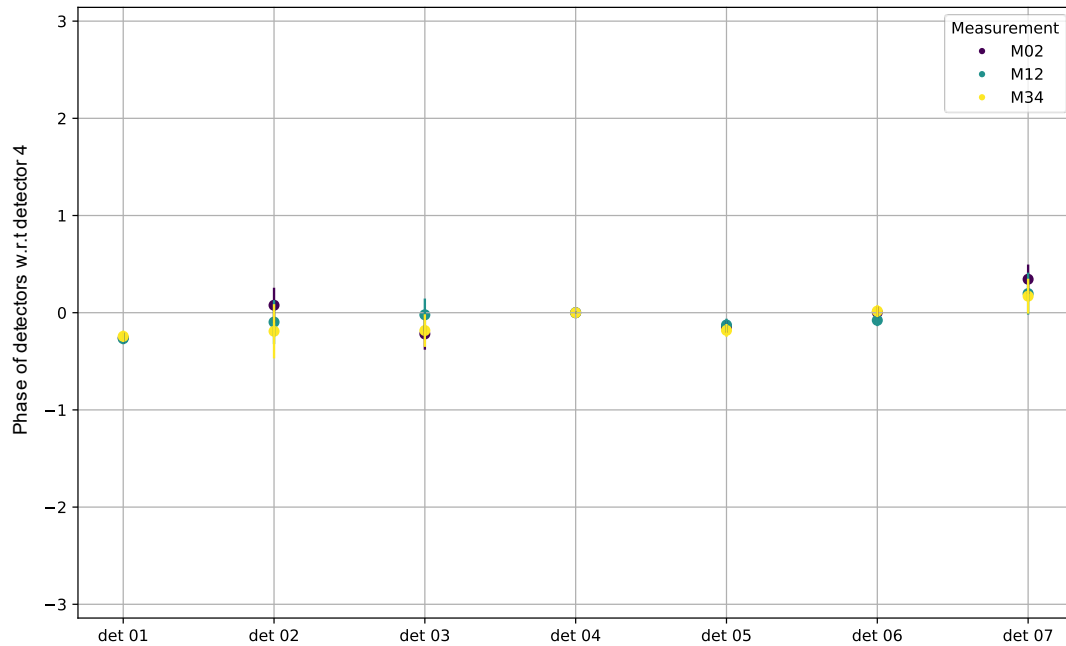


**Figure 7: Relative phase of the detector signals w.r.t detector 4 in the third measurement campaign for case 1.**

#### 4.1.2 Case 2 – Vibrating Absorber

Results for the relative peak area for case 2 (VA) can be found in Figure 8 (second campaign) and Figure 9 (third campaign). Results are near one except for detector 3 which is facing directly at the noise source. All data shows low uncertainty estimates due to the higher signal-to-noise ratio with the vibrating absorber being driven with a large amplitude.

Phase values are presented in Figure 10 (second campaign) and Figure 11 (third campaign). There is again a phase shift between the different DAQs in the second campaign. Looking at the results for the third campaign, this deviation is almost certainly due to a synchronization issue of the different DAQs.

Overall repeated measurements of AKR-2 show consistent uncertainty estimates and overall good results. Phase data of the second campaign should be handled with care and where possible third campaign data should be preferred.

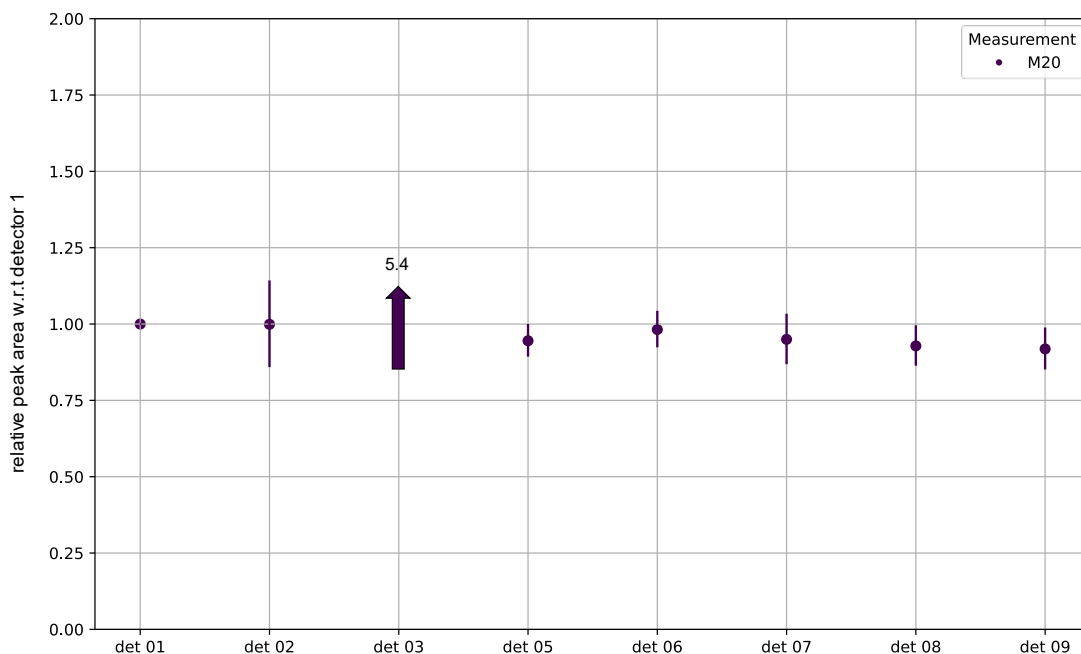


**Figure 8: Relative peak area of the detector signals w.r.t detector 1 in the second measurement campaign for case 2.**



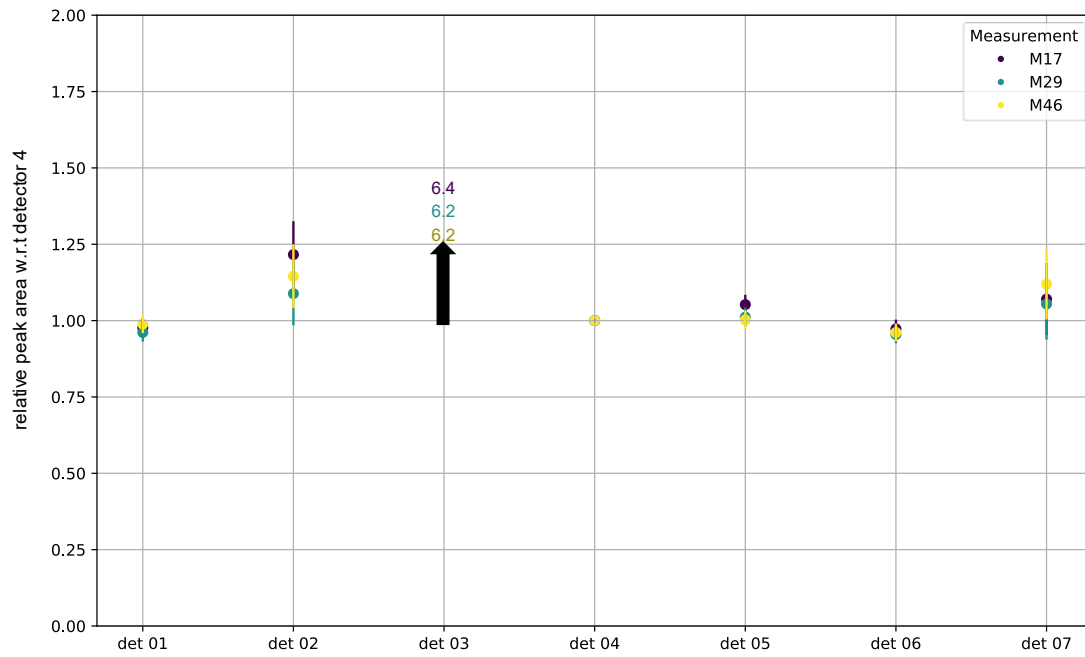


**Figure 9: Relative peak area of the detector signals w.r.t detector 4 in the third measurement campaign for case 2.**

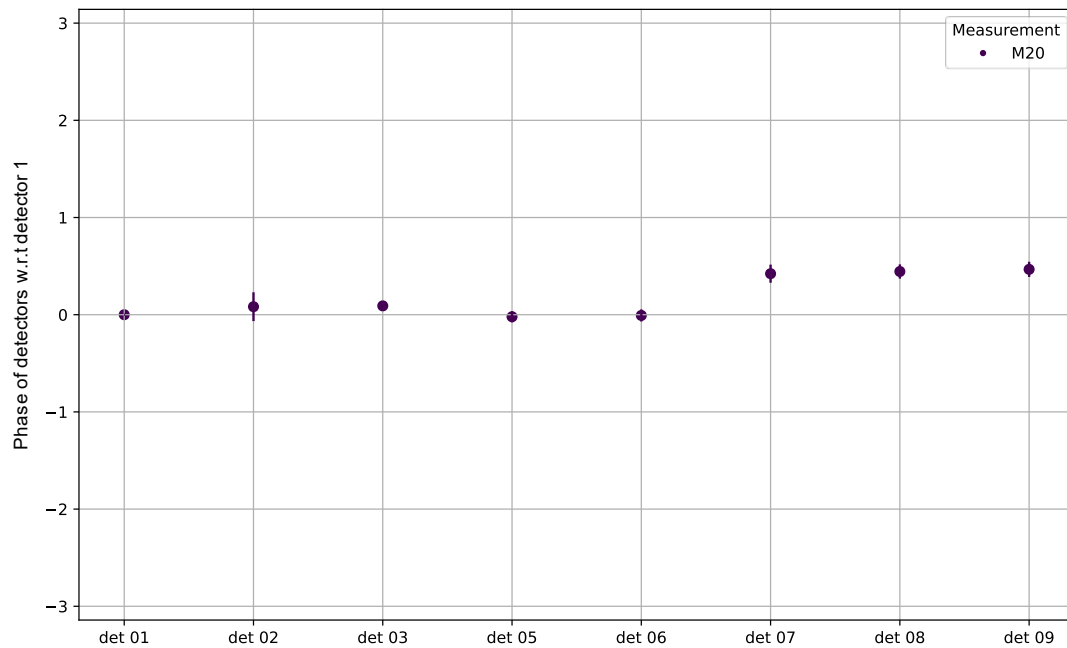


**Figure 10: Relative phase of the detector signals w.r.t detector 1 in the second measurement campaign for case 2.**

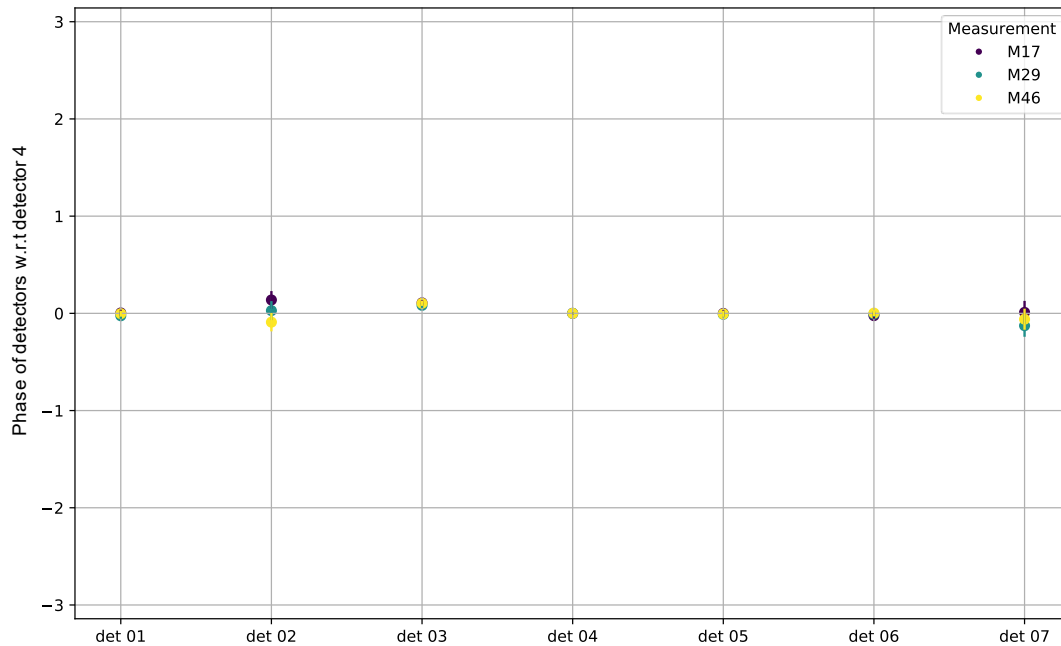


**Figure 11: Relative phase of the detector signals w.r.t detector 4 in the third measurement campaign for case 2.**

## 4.2 CORE SIM+ modelling

Models of the AKR-2 reactor and of the neutron noise sources have been developed for the CORE SIM+ simulations of experiments from the three AKR-2 neutron noise campaigns. Two verification tests were performed. First, the neutron flux calculated for the static reactor configuration was compared with a reference solution obtained from Monte Carlo calculations. Second, the model was used to estimate the point-kinetics zero-power reactor transfer function for AKR-2 and the result was compared with an analytical solution.

### 4.2.1 Modelling of the reactor

The reactor is modelled as a union of homogeneous regions as illustrated in Figure 12. The energy-group nuclear constants for each region are generated with the Monte-Carlo code Serpent [27].

Two kinds of experiments are simulated, namely the vibrating absorber and the rotating absorber experiments. In the vibrating absorber experiments, a thin thermal absorber foil, introduced through the central channel, vibrates inside the reactor core. In the rotating absorber experiments, a thin absorber foil rotates inside a peripheral horizontal channel that does not cross the core. Reactor models for the simulations of the experiments from the first campaign were developed. These models were improved for the simulations in the second and third campaigns, since locally finer spatial meshes were used for a more accurate description of the noise sources. The spatial discretization of the AKR-2 reactor with emphasis on the region in which the noise source is located is illustrated in Figure 13 for the case of the vibrating absorber and in Figure 14 for the case of the rotating absorber.

No detectors are modelled in CORE SIM+. Instead, the thermal neutron noise calculated at the nodes of the grid corresponding to the center of the active region of each detector is used. The detector arrangements in each experimental campaign are illustrated in Figure 1 to 3.

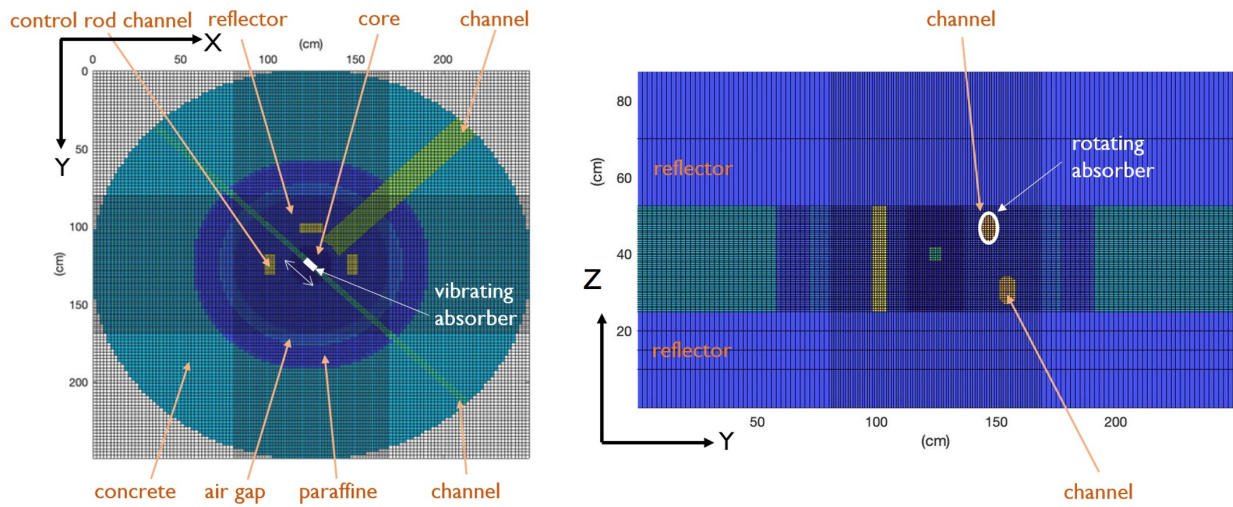


**Figure 12: CORE SIM+ model of AKR-2.**

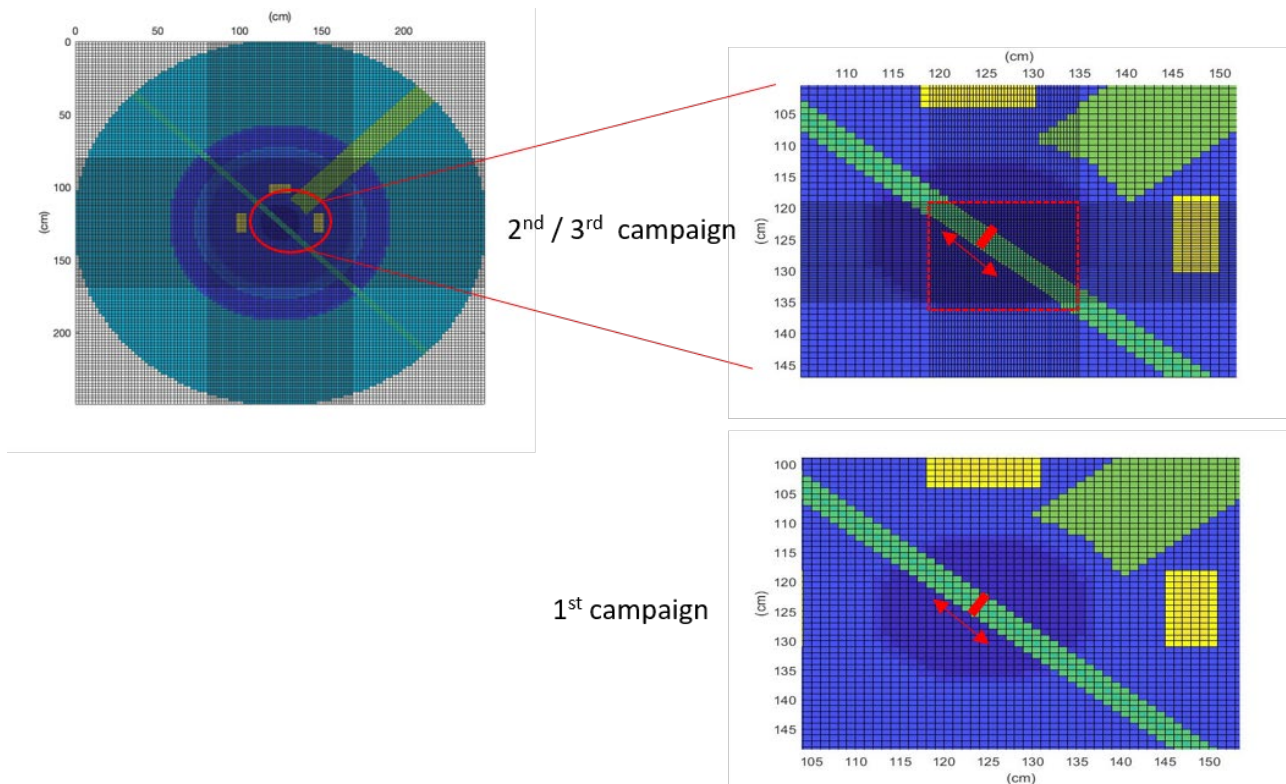


**Figure 13: Vibrating absorber model in CORE SIM+.**

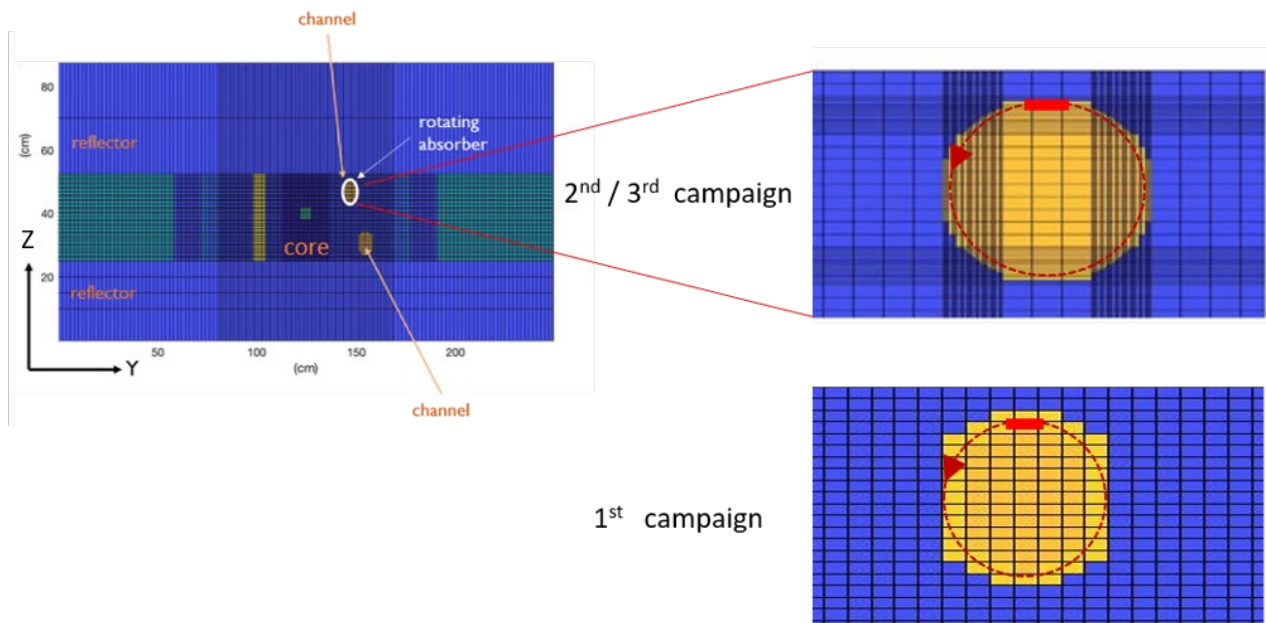


**Figure 14: Rotating absorber model in CORE SIM+.**

#### 4.2.2 Modelling of the neutron noise sources

The two neutron noise sources, i.e., the rotating absorber and the vibrating absorber, are modelled with a time-dependent expression of the fluctuation of thermal absorption macroscopic cross section caused by the moving thermal absorber. A frequency-dependent model is then built via a Fourier transform of the time-dependent model. The first harmonic of the frequency-dependent source model is used as input for the CORE SIM+ simulation. Figures 15 and 16 show the real and the imaginary parts of the models for the rotating and vibrating absorbers, respectively. The model for the vibrating absorber depends on the campaign. The model for the 1<sup>st</sup> campaign describes an absorber that moves with a trapezoidal profile (see Figure 16, left-hand plot), while the model for the 2<sup>nd</sup> and 3<sup>rd</sup> campaigns is based on a sinusoidal vibration of the absorber (see Figure 16, right-hand plot).

The neutron noise source models used for CORE SIM+ are similar to the models developed for the Monte Carlo simulations (see sections 4.3.1 and 4.3.2).

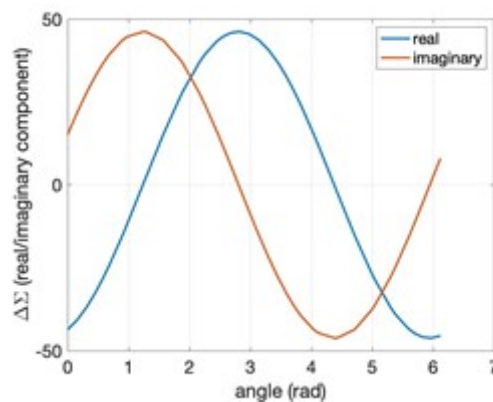


**Figure 15: Real and imaginary parts of the noise source model for the rotating absorber.**

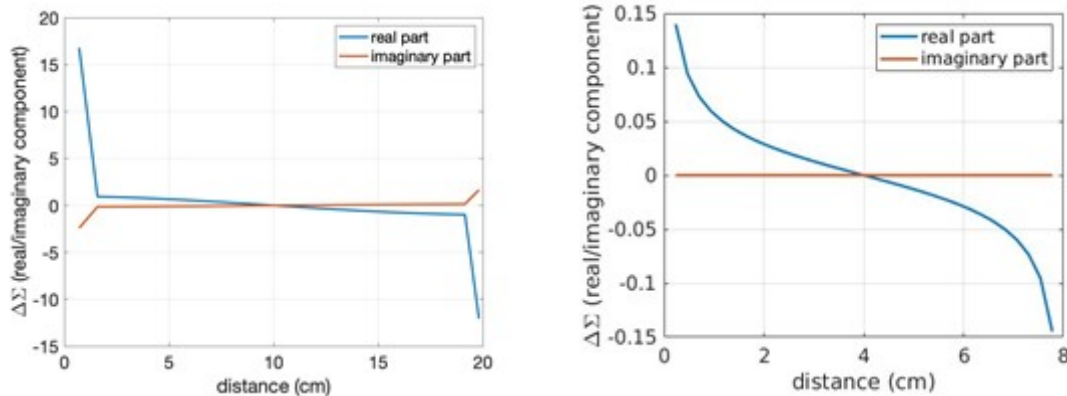


**Figure 16: Real and imaginary parts of the noise source model for the vibrating absorber; 1<sup>st</sup> campaign on the left and 2<sup>nd</sup> and 3<sup>rd</sup> campaign on the right.**

#### 4.2.3 Model verification

The reactor AKR-2 consists of a small core, a few layers of surrounding materials, and multiple horizontal and vertical channels for instrumentation and experiments. This complexity is translated into a large variation of the nuclear properties throughout the reactor. Since the adequacy of diffusion theory for the modelling of such systems is questionable, CORE SIM+ and the developed model needs to be carefully evaluated.

As a first step, the static solution computed with CORE SIM+ is compared with the reference calculated with the Monte Carlo code Serpent. Figures 17 and 18 show the comparison of the static fluxes, respectively, along a line that crosses horizontally the reactor and along a diagonal, at the same axial elevation of the central channel and of the large diagonal channel (see the red line in the reactor drawings that are included in the figures). Although the reactor configuration is complex, CORE SIM+ can reproduce the main features of the reference solution rather satisfactorily. Discrepancies are found mainly in the air-filled central channel crossing the core and in regions surrounding the core such as the air-filled control rod channels (see Figure 17). In addition, the static flux calculated with CORE SIM+ deviates significantly from the reference static flux in the large diagonal channel (see Figure 18). This behaviour is expected and is due to the limitations of diffusion theory when applied to strongly heterogeneous systems and optically thin mediums of large size.

In the second step, the point-kinetic zero-power transfer function of AKR-2 is estimated with CORE SIM+ and compared with an analytical form. For this purpose, CORE SIM+ is used to calculate the reactor response to the vibrating absorber at various frequencies. Then, the point-kinetic component of the response is extracted according to the methodology described in [28] and compared with the analytical form, see Figure 19. CORE SIM+ estimates the transfer function very satisfactorily in the frequency range between  $10^{-4}$  Hz and 100 Hz, which encloses the frequency range of the noise experiments, i.e. (0.01 Hz – 7 Hz). Despite the complexity of the reactor, the code can reproduce the broad variation of the amplitude and phase over the frequency range. The maximum deviation is ~6% for the amplitude and below 11 degrees for the phase.



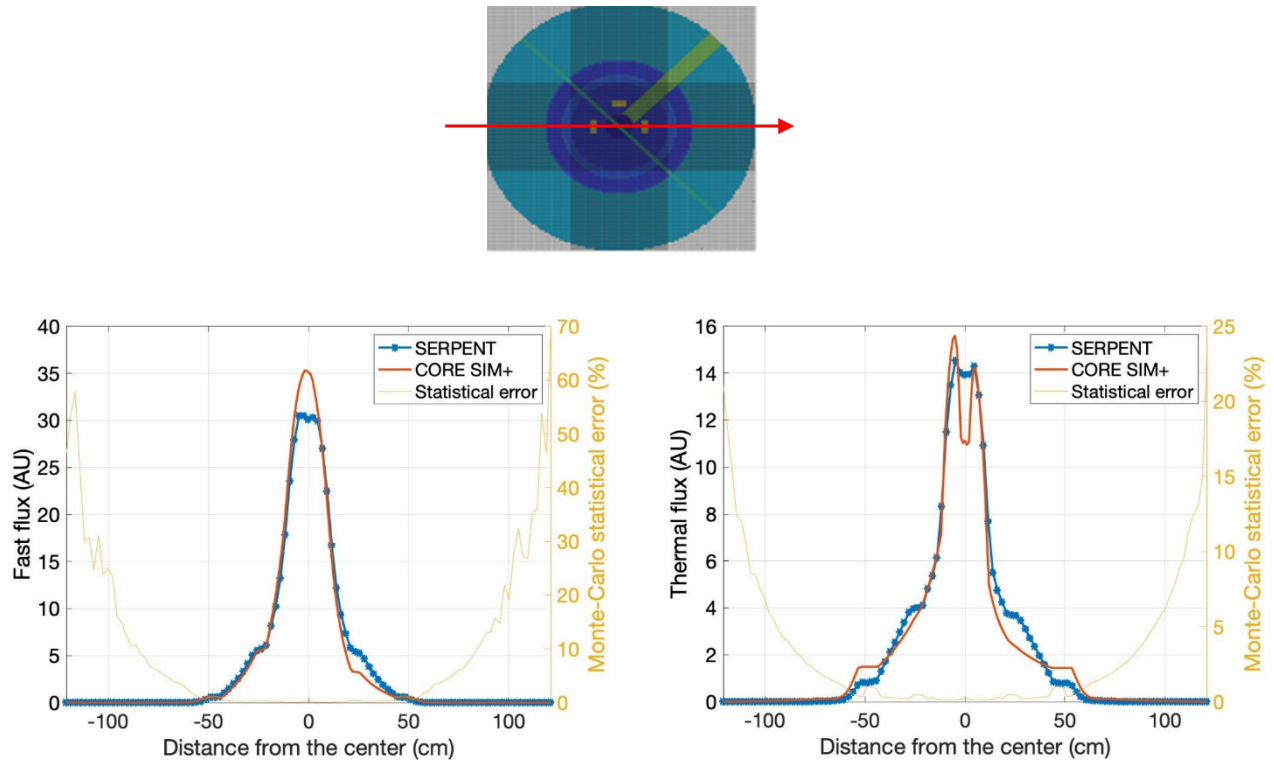


**Figure 17: Comparison of the static fluxes computed with CORE SIM+ and with Serpent (fast group on the left and thermal group on the right; the fluxes are taken along the red line shown in the reactor drawing at the top).**

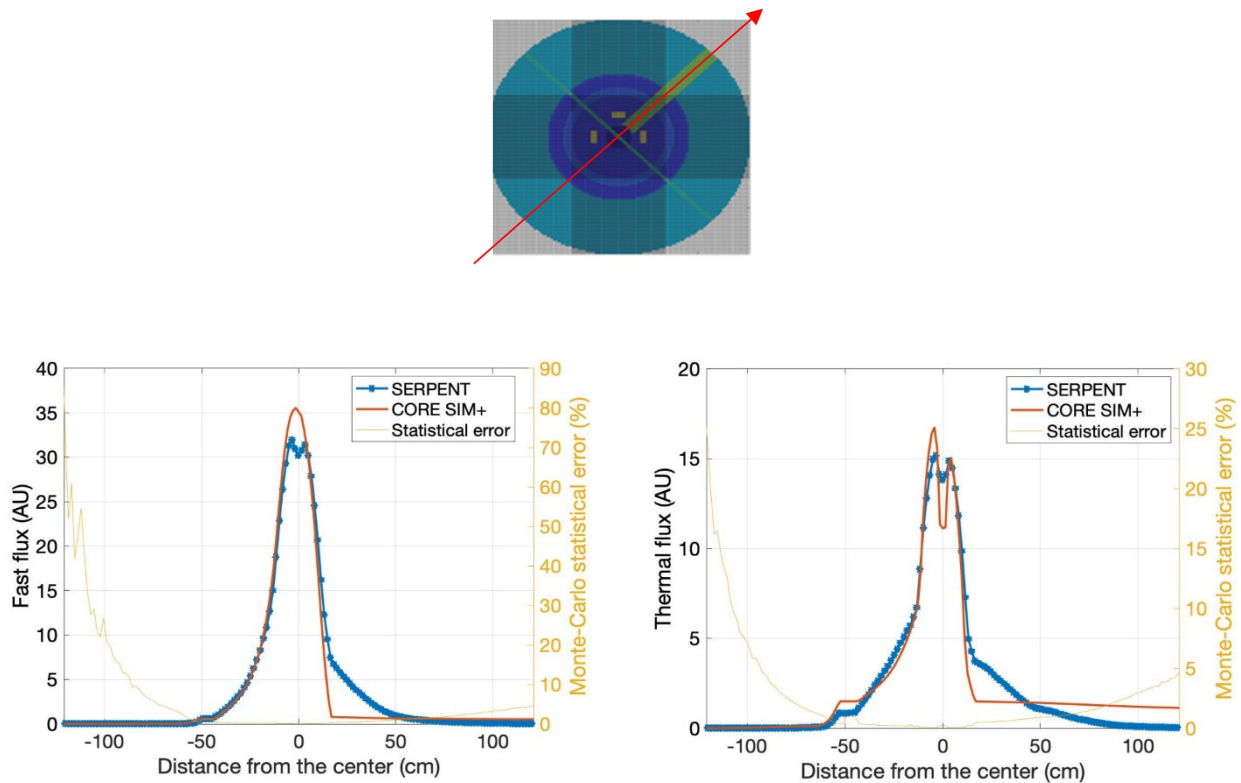


**Figure 18: Comparison of the static fluxes computed with CORE SIM+ and with Serpent (fast group on the left and thermal group on the right; the fluxes are taken along the red line shown in the reactor drawing at the top).**

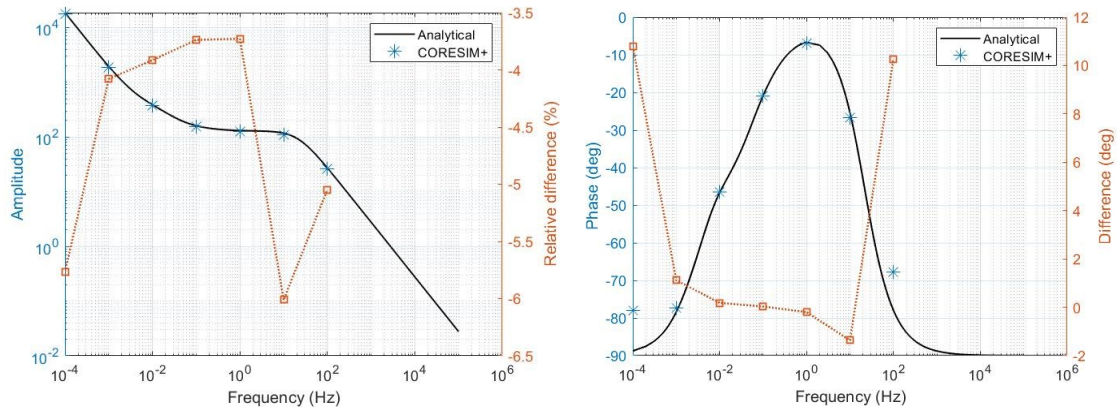


**Figure 19: AKR-2 point-kinetic zero-power reactor transfer function; comparison between CORE SIM+ and the expected analytical solution.**

### 4.3 Modelling for the KU Monte Carlo solver

Models of the AKR-2 reactor and of the neutron noise sources have been developed by Kyoto University for Monte Carlo simulations of experiments from the first and second AKR-2 neutron noise campaigns.

#### 4.3.1 Modelling of neutron noise sources in the 1<sup>st</sup> campaign

The neutron noise source is defined by the following equation:

$$S(\mathbf{r}, \boldsymbol{\Omega}, E, \omega) = -\delta\Sigma_t(\mathbf{r}, E, \omega)\phi_0(\mathbf{r}, \boldsymbol{\Omega}, E) + \iint \delta\Sigma_s(\mathbf{r}, E' \rightarrow E, \boldsymbol{\Omega}' \rightarrow \boldsymbol{\Omega}, \omega)\phi_0(\mathbf{r}, \boldsymbol{\Omega}', E')d\boldsymbol{\Omega}'dE', \quad (15)$$

where  $\phi_0(\mathbf{r}, \boldsymbol{\Omega}, E)$  is the neutron flux in the steady state,  $\delta\Sigma_t(\mathbf{r}, E, \omega)$  and  $\delta\Sigma_s(\mathbf{r}, E' \rightarrow E, \boldsymbol{\Omega}' \rightarrow \boldsymbol{\Omega}, \omega)$  are the total and scattering cross section fluctuations in the frequency domain, respectively. These frequency domain cross section fluctuations of a reaction  $x$  are given by the following expansion:

$$\delta\Sigma_x(\mathbf{r}, \omega) = 2\pi \sum_{k=-\infty}^{+\infty} c_k \delta(\omega - k\omega_0), \quad (16)$$

where  $\omega_0$  is the angular frequency of the absorber and  $k$  is an integer. The expansion coefficient,  $c_k$ , needs to be defined for the rotating and vibrating absorbers used in the AKR-2 neutron noise experiments.

For the rotating absorber,  $c_k$  is given by:

$$c_k = \frac{\Delta}{2\pi k} [i \cdot \cos(k\omega_0 t) + \sin(k\omega_0 t)]_{t=a}^{t=b}, \quad (17)$$

where  $\Delta$  = the cross section of the absorber (in the current case, Cadmium),  $a = \frac{R\theta}{v} - \frac{T}{2}$  and  $b = \frac{R\theta}{v} + t_d - \frac{T}{2}$ .  $T$  is the period of the rotation;  $v$  is the velocity of the absorber;  $t_d$  is equal to (the length of the

absorber in the circumferential direction) /  $v$ ;  $R$  and  $\theta$  are defined as shown in Figure 20. As an example,  $\delta\Sigma_x(r, \omega)$  as a function of  $\theta$  is shown in Figure 21 for 1 Hz and  $k = 1$ .

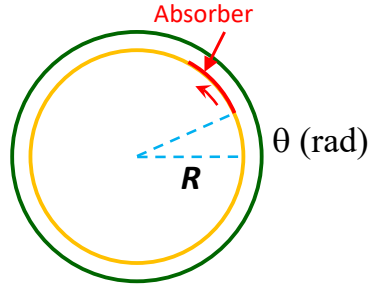


**Figure 20: Rotating absorber.**

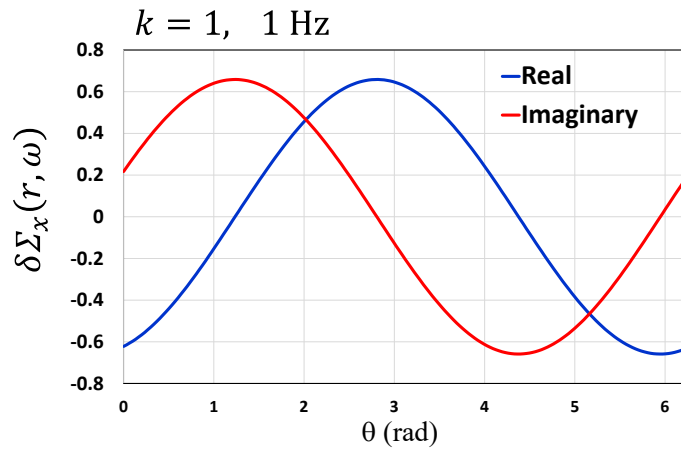


**Figure 21:  $\delta\Sigma_x(r, \omega)$  as a function of  $\theta$ .**

The vibrating absorber in the first campaign moved according to a trapezoidal shape, as shown in Figure 22. For this movement of the vibrating absorber, the expansion coefficient,  $c_k$ , is given by the following equations:

$$1) \quad c_k = \frac{\Delta}{2\pi k} [i \cdot \cos(k\omega_0 t) + \sin(k\omega_0 t)]_{t=a}^{t=b}, \quad 0 < x < D, \quad (18)$$

where  $a = -\frac{x}{v}$  and  $b = t_w + x/v$ ;

$$2) \quad c_k = \frac{\Delta}{2\pi k} \{ [i \cdot \cos(k\omega_0 t) + \sin(k\omega_0 t)]_{t=a}^{t=b} + [i \cdot \cos(k\omega_0 t) + \sin(k\omega_0 t)]_{t=c}^{t=d} \}, \quad D < x < W - D, \quad (19)$$

where  $a = -x/v$ ,  $b = D/v - x/v$ ,  $c = t_w + x/v - D/v$ ,  $d = t_w + x/v$ ;

$$3) \quad c_k = \frac{\Delta}{2\pi k} \{ [i \cdot \cos(k\omega_0 t) + \sin(k\omega_0 t)]_{t=a}^{t=b} + [i \cdot \cos(k\omega_0 t) + \sin(k\omega_0 t)]_{t=c}^{t=d} \}, \quad W - D < x < W \quad (20)$$

where  $a = -T/2$ ,  $b = W/v - x/v - t_m$ ,  $c = x/v - D/v + t_w$ ,  $d = T/2$ .



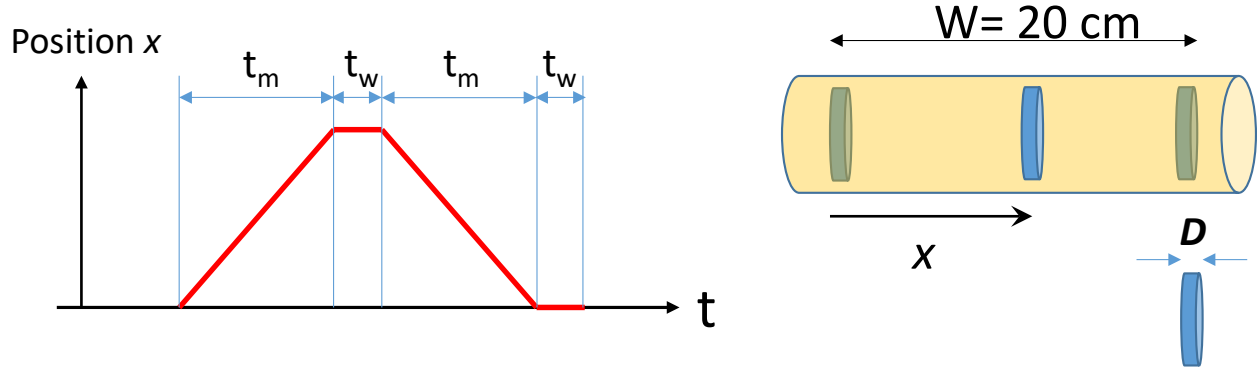


**Figure 22: Movement of the vibrating absorber in the first campaign.**

As an example,  $\delta\Sigma_x(x, \omega)$  as a function of  $x$  is shown in Figure 23 for 0.455 Hz and  $k = 1$ . This frequency corresponds to the experiment No. 22 in the first campaign.

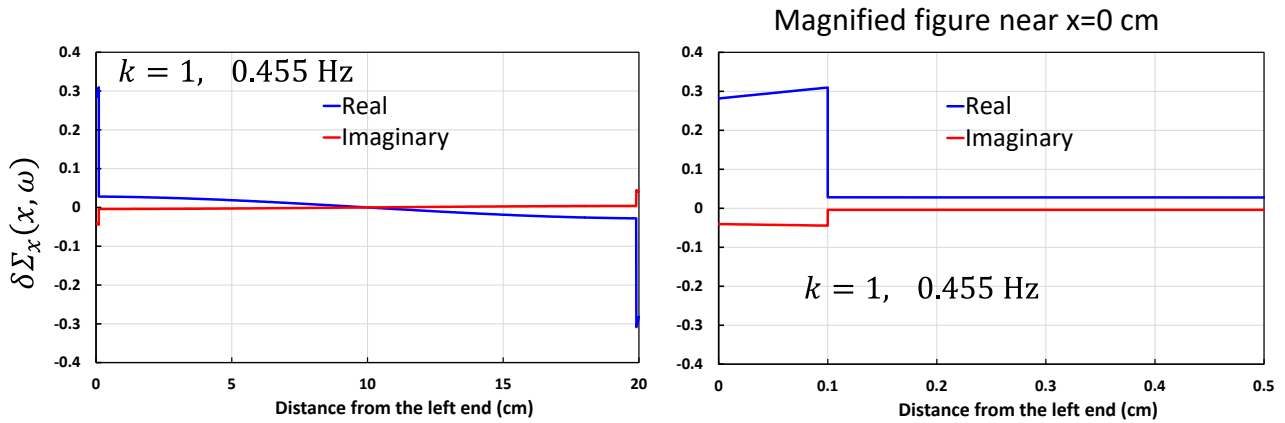


**Figure 23:  $\delta\Sigma_x(x, \omega)$  as a function of  $x$ .**

#### 4.3.2 Modelling of neutron noise sources in the 2<sup>nd</sup> campaign

Whereas the absorber of variable strength was unchanged from the 1st campaign, the location and motion of the vibrating absorber were different in the 2nd campaign. For the simulations of the neutron noise induced by the vibrating absorber in the 2nd campaign, the vibration is assumed to be completely sinusoidal.

The schematic view of the vibrating absorber used in the 2<sup>nd</sup> campaign is shown in Figure 14. In the same manner as in the 1st campaign, the cross-section fluctuation in the frequency domain is expressed by Eq. (16). The expansion coefficients,  $c_k$ , for the vibrating absorber are given below.

When  $0 < x < W$ ,

$$c_k = -\frac{\Delta}{\pi k} \sin \left( k \left( \cos^{-1} \left( \frac{x}{A} - 1 \right) \right) \right), \quad (21)$$

where  $\Delta$  is the cross section of the absorber (in this case, ln).

When  $W < x < 2A$ ,

$$c_k = \frac{\Delta}{2\pi k} \{ [\sin(k\omega_0 t)]_{t=a}^{t=b} + [\sin(k\omega_0 t)]_{t=c}^{t=d} \}, \quad (22)$$

where  $a = -\frac{T}{2\pi} \left( \cos^{-1} \left( \frac{x-W}{A} - 1 \right) \right)$ ,  $b = -\frac{T}{2\pi} \left( \cos^{-1} \left( \frac{x}{A} - 1 \right) \right)$ ,  $c = \frac{T}{2\pi} \left( \cos^{-1} \left( \frac{x}{A} - 1 \right) \right)$ , and  $d = \frac{T}{2\pi} \left( \cos^{-1} \left( \frac{x-W}{A} - 1 \right) \right)$ .

When  $2A < x < 2A + W$ ,

$$c_k = \frac{\Delta}{\pi k} \sin(k\omega_0 a), \quad (23)$$

where  $a = \frac{T}{2\pi} \left( \pi - \cos^{-1} \left( 1 - \frac{x-W}{A} \right) \right)$ . Figure 25 shows  $\text{Re}[\delta\Sigma_x(x, \omega)]$  as a function of  $x$  for 2 Hz,  $A = 3$  cm, and  $k = 1$ . Unlike the 1st campaign,  $\text{Im}[\delta\Sigma_x(x, \omega)] = 0$ .

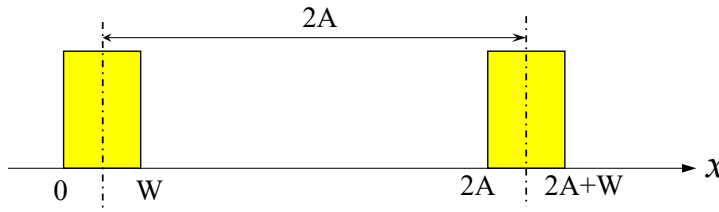


**Figure 24: Schematic view of the vibrating absorber; A = amplitude and W = thickness of the absorber.**

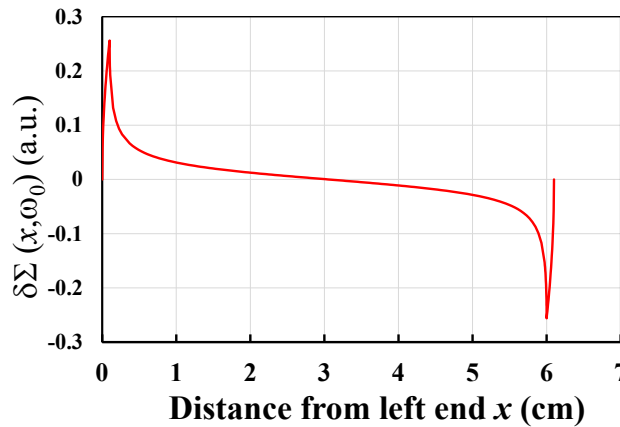


**Figure 25:  $\text{Re}[\delta\Sigma_x(x, \omega)]$  as a function of  $x$  for the case of  $k=1$  and a vibration with frequency = 2 Hz and amplitude = 3 cm.**

#### 4.3.3 Neutron noise simulation scheme

The calculation for the noise transport equation is performed in two steps. In the first step, a criticality calculation is performed for the steady state to obtain the steady state neutron flux  $\phi_0$ . When a particle undergoes a collision in the moving absorber region, the noise source caused by the first term on the right-hand of Eq. (15) is given by the following:

$$S_t(\mathbf{r}, \mathbf{\Omega}, E, \omega) = -\delta\Sigma_t(\mathbf{r}, E, \omega) \frac{W}{\Sigma_t(\mathbf{r}, E)}, \quad (24)$$

where  $W$  = the colliding particle weight. The direction  $\mathbf{\Omega}$  and energy  $E$  of the source term remain unchanged from those of the colliding particle. The noise source caused by the second term on the right-hand of Eq. (15) is given by the following:

$$S_s(\mathbf{r}, \mathbf{\Omega}', E', \omega) = \delta\Sigma_s(\mathbf{r}, E, \omega) \frac{W}{\Sigma_t(\mathbf{r}, E)}, \quad (25)$$

where the direction  $\Omega'$  and energy  $E'$  values are taken after scattering and they are sampled from the scattering law of the absorber nuclide. These noise source data (position, energy, weight, direction) are stored in a file.

After sufficient data are accumulated in the file, the neutron noise source transport calculation is performed. A noise source is taken from the file. Particles are emitted from the noise source site and transported in the calculation domain. After all noise sources are exhausted, the whole calculation is terminated.

#### 4.3.4 Detector arrangement and modelling

The detector arrangement in the MCNP calculations is shown in Figure 26 for the 1<sup>st</sup> campaign and in Figure 27 for the 2<sup>nd</sup> campaign. The detector sizes and locations were adjusted from the actual ones in order to detect more noise particles in the Monte Carlo calculations. Continuous energy cross section with JENDL-4.0 nuclear data were used. Noise source particles with complex-valued weights were emitted from the absorber. The particles were transported in the calculation domain. Reaction rates of the complex-valued weights with the detector materials were calculated at each detector position.

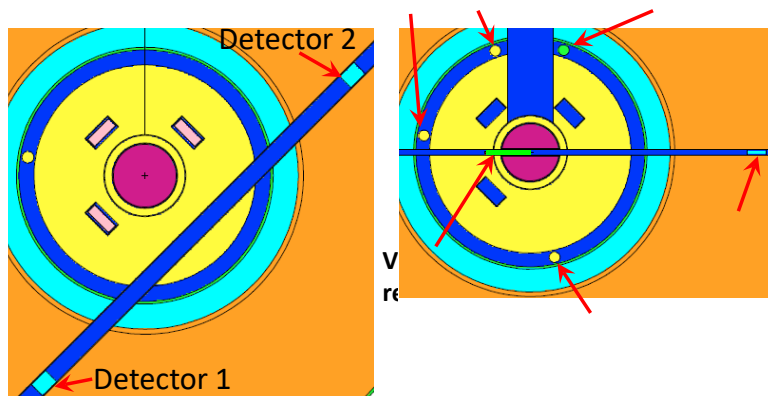


Figure 26: Detector arrangement in the MCNP model for the first campaign.

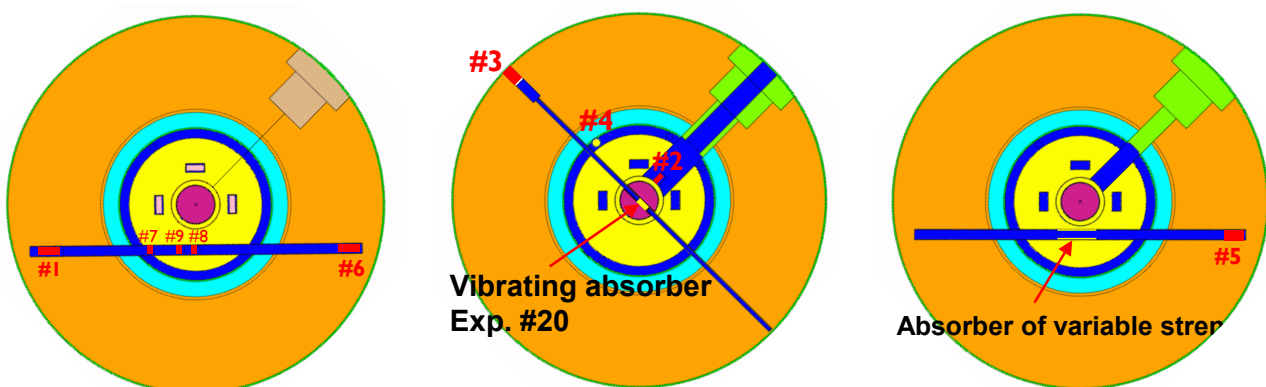


Figure 27: Detector arrangement in the MCNP model for the 2<sup>nd</sup> campaign.

### 4.4 Comparison between simulations and measurements

Experiments carried out in the three neutron noise campaigns at AKR-2 have been simulated using CORE SIM+ and the stochastic neutron noise solver developed in the MCNP code. The results are compared with the measured neutron noise.

#### 4.4.1 Simulations of experiments from the 1<sup>st</sup> campaign

Two experiments from the first campaign at AKR-2 have been simulated, namely experiment 7 and experiment 22 [7]. The main purpose was to gain experience and knowledge in order to improve the modelling and the measurements in the subsequent campaigns. The results are expressed in terms of PSD (see section 2). The detector 1 is selected as reference and the values of the CPSD amplitude are normalized using the amplitude of the CPSD between the detectors 2 and 1. The positions of the detectors are shown, e.g., in Figure 1.

In experiment 7, an absorber rotates at a frequency of 1 Hz (see Figure 20). The calculated and measured neutron noise are compared in Figure 28. The behaviour of the CPSD amplitudes with respect to the detectors calculated with MCNP is similar to the behaviour obtained from the measurements, although differences in values can be found. On the other hand, CORE SIM+ predicts a flat trend of the noise, which may be due to the limitations of diffusion theory. For the neutron noise phase, there are large discrepancies between calculations and measurements.

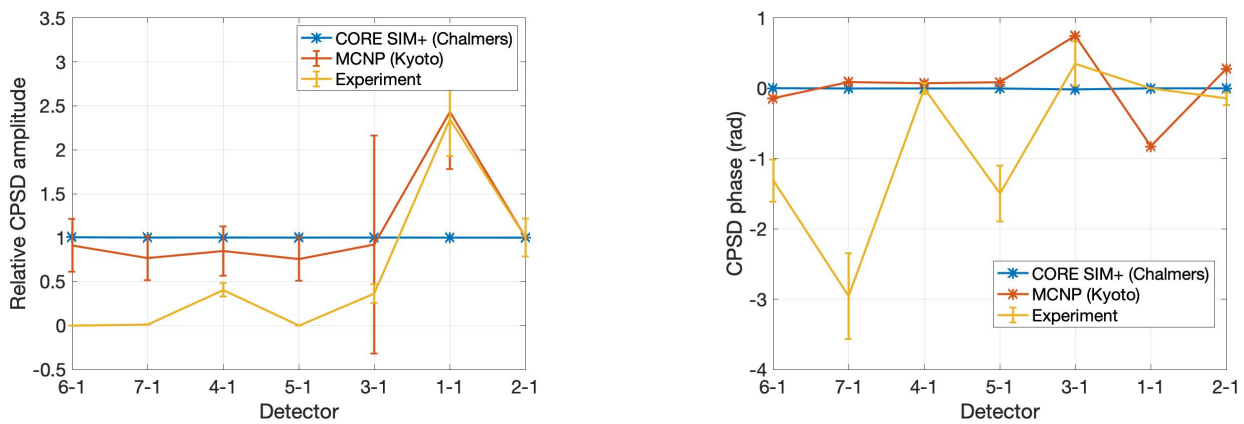


**Figure 28: Experiment 7 (rotating absorber) in the first campaign at AKR-2; neutron noise amplitude (left) and phase (right).**

In experiment 22, an absorber is oscillated in the reactor core according to a trapezoidal shape (see Figure 22). The calculated and measured neutron noise is compared in Figure 29. The neutron noise (amplitude and phase) calculated with MCNP and CORE SIM+ is similar, except for the amplitude associated with detector 3. However, the difference between calculations and measurements are significant.

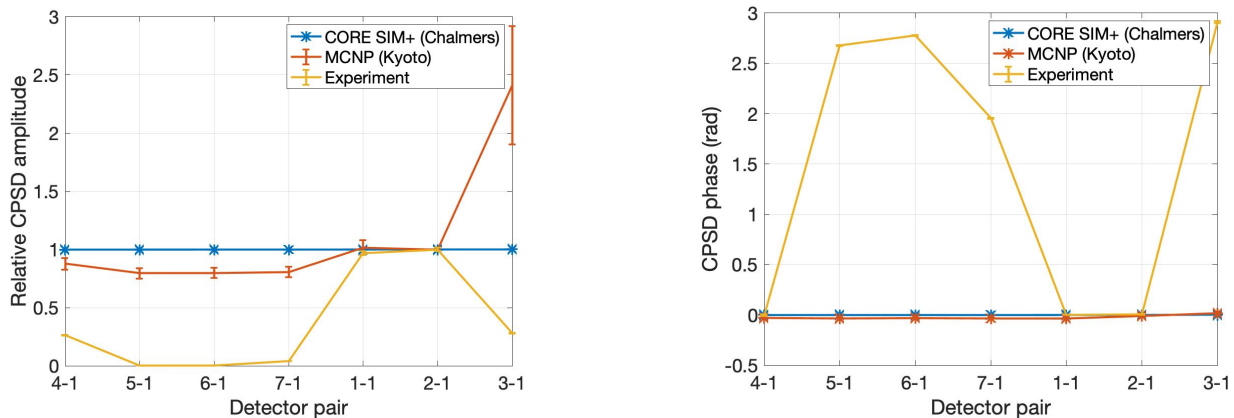


**Figure 29: Experiment 22 (vibrating absorber) in the first campaign at AKR-2; neutron noise amplitude (left) and phase (right).**

#### 4.4.2 Simulations of experiments from the 2<sup>nd</sup> campaign

Two experiments carried out in the second campaign at AKR-2 have been simulated, namely experiment 1 and experiment 20 [8]. The neutron noise amplitude for the detector  $i$  is obtained from the APSD of the detector  $i$  divided by the CPSD between the detector  $i$  and the reference detector 8. The neutron noise phase is derived from the CPSD between the detector  $i$  and the detector 1. The positions of the detectors are shown, e.g., in Figure 2.

In experiment 1, an absorber rotates at a frequency of 2 Hz. The calculated and measured neutron noise are compared in Figure 30. The experimental behaviour of the noise (amplitude and phase) for detectors 8, 9 and 7 is reproduced by both MCNP and CORE SIM+ to some extent.

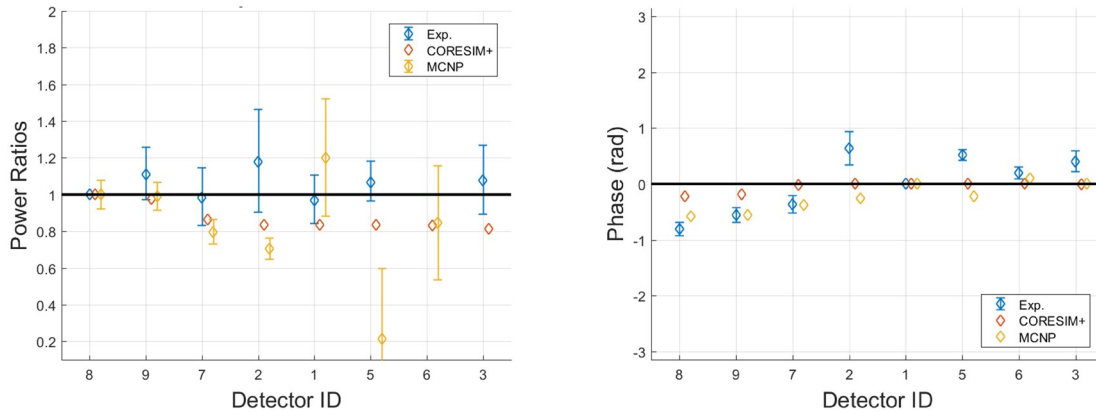


**Figure 30: Experiment 1 (rotating absorber) in the second campaign at AKR-2; neutron noise amplitude (left) and phase (right).**

In experiment 20, an absorber vibrates in the core with a frequency of 2 Hz and an amplitude of 3 cm. The calculated and measured neutron noise is compared in Figure 31. The noise amplitude calculated with MCNP and CORE SIM+ is close to unity for most of the detectors and agrees with the experimental results. For the detector 3, the experimental power ratio is equal to 5.8 and is not included in the plot; the MCNP calculation can partly capture such an increase of neutron noise.

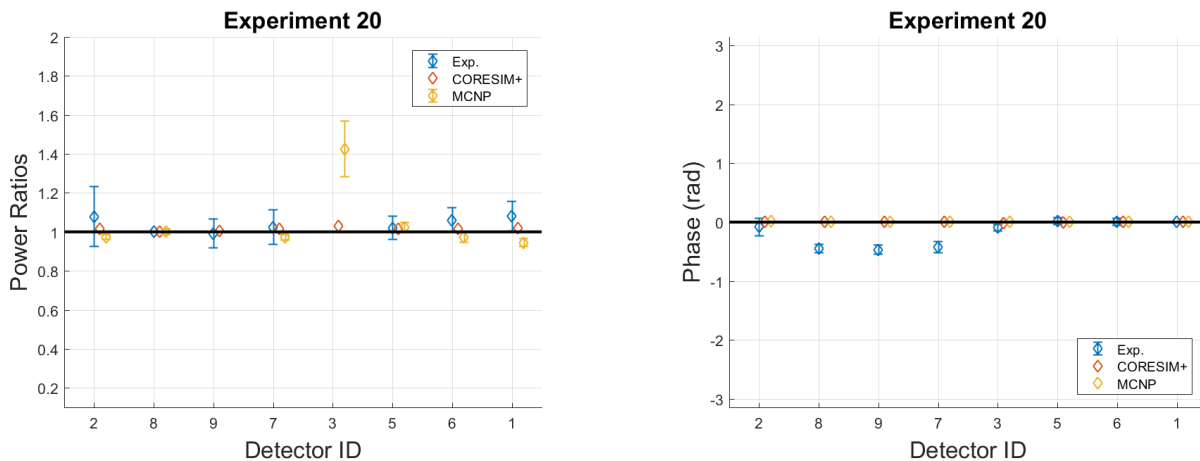


**Figure 31: Experiment 20 (vibrating absorber) in the second campaign at AKR-2; neutron noise amplitude (left) and phase (right). For detector 3, the experimental power ratio is equal to 5.8.**

#### 4.4.3 Simulations of experiments from the 3<sup>rd</sup> campaign

Two experiments carried out in the third campaign at AKR-2 have been simulated, i.e., experiment M02 (or experiment 3) and experiment M17 (or experiment 23) [9]. The neutron noise amplitude for the detector  $i$  is obtained from the APSD of the detector  $i$  divided by the CPSD between the detector

$i$  and the reference detector 1. The neutron noise phase is derived from the CPSD between the detector  $i$  and the detector 1. The positions of the detectors are shown, e.g., in Figure 3.

In experiment M02, an absorber rotates at a frequency of 2 Hz. The calculated and measured neutron noise are compared in Figure 32. The behaviour of the neutron noise (amplitude and phase) obtained from the measurements and from the CORE SIM+ simulation is similar, although differences are found, e.g., for detectors 7, 4 and 6.

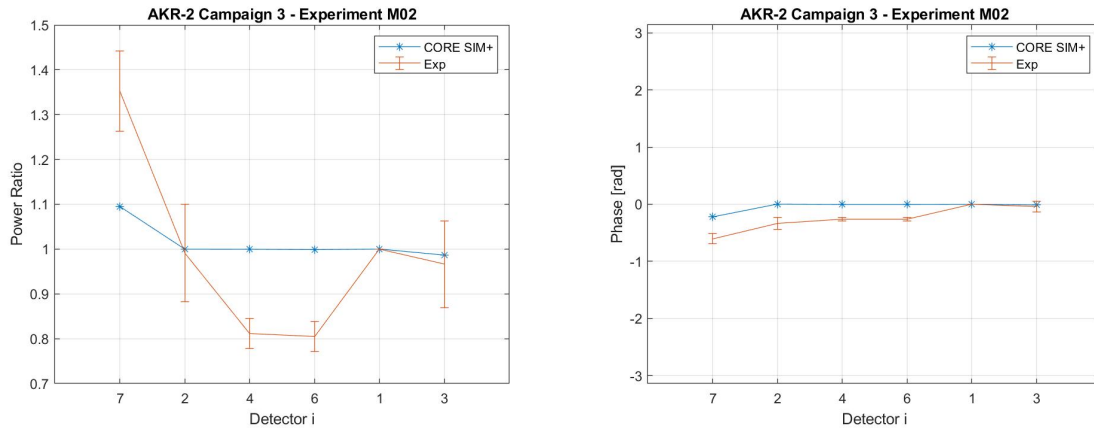


**Figure 32: Experiment M02 (rotating absorber) in the third campaign at AKR-2; neutron noise amplitude (left) and phase (right).**

In experiment M17, an absorber vibrates in the core with a frequency of 2 Hz and an amplitude of 3 cm. The calculated and measured neutron noise is compared in Figure 33. For the noise amplitude, the values calculated with CORE SIM+ agree with the values estimated from the measurements, except at the positions of detector 2 (small difference) and detector 3 (large difference). These results are consistent with the results obtained in campaign 2, see Figure 31.

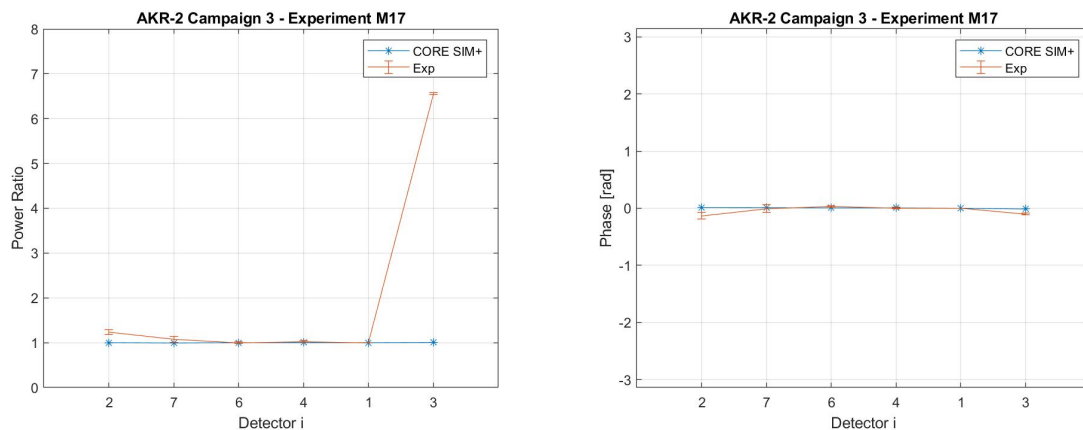


**Figure 33: Experiment M17 (vibrating absorber) in the third campaign at AKR-2; neutron noise amplitude (left) and phase (right).**

## 4.5 Uncertainty analysis for the CORE SIM+ simulations

To quantify the uncertainties associated with the CORE SIM+ calculations, the GRS (Gesellschaft für Anlagen und Reaktorsicherheit) methodology [29] has been applied. This methodology is a non-parametric statistical method based on well-established concepts from probability and statistics theory and allows to quantify the uncertainty of a code output variable in terms of statistical tolerance limits. The tolerance limits are obtained from a series of calculations in which code input and modelling parameters are varied according to their uncertainties. The number of calculations and thus the size of the samples that are built for the code output variables from the calculations, define the probability content and confidence level of the tolerance limits, as given by the Wilks' formula



[30]. In the current application, the 1<sup>st</sup> order Wilks' formula for two-sided limits is selected. This formula requires samples of 93 elements (93 code runs) to estimate tolerance limits (through the smallest and largest value of the sample) with 95% of probability content and with a 95% of confidence (which are typical values used for nuclear safety analysis).

#### 4.5.1 Uncertainty analysis for the 1<sup>st</sup> campaign

The two neutron noise experiments from the first campaign at AKR-2 have been considered, i.e., experiment 7 (with a rotating absorber equivalent to an absorber of variable strength) and experiment 22 (with a vibrating absorber).

The uncertainty analysis is mainly based on the methodology described in [31]. The neutron noise uncertainty ranges are determined by propagating the uncertainties of the input and modeling parameters such as selected nuclear data, rotation frequency for the rotating absorber or moving and waiting time for the vibrating absorber, and location of noise source within their uncertainty ranges, as summarized in Table 4.

The 748 nuclear data considered for the uncertainty analysis include the microscopic cross sections for <sup>235</sup>U, <sup>238</sup>U, <sup>1</sup>H, <sup>12</sup>C and <sup>16</sup>O in the case of the reactions (n, el), (n, inl), (n, 2n), (n, capture), and (n, f), and the quantities  $\bar{\nu}$  and  $\chi$ . The uncertainties in these quantities are used to generate the uncertainties in the 2-energy group macroscopic nuclear data needed for the CORE SIM+ calculations, i.e., the fast and thermal diffusion coefficient ( $D$ ), the fast and thermal absorption cross-section ( $\Sigma_{abs}$ ), the fast and thermal nu-fission cross-section ( $\nu\Sigma_{fiss}$ ), and the removal cross-section ( $\Sigma_{rem}$ ). This procedure is based on computations with the Serpent Monte Carlo code, in which the native ENDF/B-VII.0 ACE files, the ENDF/B-VII.1 covariances, and the Scale 6.0 energy group structure (44 groups) are used.

The other input parameters and their uncertainties are derived from expert judgement. A total of 93 CORE SIM+ runs are executed to meet the 95%/95% criterion following 1<sup>st</sup> order Wilks' formula for two-sided limits.

Figures 34 and 35 show the uncertainties of the neutron noise calculated at the detector locations for Experiment 7 (with a rotating absorber) and Experiment 8 (with a vibrating absorber), respectively. These uncertainties are much smaller than the experimental uncertainties (see Figures 28 and 29) and as such cannot explain the discrepancies between the computational and measured quantities of interest.

**Table 4: Uncertainties for selected input and modelling parameters for the simulations related to the 1<sup>st</sup> experimental campaign in AKR-2**

No.	Parameter		Distribution	Unit	Mean	Lower/Upper limit
1~748	Nuclear data uncertainties <sup>4</sup>					
749 <sup>1</sup>	Moving time		Uniform	sec.	1	0.95/1.05
	Waiting time		Uniform	sec.	0.1	0.095/0.105
750 <sup>2</sup>	Oscillating frequency		Uniform	Hz	1	0.95/1.05
751	Location of noise source	Along the experimental channel	Uniform	Mesh	Ideal location	-1/+1 <sup>3</sup>
752		Along the core center line	Uniform	Mesh	Ideal location	-1/+1 <sup>3</sup>

1: These parameters are considered in the case of the vibrating absorber.

2: This parameter is considered in the case of the rotating absorber.

3: -1/+1 correspond to -1.4/+1.4 cm for the vibrating absorber and -1/+1 cm for the rotating absorber.

4: Nuclear data uncertainties are treated in a distinct manner, as explained above.

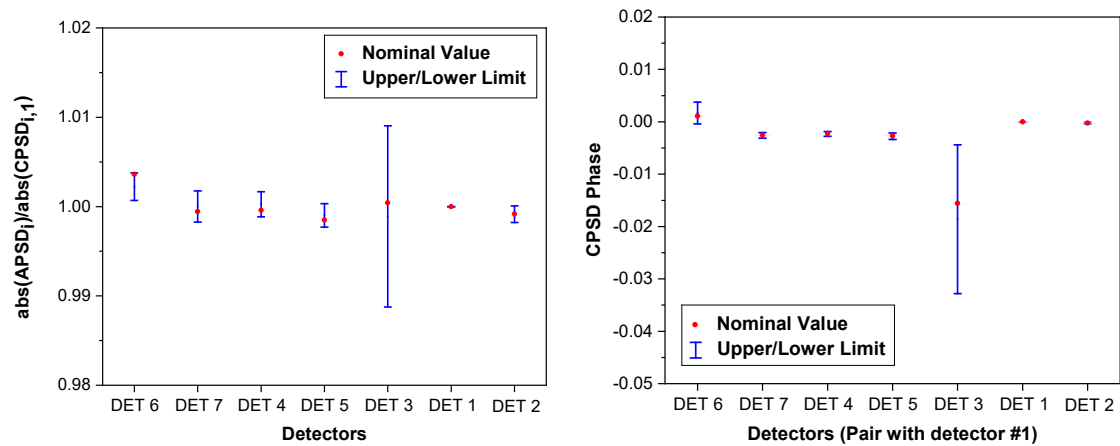


**Figure 34: Experiment 7 (rotating absorber) in the 1<sup>st</sup> campaign at AKR-2; uncertainties of neutron noise amplitude (left) and phase (right) calculated with CORE SIM+.**

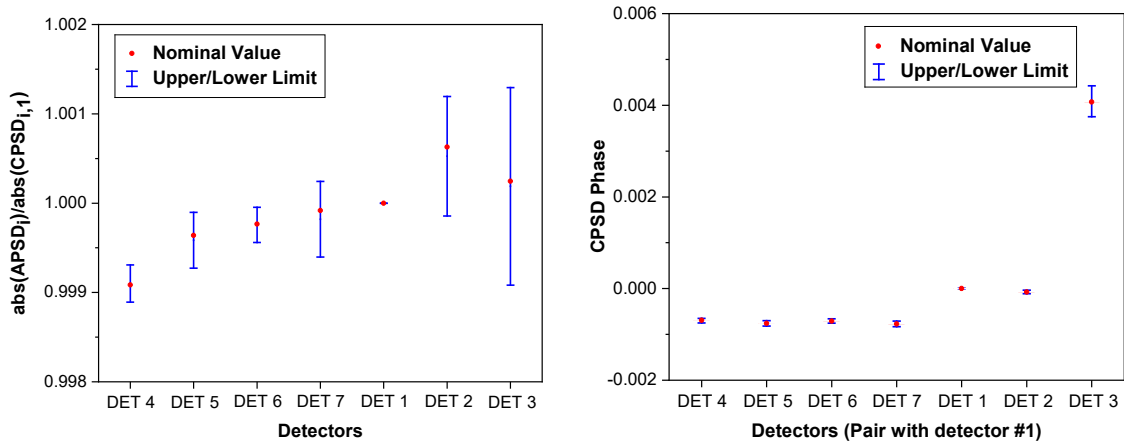


**Figure 35: Experiment 22 (vibrating absorber), in the 1<sup>st</sup> campaign at AKR-2; uncertainties of neutron noise amplitude (left) and phase (right) calculated with CORE SIM+.**

#### 4.5.2 Uncertainty analysis for the 2<sup>nd</sup> campaign

The uncertainty analysis of the CORE SIM+ simulations performed for the 2<sup>nd</sup> campaign is identical to the analysis discussed for the 1<sup>st</sup> campaign. The experiments selected in the 2<sup>nd</sup> campaign are Experiment 1 (with a rotating absorber equivalent to an absorber of variable strength) and Experiment 20 (with a vibrating absorber). Different from the 1<sup>st</sup> campaign, the movement of the vibrating absorber is sinusoidal. Table 5 summarizes the input uncertainties considered in the analysis.

Figures 36 and 37 show the uncertainties estimated for the CORE SIM+ simulations of experiment 1 and experiment 20, respectively. Similar to the uncertainty analysis for the 1<sup>st</sup> campaign, the uncertainties associated with the simulations are small, so they cannot explain the discrepancies between the computational and measured quantities of interest (compare Figures 36 and 37 to Figures 30 and 31).



**Table 5: Uncertainties for selected input parameters in the simulations for the second AKR-2 experimental campaign**

No.	Parameter		Distribution	Unit	Nominal value	Standard deviation (Lower/Upper limit <sup>1</sup> )
1	Oscillating frequency		Normal	Hz	2	5%
2	Location of noise source	Along the experimental channel	Uniform	Mesh	Ideal location	-1/+1 <sup>2</sup>
3		Along the core center line	Uniform	Mesh	Ideal location	-1/+1 <sup>3</sup>

1: Standard deviation in the case of a normal distribution or lower and upper limits in the case of a uniform distribution.

2: -1/+1 correspond to -0.47/+0.47 cm for the vibrating absorber and -1/+1 cm for the rotating absorber.

3: -1/+1 correspond to -0.47/+0.47 cm for vibrating absorber. This parameter is not considered in the case of the rotating absorber.

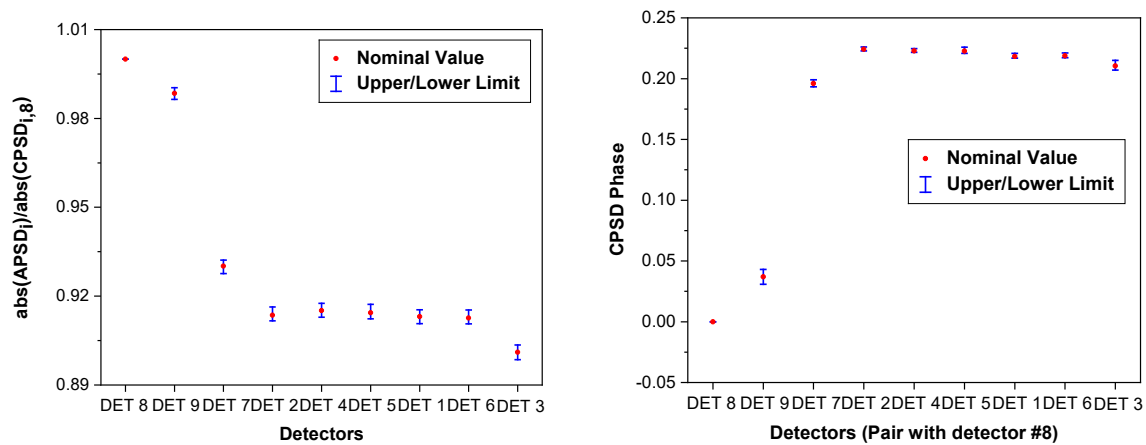


**Figure 36: Experiment 1 (rotating absorber) in the 2nd campaign at AKR-2; uncertainties of neutron noise amplitude (left) and phase (right) calculated with CORE SIM+.**

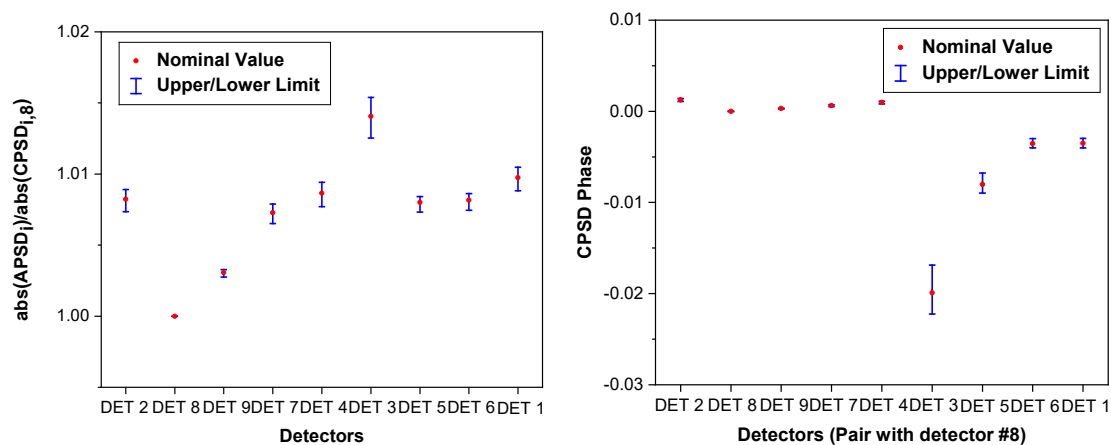


**Figure 37: Experiment 20 (vibrating absorber) in the 2nd campaign at AKR-2; uncertainties of neutron noise amplitude (left) and phase (right) calculated with CORE SIM+.**

## 5 COLIBRI experiments and simulations

The solvers CORE SIM+, FEMFUSION, PARCS, TRIPOLI-4®, NOISE-SN and APOLLO3® have been used to model and simulate neutron noise experiments performed in the first and second COLIBRI campaigns.

### 5.1 COLIBRI experiments

Two neutron noise experimental campaigns have been carried out using the device COLIBRI that allows to oscillate fuel rods in the research reactor CROCUS (EPFL).

#### 5.1.1 CROCUS reactor

CROCUS is a pool type, water moderated, zero power reactor at EPFL. It consists of an upper and a lower grid, and two zones with different types of fuel elements. In the inner zone, there are 336 UO<sub>2</sub> fuel elements with an enrichment of 1.806 wt.% and a pitch of 1.837 cm. In the outer zone, there are 172 metallic uranium fuel elements with an enrichment of 0.947 wt.% and a pitch of 2.917 cm. The pool consists of an aluminium vessel. The reactor is controlled either by adjusting the water level or by using control rods and is also equipped with cadmium safety blades.

#### 5.1.2 COLIBRI device

The COLIBRI device is used to perform experiments with oscillating fuel rods in the CROCUS reactor at EPFL, see Figure 38. It is located at the reactor pool NW edge and can move up to 18 fuel rods (according to a 3 x 6 arrangement). The oscillations are induced using a stepper motor and a rotary to linear movement coupling, with rotation/oscillation frequency from 0.01 Hz (at which point the motor jitters due to a limited number of poles) up to 2 Hz. The coupling also allows for adjustment of the oscillation amplitude from 0 mm to 2.5 mm. The motor rotation is controlled and monitored externally. During its operation, the rate and the position of rotation are monitored by two devices: a continuous cable position system, recording the position of the bottom part of the oscillator (e.g., see Figure 39; the position at the bottom might be different from the top part because of the sway associated with the inertia of the fuel rods and the waves in the water of the pool) and an inductive captor device, providing four pulses per single motor rotation (e.g., see Figure 40). The latter is also available for external devices in order to synchronize the measurements.

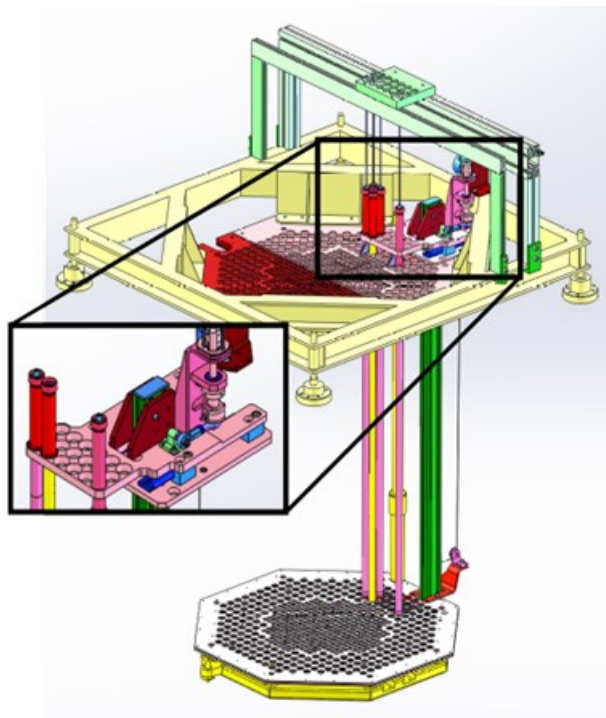
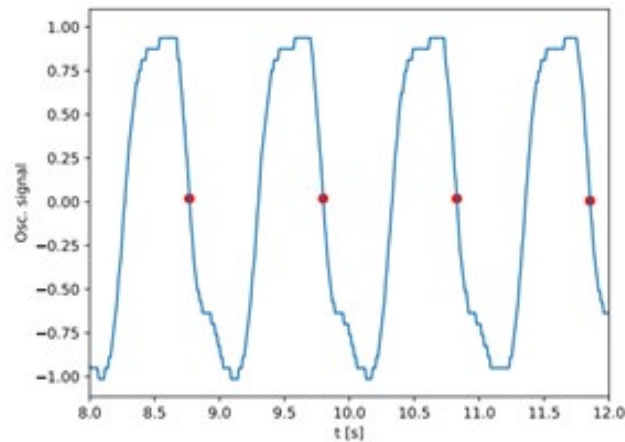
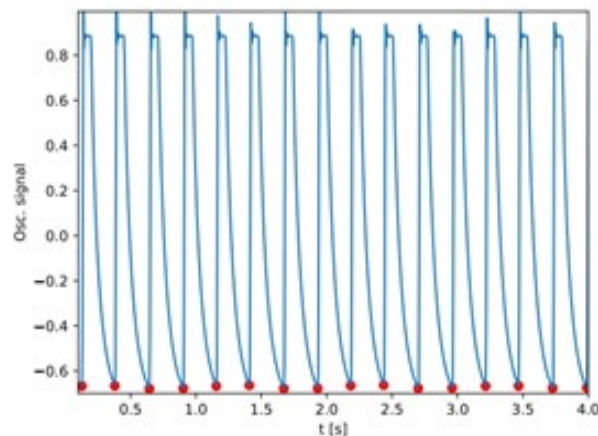


Figure 38: CAD view of the COLIBRI device with the close-up of fuel holding and moving part.



**Figure 39: COLIBRI cable position in time for 1Hz and 1mm amplitude oscillation.**



**Figure 40: COLIBRI inductive captor signal at 1 Hz oscillation.**

### 5.1.3 First experimental campaign

The first experimental campaign was performed in September 2018. It was partly devoted to the qualification and the development of the multiple data acquisition systems. However, for comparison with simulations, measurement data obtained from the industry standard ISTEK Sigma system was used. Eleven detectors were set at in-core and reflector positions (see Figure 41). Most of the experiments were performed at reactor power of  $\sim 100$  mW and 20 measurements were performed in total. Measurements no. 12 and 13 were selected as reference. The oscillation amplitude for both cases was  $\pm 2$  mm. The oscillation frequency was 0.1 Hz for measurement no. 12 and 1.0 Hz for measurement no. 13. A more detailed description of the first experimental campaign is given in [7]. Detector no. 5 was selected as a reference detector to calculate amplitude and phase of the neutron noise.

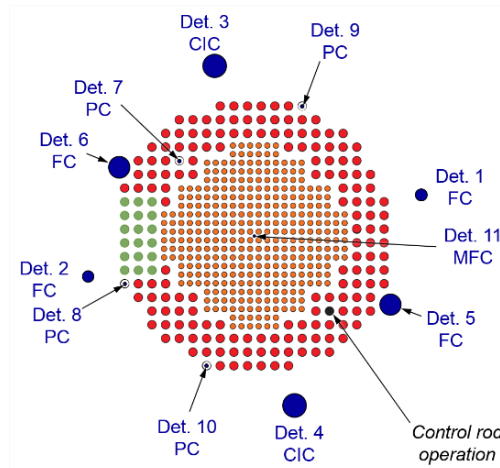


**Figure 41: Detectors and their position in the first CROCUS campaign; the fuel rods oscillating with COLIBRI are in green.**

As discussed in section 2.1, the analysis of re-sampled data is performed in two steps:

- The initial analysis includes assumptions about data normality and correlations to estimate true values and usable data ranges. Mean and standard deviation are calculated assuming normal distribution. These results are summarized in 2<sup>nd</sup> and 3<sup>rd</sup> rows in Tables 6 to 9.
- A detailed, statistical approach without assumptions, with final evaluation of maximum likelihood value and 1-sigma confidence interval boundaries (68.27%). The maximum likelihood values and the relative differences of the upper and lower boundaries from this value are given in the last three rows in Tables 6 and 8 for the spectral power ratio and in Tables 7 and 9 for the phase angle difference.

**Table 6: Measurement no. 12 from 1st COLIBRI campaign; spectral power ratio with respect to detector 5**

Det. No.	3	4	5	6	7	8	9	10
Mean	0,853	1,246	1,000	1,506	1,620	1,071	1,170	1,265
Rel. Std.	9,70E-02	4,94E-05	1,23E-04	1,63E-05	4,88E-05	2,60E-04	8,84E-04	4,39E-04
Max. likelihood	0,852	1,244	1,000	1,504	1,624	1,082	1,176	1,268
Lower bound rel. diff.	1,42E-02	1,31E-02	0,00E+00	1,44E-02	4,13E-02	5,46E-02	3,96E-02	3,00E-02
Upper bound rel. diff.	1,29E-02	1,45E-02	0,00E+00	1,59E-02	4,48E-02	5,52E-02	3,70E-02	2,97E-02

**Table 7: Measurement no. 12 from 1<sup>st</sup> COLIBRI campaign; phase angle difference with respect to detector 5**

Det. No.	3	4	5	6	7	8	9	10
Mean [rad]	-9,19E-03	-1,74E-02	0,00E+00	1,19E-01	-3,64E-01	-2,40E-01	-6,69E-02	-2,37E-02
Std. [rad]	3,77E-04	8,80E-04	7,82E-06	9,82E-03	2,37E-02	1,66E-02	4,04E-03	1,19E-03
Max. likelihood [rad]	-8,58E-03	-1,80E-02	0,00E+00	1,22E-01	-3,66E-01	-2,40E-01	-6,85E-02	-1,81E-02
Lower bound diff. [rad]	1,15E-02	1,06E-02	0,00E+00	1,48E-02	2,94E-02	4,85E-02	2,85E-02	3,10E-02
Upper bound diff. [rad]	1,03E-02	1,17E-02	0,00E+00	9,89E-03	3,28E-02	4,60E-02	3,12E-02	2,23E-02

**Table 8: Measurement no. 13 from 1<sup>st</sup> COLIBRI campaign; spectral power ratio with respect to detector 5**

Det. No.	3	4	5	6	7	8	9	10
Mean	0,862	1,266	1,000	1,632	1,207	0,734	1,103	1,313
Rel. Std.	4,53E-04	4,63E-04	4,42E-04	5,46E-04	8,23E-03	2,89E-02	5,81E-03	3,49E-03
Max. likelihood	0,860	1,264	1,000	1,632	1,208	0,739	1,101	1,310
Lower bound rel. diff.	1,32E-02	1,30E-02	0,00E+00	1,56E-02	5,81E-02	1,11E-01	4,95E-02	3,90E-02
Upper bound rel. diff.	1,60E-02	1,49E-02	0,00E+00	1,53E-02	5,87E-02	1,05E-01	5,05E-02	4,00E-02

**Table 9: Measurement no. 13 from 1<sup>st</sup> COLIBRI campaign; phase angle difference with respect to detector 5**

Det. No.	3	4	5	6	7	8	9	10
Mean [rad]	-1,69E-01	-1,59E-01	0,00E+00	7,07E-02	-1,53E-01	-1,28E-01	-2,38E-01	-1,74E-01
Std. [rad]	5,26E-05	8,55E-05	1,97E-05	2,97E-05	5,62E-04	5,02E-03	8,42E-04	2,84E-04
Max. likelihood [rad]	-1,70E-01	-1,57E-01	0,00E+00	7,14E-02	-1,50E-01	-1,41E-01	-2,40E-01	-1,69E-01
Lower bound diff. [rad]	1,46E-02	1,57E-02	0,00E+00	1,76E-02	6,25E-02	1,09E-01	5,02E-02	4,72E-02
Upper bound diff. [rad]	1,58E-02	1,34E-02	0,00E+00	1,55E-02	6,20E-02	1,39E-01	5,62E-02	3,83E-02

#### 5.1.4 Second experimental campaign

The second experimental campaign was performed in October 2019. Compared to the first campaign, the total number of detectors was increased from 10 to 16 (see Figure 42). The data acquisition system for pulsed detectors was also changed: instead of ISTECA Sigma, a CAEN V2495 FPGA logic board was used as a counter, in conjunction with a communication board. Several shortcomings, identified during the first campaign were addressed, i.e.:

- increase of the measurement time, to provide better statistics;
- detectors located at both sides of the region of the oscillating fuel rods, to observe the phase shift;
- testing of measurement repeatability.

In addition, oscillations were performed not only with the fully filled COLIBRI oscillator, but partially filled as well. A more detailed description of the second experimental campaign is given in [8].

In this campaign, detector no. 12 was selected as the reference detector, and measurements 7 and 8 were selected for validation, which are equivalent in terms of oscillation frequency and amplitude to measurements 12 and 13 from the first campaign, respectively. Experiments similar to measurement no. 7 and 8 were repeated, and repeatability was shown. The analysis follows the same 2-step strategy described for the first campaign (see section 5.1.3). The results for the spectral power ratio are summarized in Table 10 (experiment 7) and in Table 12 (experiment 8). The results for the phase angle difference include only the first step of the analysis and are given in Table 11 (experiment 7) and Table 13 (experiment 8).

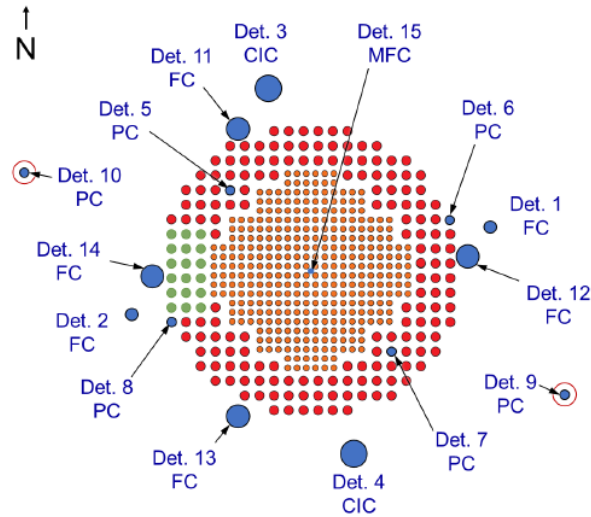


**Figure 42: Detectors and their position in the second CROCUS campaign; the fuel rods oscillating with COLIBRI are in green.**

**Table 10: Measurement no. 7 from 2nd COLIBRI campaign; spectral power ratio with respect to detector 12**

Det. No.	1	2	3	4	5	6	7	8	9	10	11	12	13	14	15
Mean	1,585	2,816	1,136	0,970	1,066	1,005	0,948	0,634	0,942	2,339	1,084	1,000	1,101	0,374	0,999
Rel. Std.	2,58E-01	1,18E-01	2,21E-02	1,76E-02	6,63E-02	1,84E-02	8,23E-02	4,66E-02	1,54E-01	1,85E-02	7,40E-03	2,19E-02	8,23E-03	4,39E-02	1,84E-01
Max. likelihood	2,442	3,321	1,210	0,982	1,184	1,025	1,081	0,696	1,371	2,279	1,073	1,000	1,076	0,406	1,632
Lower bound rel. diff.	1,99E-01	1,49E-01	1,25E-01	8,93E-02	1,55E-01	8,42E-02	1,48E-01	1,06E-01	1,57E-01	7,72E-02	5,24E-02	0,00E+00	5,40E-02	1,24E-01	2,03E-01
Upper bound rel. diff.	2,48E-01	1,74E-01	1,64E-01	9,84E-02	1,93E-01	8,40E-02	2,00E-01	1,17E-01	2,01E-01	7,92E-02	5,56E-02	0,00E+00	5,78E-02	1,32E-01	2,54E-01

**Table 11: Measurement no. 7 from 2nd COLIBRI campaign; phase angle difference with respect to detector 12**

Det. No.	1	2	3	4	5	6	7	8	9	10	11	12	13	14	15
Mean [rad]	2,95E-02	3,00E-01	5,99E-02	4,67E-02	1,41E-01	7,06E-03	1,17E-01	1,00E-01	1,35E-01	2,26E-01	3,73E-02	0,00E+00	6,83E-02	9,37E-01	9,67E-02
Std. [rad]	1,70E-01	3,29E-02	7,87E-03	4,00E-03	2,06E-02	6,12E-03	2,46E-02	1,59E-02	4,44E-02	1,03E-02	2,27E-03	2,94E-03	3,23E-03	4,75E-02	8,66E-02
Max. likelihood [rad]	1,42E-01	3,64E-01	5,06E-02	5,08E-02	1,10E-01	1,79E-02	1,39E-01	1,13E-01	7,86E-02	2,08E-01	3,42E-02	0,00E+00	5,87E-02	8,95E-01	-4,75E-02
Lower bound diff. [rad]	1,55E+00	9,81E-01	5,82E-01	4,10E-01	7,86E-01	4,12E-01	8,06E-01	6,27E-01	8,97E-01	4,12E-01	2,81E-01	0,00E+00	2,90E-01	5,88E-01	1,20E+00
Upper bound diff. [rad]	1,70E+00	8,73E-01	6,02E-01	3,93E-01	7,94E-01	4,15E-01	7,56E-01	6,35E-01	9,00E-01	4,50E-01	2,68E-01	0,00E+00	2,69E-01	6,37E-01	1,35E+00



**Table 12: Measurement no. 8 from 2nd COLIBRI campaign; spectral power ratio with respect to detector 12**

Det. No.	1	2	3	4	5	6	7	8	9	10	11	12	13	14	15
Mean	0,996	3,363	1,164	1,110	1,145	1,061	1,086	0,464	1,073	2,629	1,094	1,000	1,134	0,135	1,067
Rel. Std.	2,30E-02	1,76E-03	9,84E-05	9,74E-05	1,58E-03	3,60E-04	1,80E-03	1,89E-03	2,18E-03	3,17E-04	1,21E-04	2,65E-05	1,25E-04	6,49E-03	5,93E-03
Max. likelihood	1,003	3,356	1,164	1,111	1,142	1,059	1,083	0,465	1,070	2,626	1,093	1,000	1,135	0,135	1,067
Lower bound diff. rel.	1,19E-01	2,95E-02	7,15E-03	7,92E-03	2,89E-02	1,41E-02	3,03E-02	3,45E-02	3,33E-02	1,38E-02	8,94E-03	0,00E+00	1,15E-02	6,58E-02	5,96E-02
Upper bound diff. rel.	1,11E-01	3,37E-02	7,83E-03	7,13E-03	3,21E-02	1,72E-02	3,51E-02	3,14E-02	3,90E-02	1,57E-02	1,02E-02	0,00E+00	8,41E-03	5,81E-02	5,71E-02

**Table 13: Measurement no. 8 from 2nd COLIBRI campaign; phase angle difference with respect to detector 12**

Det. No.	1	2	3	4	5	6	7	8	9	10	11	12	13	14	15
Mean [rad]	1,05E-01	2,33E-01	2,06E-02	3,56E-02	1,73E-01	1,30E-01	1,60E-01	2,74E-01	1,36E-01	2,02E-01	1,91E-02	0,00E+00	3,16E-02	-	1,43E-01
Std. [rad]	4,21E-03	1,55E-04	2,12E-05	2,28E-05	1,57E-04	2,50E-05	1,68E-04	2,09E-04	2,76E-04	1,73E-05	2,61E-06	2,53E-06	1,49E-06	9,79E-04	9,56E-04
Max. likelihood [rad]	1,10E-01	2,27E-01	2,01E-02	3,48E-02	1,70E-01	1,29E-01	1,56E-01	2,76E-01	1,38E-01	2,03E-01	1,87E-02	0,00E+00	3,25E-02	-	1,46E-01
Lower bound diff. [rad]	1,42E-01	3,01E-02	8,47E-03	8,07E-03	3,17E-02	1,65E-02	3,29E-02	4,26E-02	4,20E-02	1,82E-02	1,08E-02	0,00E+00	1,29E-02	6,96E-02	7,37E-02
Upper bound diff. [rad]	1,29E-01	4,23E-02	8,90E-03	9,05E-03	3,65E-02	1,89E-02	3,96E-02	3,85E-02	3,71E-02	1,55E-02	1,11E-02	0,00E+00	1,02E-02	7,35E-02	6,59E-02

## 5.2 CORE SIM+ modelling

A model of the CROCUS reactor has been developed for CORE SIM+. The fuel rod oscillations driven by the COLIBRI device are described as localized fluctuations of macroscopic cross sections. As verification test, the model was used to estimate the point-kinetic zero-power reactor transfer function for CROCUS and the result has been compared with an analytical solution.

### 5.2.1 Modelling of the reactor and neutron noise source

A simplified 3-D model of the CROCUS reactor core is used, as illustrated in Figure 43. The model consists of three homogenized regions, i.e., the inner fuel region, the outer fuel region, and the water reflector. The macroscopic neutron cross sections are generated from Monte Carlo calculations and are given according to 2 energy groups. For each region two sets of cross sections are generated, i.e., one for the part that is covered by the water reflector and another for the part that is above the water level. This modelling approach was demonstrated to be faithful enough, at least for the calculation of the static neutron flux distribution [32].

The movement of the fuel rods imposed in the COLIBRI experiments is modelled with the  $\epsilon/d$  method [33-34]. Accordingly, the noise source is described using two Dirac-like perturbations localized at the west and east boundaries of the region of the vibrating fuel rods, see Figure 27. The amplitudes of the perturbations are defined as the differences between the macroscopic cross sections of the vibrating and the neighbouring regions. A fine spatial discretization is used for the region where the perturbation is located, so that the effect of the small displacement of the fuel rods can be accurately reproduced. The same modelling strategy was used for the experiments of both the first and the second campaign. The models of the two campaigns differ only in the selected computational grid.

No modelling of detectors is included. Instead, the calculated thermal neutron noise at the center of the active region of each detector is used. The detector arrangements in the two experimental campaigns are illustrated in Figures 41 and 42.

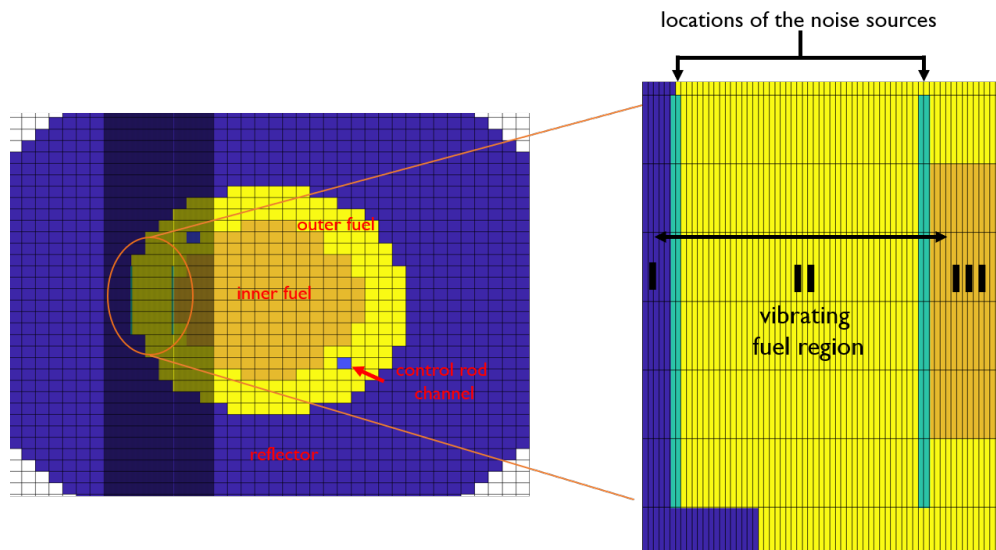


**Figure 43: Radial cross-section of the reactor model (left) and neutron noise sources (right).**

### 5.2.2 Model verification

As a verification exercise, the point-kinetic zero-power transfer function of CROCUS is computed with CORE SIM+ at various frequencies and compared with its analytical values, see Figure 44. CORE SIM+ estimates the transfer function very accurately in the frequency range ( $10^{-4}$  –  $1000$  Hz), which encloses the frequency range of the noise experiments ( $0.1$  Hz –  $2$  Hz). The code can reproduce the large variation of the amplitude and phase over the frequency range. The maximum deviation is below 1.5% for the amplitude and  $\sim 2.5$  degrees for the phase.

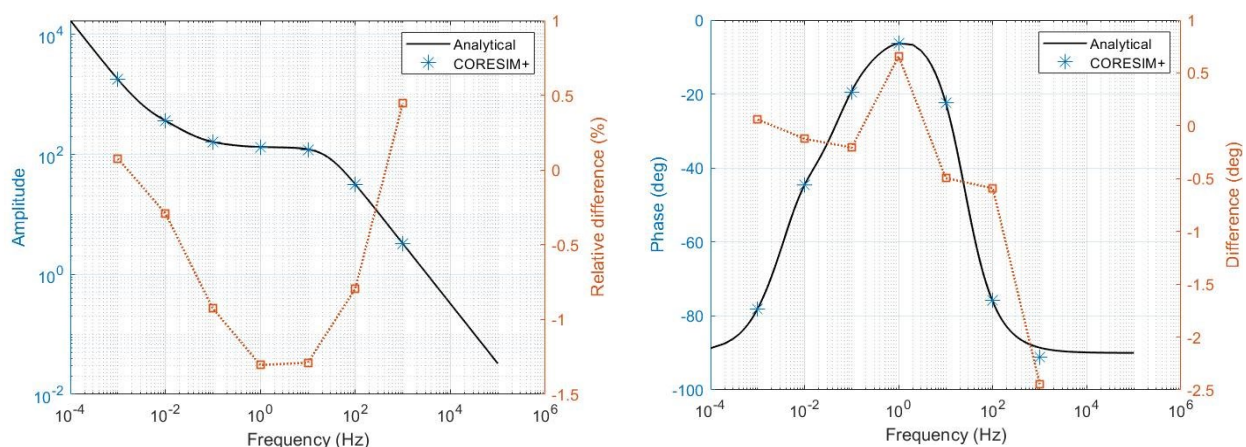


**Figure 44: CROCUS zero-power reactor transfer function; comparison between CORE SIM+ and the expected analytical solution.**

### 5.3 FEMFFUSION and PARCS modelling

Time-domain neutron noise simulations using the coarse-mesh, diffusion-based codes FEMFFUSION and PARCS were performed by UPV. The main methods to simulate mechanical vibrations of the fuel assemblies are described in [5].

UPV modelled the CROCUS reactor using a two-dimensional mesh for the time-dependent simulations with FEMFFUSION and PARCS. Cross sections for the diffusion approximation and kinetic data can be found in [7]. Two grids were proposed:

- A uniform refined mesh with a  $44 \times 44$  cells, each cell of  $2.917 \text{ cm} \times 2.917 \text{ cm}$ . The uniform mesh is shown in Figure 45.
- A locally refined mesh around the region where the fuel rods vibrate, the refining being in the direction of the movement of the fuel rods. Then the original cell is composed of  $96 \times 44$  cells. The locally refined mesh is displayed in Figure 46.

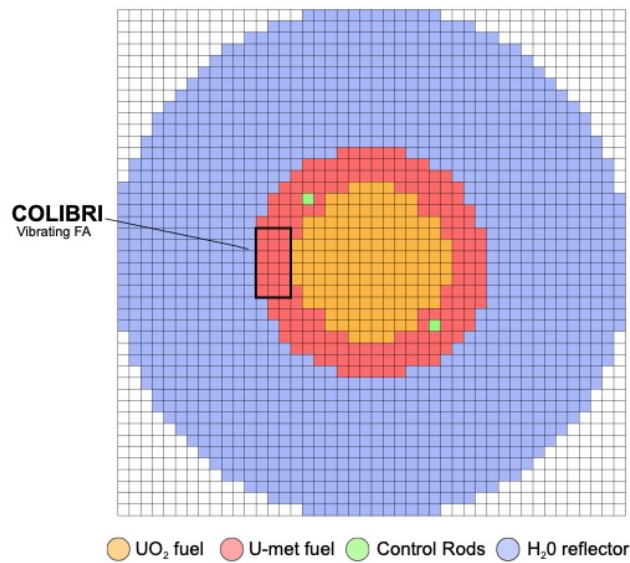


Figure 45: Uniform refined mesh for the CROCUS reactor.

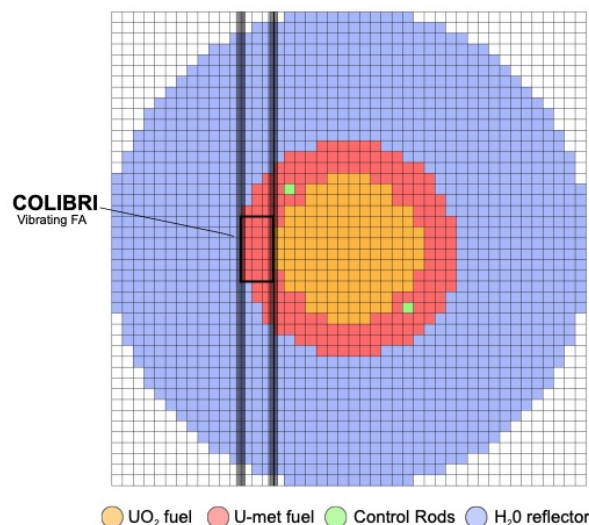


Figure 46: Locally refined mesh around the vibrating cluster of fuel rods, for the CROCUS reactor.

## 5.4 TRIPOLI-4® modelling

The TRIPOLI-4® noise calculations for the first and second COLIBRI experimental campaigns have been run by using the methods and the strategy thoroughly described in [6]. In the following, we will recall the main simulation results.

### 5.4.1 Model description and simulation parameters

The CROCUS model for TRIPOLI-4® is a fully detailed 3D geometry including the explicit structures for the detectors and continuous-energy material compositions. A radial cut is illustrated in Figure 48, where we compare the reactor specifications for the first and second experimental campaign to the corresponding Monte Carlo models. The only approximation introduced in the TRIPOLI-4® description is that the 18 fuel pins for the vibrating region have been transformed into “square” cylinders, in order to simplify the calculations of the noise source terms (see the considerations discussed in [6]). This simplification is however unnecessary and might be removed if needed, by allowing for the complex shapes of the overlapping disks. The whole set of detectors is taken into account and the control rod is also modelled.

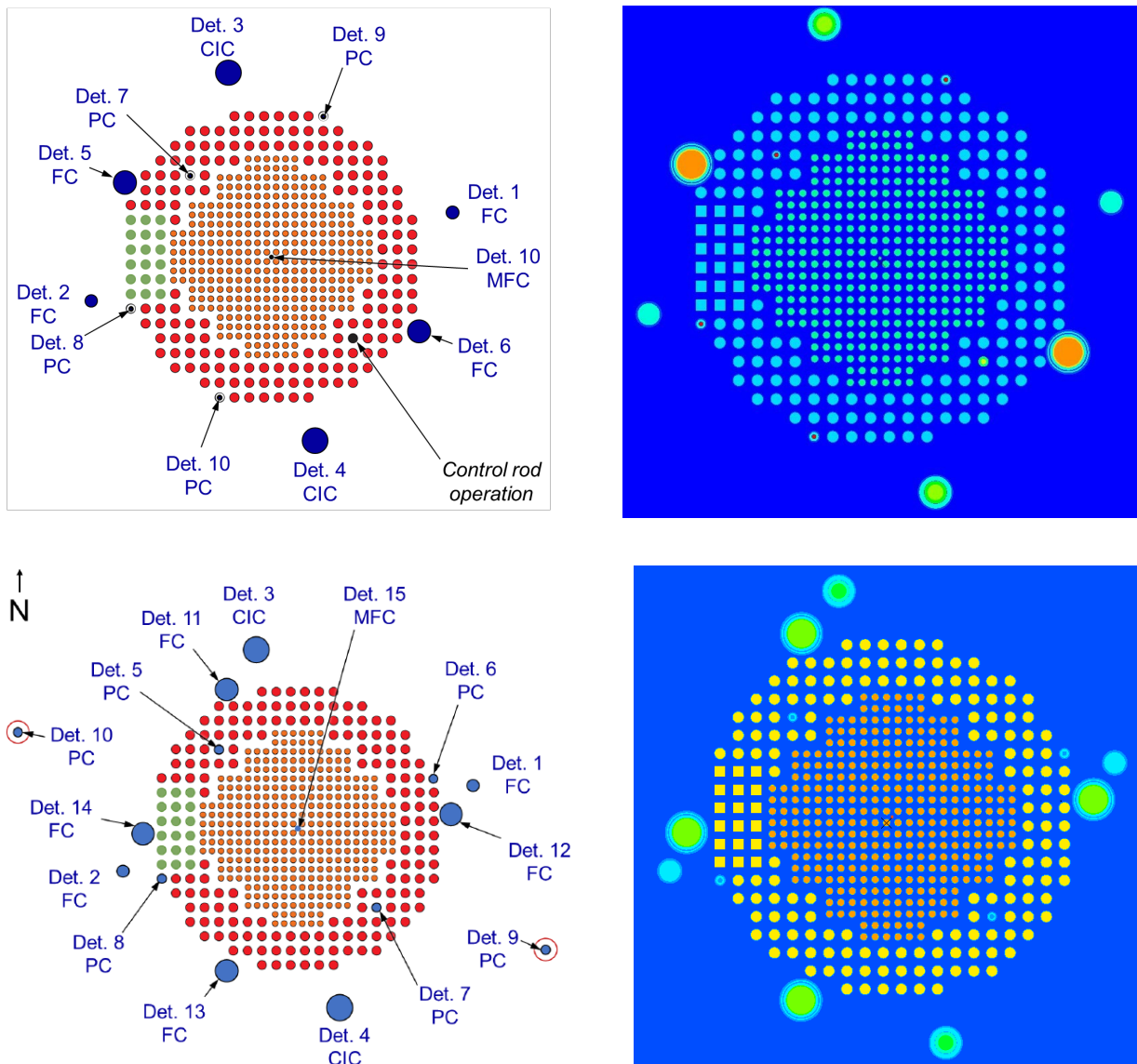


**Figure 47:** Radial cut of the reactor specifications (left) and of the corresponding TRIPOLI-4® model (right) for the COLIBRI experimental campaigns in CROCUS. Top: configuration in the first experimental campaign; bottom: configuration in the second experimental campaign.



The chosen nuclear data library for all the calculations presented in the following is JEFF3.1.1. The water level is adjusted to the one given in the experimental specifications: due to the uncertainties in the nuclear data library and in the technological specifications, a residual bias is expected concerning the criticality at the water height that is supposed to make the reactor critical. In other words, the effective multiplication factor  $k_{eff}$  will not be 1 at the critical water height. This discrepancy, which is of course not specific to noise calculations but affects more generally eigenvalue problems, is implicitly taken into account by the  $1/k_{eff}$  factor that is commonly used in the definition of the noise equations (and the noise source). Although the model is not precisely critical, the system is made artificially critical by rescaling the fission neutron multiplicity with the value of  $k_{eff}$  computed by the code. Observe that the water level for the two configurations is not the same, since the reactivity has been adjusted to compensate the replacement of the control rod with a detector in the second campaign [8].

Several sets of simulations have been carried out. In the following, we focus on a set of results pertaining to:

- experiments 12 and 13 of the first campaign, which correspond to a vibration of amplitude 2 mm and frequency 0.1 Hz and a vibration of amplitude 2 mm and frequency 1.0 Hz, respectively; and
- experiments 7 and 8 of the second campaign, which correspond to a vibration of amplitude 1.5 mm and frequency 0.1 Hz and a vibration of amplitude 1.5 mm and frequency 0.97 Hz, respectively.

As mentioned in [6], the noise source is modelled exactly, i.e., by representing the full Fourier transform of the spatial displacements of the fuel pins into the moderator, without resorting to the  $\varepsilon/d$  approximation. No attempt has been made to take in account the fact that the supposedly monochromatic vibration at frequency  $\omega_0$  is actually not a perfect “sine function”, because of inertial effects in the COLIBRI vibrating mechanism. We will therefore assume that the vibration is described by a sine function with a single frequency  $\omega_0$ , i.e., 0.1, 0.97 or 1 Hz in our case, depending on the chosen configuration. In view of the considerations discussed in [6], however, we have explicitly simulated not only the noise source component at the fundamental frequency  $\omega_0$ , but also the second higher harmonic at  $2\omega_0$ .

For the noise calculations described in the following, we have used the simulation parameters reported in Table 14.

**Table 14: Parameters used for TRIPOLI-4® simulations**

<b>Case:</b>	<b>1<sup>st</sup> campaign 2 mm 0.1 Hz</b>	<b>1<sup>st</sup> campaign 2 mm 1 Hz</b>	<b>2<sup>nd</sup> campaign 1.5 mm 0.1 Hz</b>	<b>2<sup>nd</sup> campaign 1.5 mm 0.97 Hz</b>
Criticality: inactive cycles	100	100	100	100
Criticality: decorrelation cycles	3	3	3	3
Criticality: number of particles/cycles	30 000	30 000	30 000	30 000
Noise: number of replicas	100 000	100 000	100 000	100 000

Concerning the results, the noise is tallied by TRIPOLI-4® in the form of real and imaginary parts separately, as detailed in [6]. For each component, the code yields the average value and the error bar, similarly as for regular Monte Carlo tally. This is justified by the real and imaginary parts of the noise being estimated using independent replicas. Based on these values, the absolute value and the phase are then reconstructed, but the error bar is not given, since the error propagation is not trivial (real and imaginary parts are strongly correlated and enter the formulas for the absolute value

and the phase in a nonlinear manner). Once the neutron noise has been computed, APSDs and CPSDs are estimated according to the procedure discussed in section 2.

The noise field is tallied over a 2D spatial mesh with 0.25 cm x 0.25 cm cells covering the entire geometrical model, and two energy groups: thermal for energies up to 0.625 eV, and fast above this threshold. The noise is also estimated in the volumes corresponding to the detectors of the CROCUS model, with the aim of having the APSD and CPSD values to be compared with experimental results.

#### 5.4.2 Criticality calculations: the fundamental flux

The criticality calculations do not depend on the noise source (i.e., the frequency and amplitude of the mechanical vibration), although for practical reasons the power iteration required to sample the critical eigen-mode is re-run for each of the four chosen noise experiments. This is mandatory in order to sample the noise source (which depends on the critical eigen-mode) without any discretization bias. The resulting spatial shape of the fundamental mode is shown in Figure 48, for the purpose of illustration. Observe that the fast flux is rather insensitive to the presence of the fuel pins, whereas the thermal flux exhibits strong local gradients across the pins and at the discontinuities corresponding to the boundaries with the oxide fuel and with the reflector.

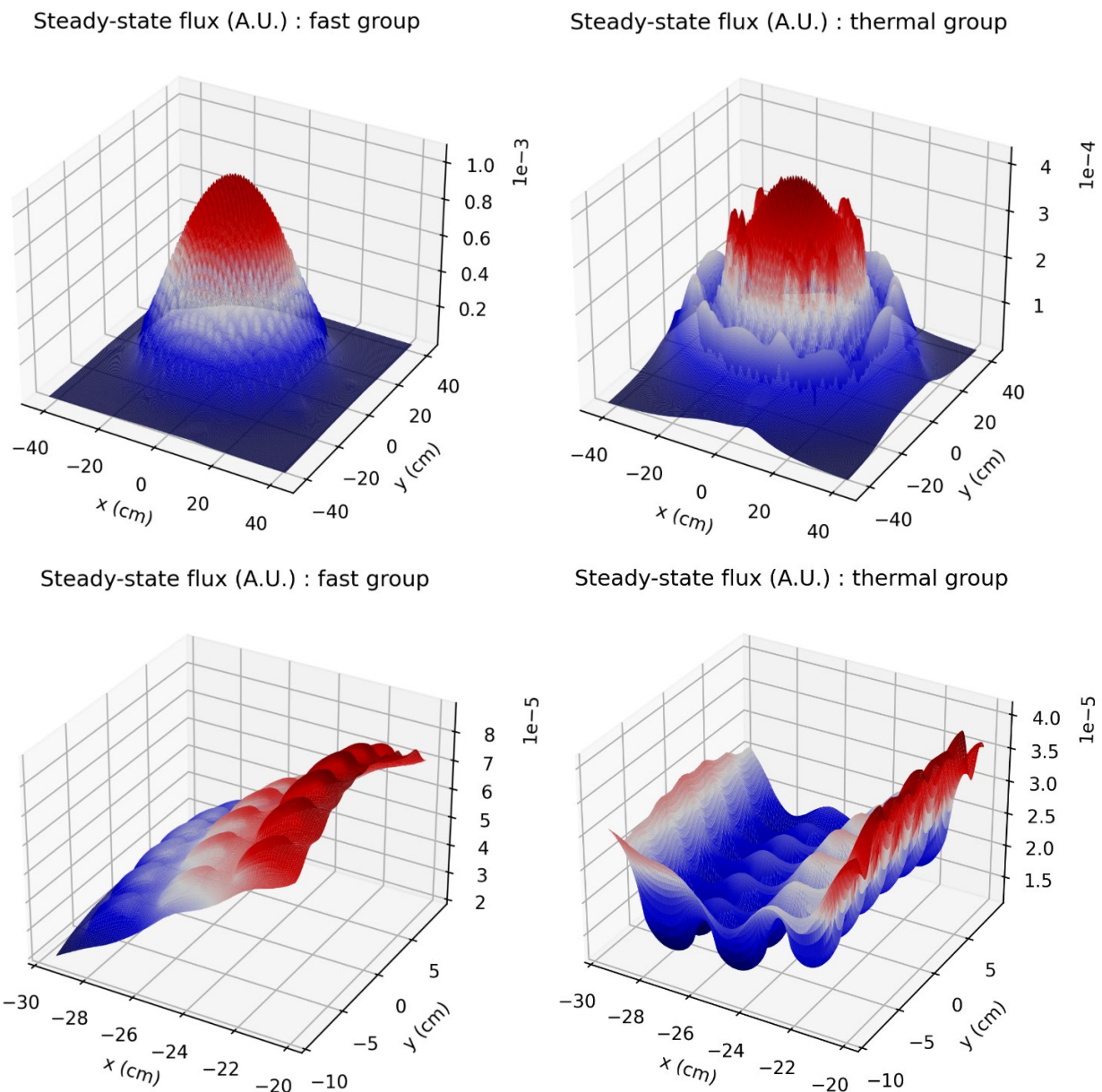


**Figure 48:** The critical neutron flux for the fast (left) and thermal (right) energy group, in arbitrary units. Top: overall spatial distribution. Bottom: zoom over the region of the 18 vibrating fuel rods.



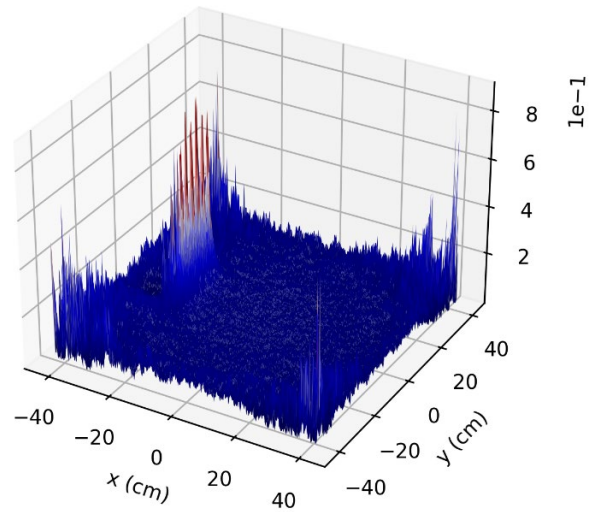
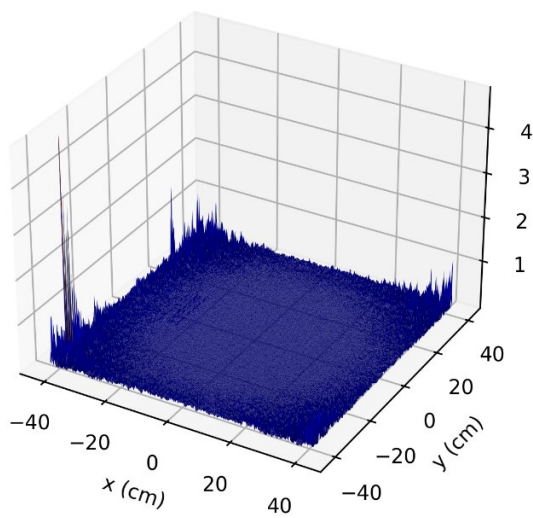
### 5.4.3 Noise calculations: the first harmonic

We now illustrate the behaviour of the first harmonic component of the noise: the simulation findings are shown in Figure 49 for the amplitude and in Figure 50 for the phase. For the sake of conciseness, we only display the results for the second campaign (those of the first campaign have very similar trends). The results for the noise amplitude are squared and normalized to the square of the fundamental mode (energy group by energy group), which corresponds to the definition of the APSD function.

The amplitude in Figure 49 shows that the fast component of the noise closely follows the profile of the fast component of the static flux (their ratio being constant), whereas a non-trivial spatial shape of the thermal component appears close to the vibrating region. Far from the vibrating rods, the ratio between the noise amplitude and the static flux is flat also for the thermal group. Despite some systematic differences, the behaviour of the noise is globally similar for the 0.1 and 0.97 Hz cases, and the main spatial trends are close to each other.

Modulus (A.U.) : fast group ( Normalized )

Modulus (A.U.) : thermal group ( Normalized )



Modulus (A.U.) : fast group ( Normalized )

Modulus (A.U.) : thermal group ( Normalized )

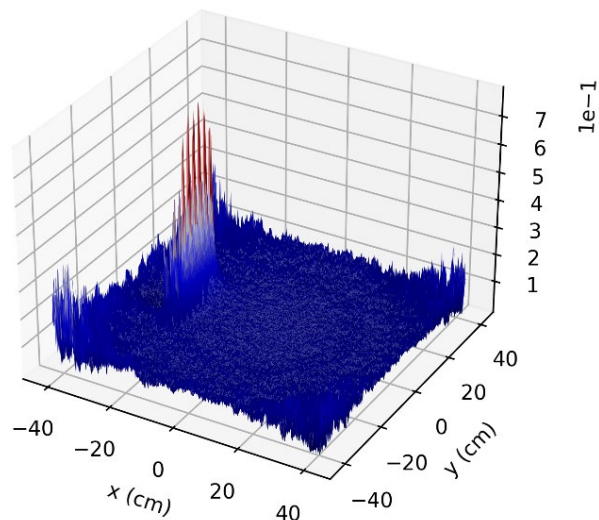
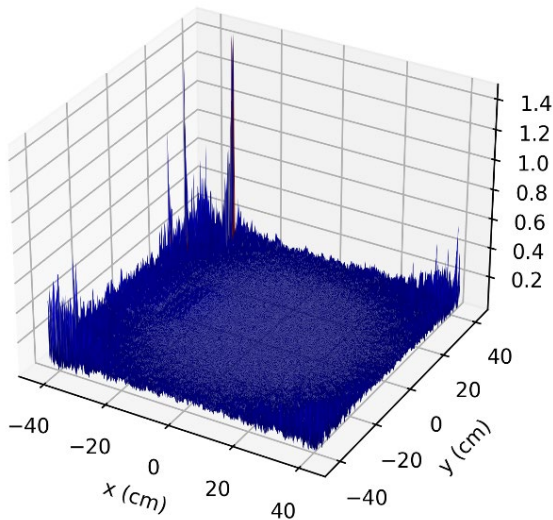


**Figure 49: The first harmonic component of the (normalised) absolute value of the neutron noise field for the fast (left) and thermal (right) energy group. Top: vibration at amplitude 1.5 mm and frequency 0.1 Hz (2nd campaign, experiment 7). Bottom: vibration at amplitude 1.5 mm and frequency 0.97 Hz (2nd campaign, experiment 8).**

The spatial behaviour of the phase for the first noise harmonic is displayed in Figure 50. For the fast component, the phase is flat; for the thermal component, the phase is overall flat, apart from an abrupt deviation that appears in the vibrating region. The observed trends are very similar for both 0.1 and 0.97 Hz.

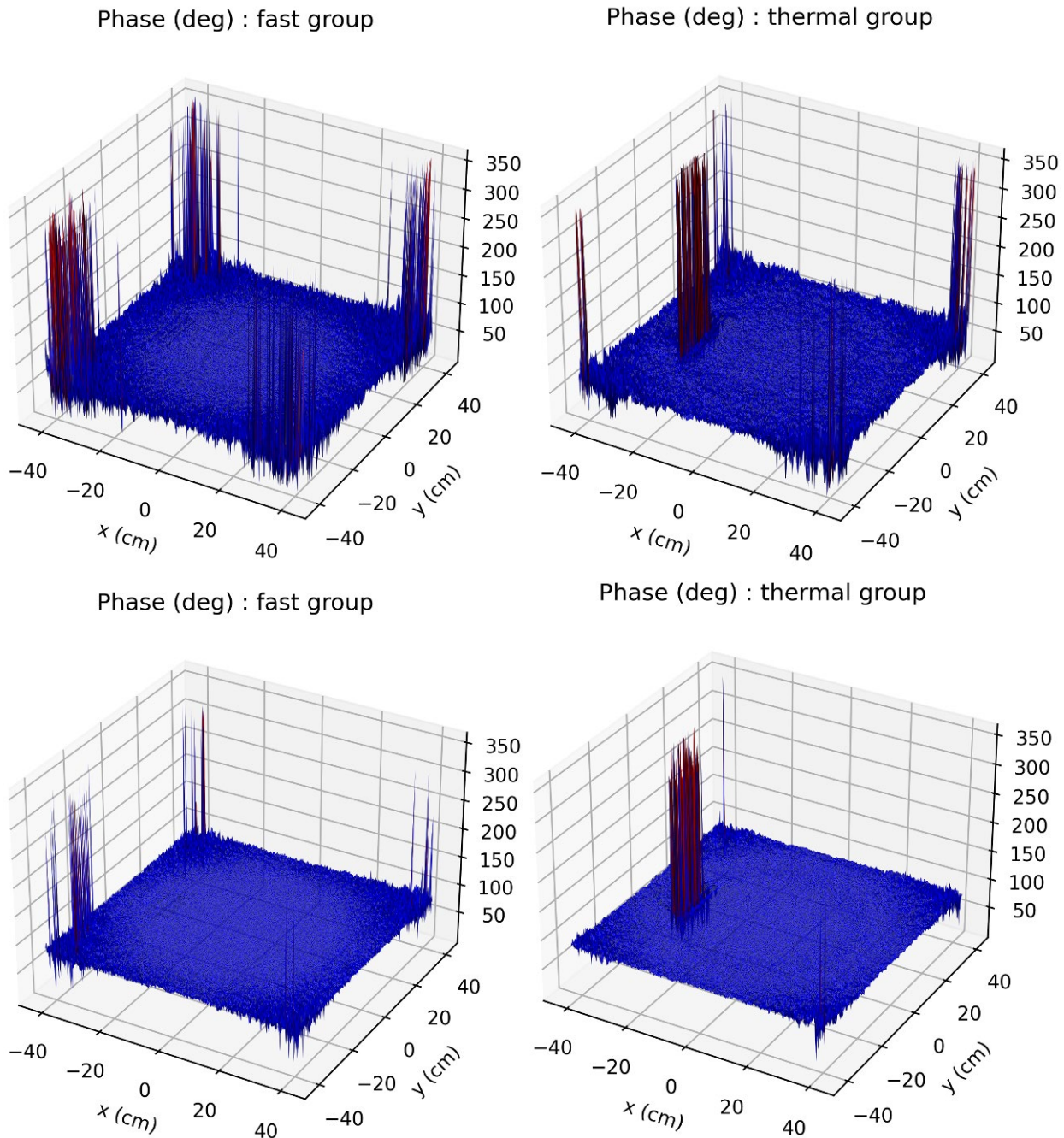


**Figure 50: The first harmonic component of the phase of the neutron noise field for the fast (left) and thermal (right) energy group. Top: vibration at amplitude 1.5 mm and frequency 0.1 Hz (2nd campaign, experiment 7). Bottom: vibration at amplitude 1.5 mm and frequency 0.97 Hz (2nd campaign, experiment 8).**

#### 5.4.4 Noise calculations: the second harmonic

We now illustrate the behaviour of the second harmonic component of the noise: the simulation findings are shown in Figure 51 for the amplitude and in Figure 52 for the phase. Similarly as for the case of the first harmonic, for the sake of conciseness, we only provide the results for the second

campaign (those of the first campaign have very similar trends). In order to make the interpretation easier, we show a cut at the center of the core, with both the first and second harmonic.

The amplitudes in Figure 51 show that the linearized noise solver implemented in TRIPOLI-4® systematically predicts that the second harmonic component should have an amplitude everywhere significantly larger than the first harmonic. Despite some systematic differences, the behaviour of the noise is globally similar for the 0.1 and 0.97 Hz cases, and the main spatial trends are close to each other. This surprising behaviour, which contradicts the experimental findings of the COLIBRI measurements (where the first harmonic has been found to be dominant over the second harmonic), is actually an artefact of the “orthodox linearization” [35]. No spatial effect is detected on the phase of the second harmonic, as shown in Figure 52.

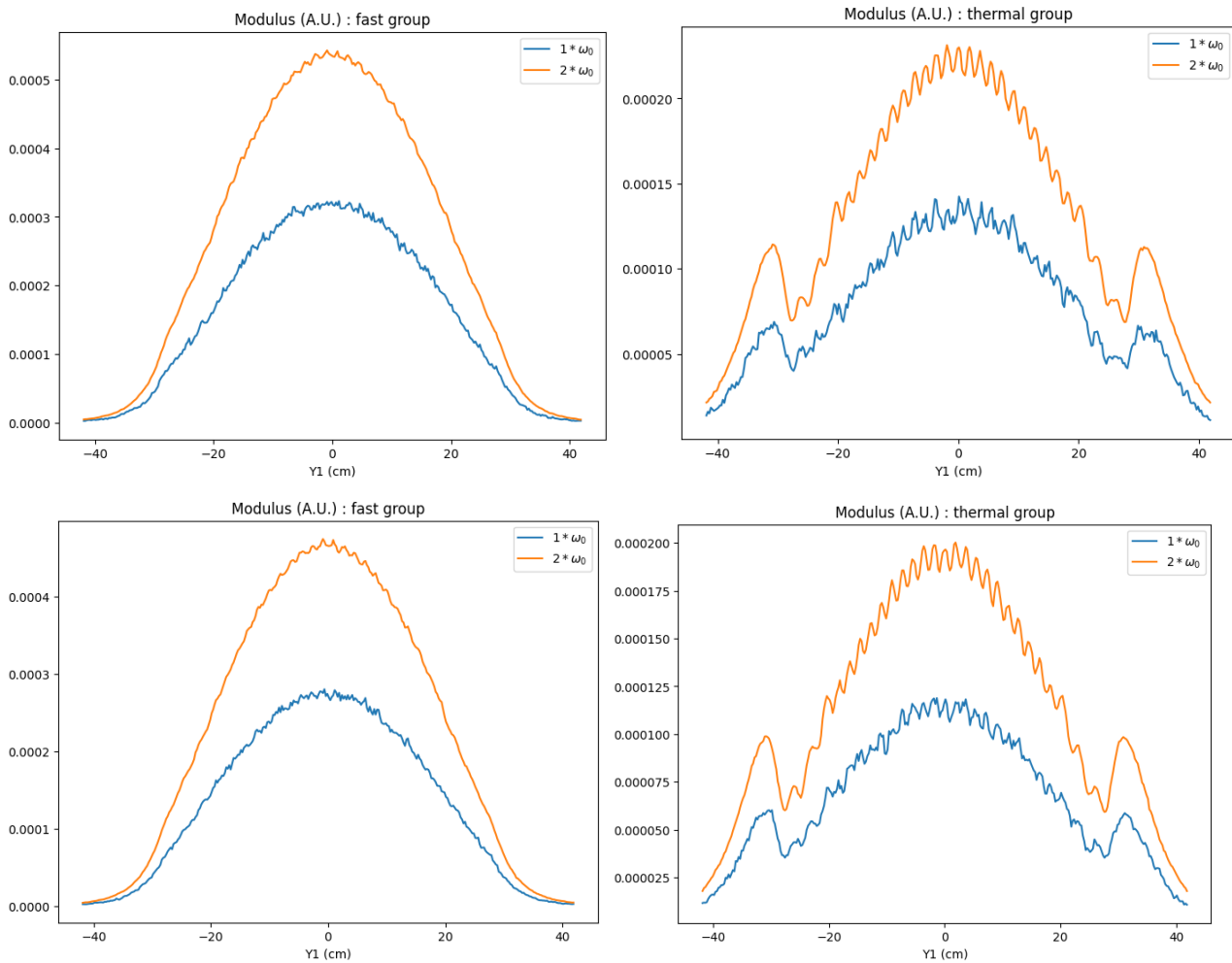


**Figure 51: Comparison between the second harmonic component of the absolute value of the neutron noise field (cut at the center of the core) for the fast (left) and thermal (right) energy group. Top: vibration at amplitude 1.5 mm and frequency 0.1 Hz (2nd campaign, experiment 7). Bottom: vibration at amplitude 1.5 mm and frequency 0.97 Hz (2nd campaign, experiment 8).**

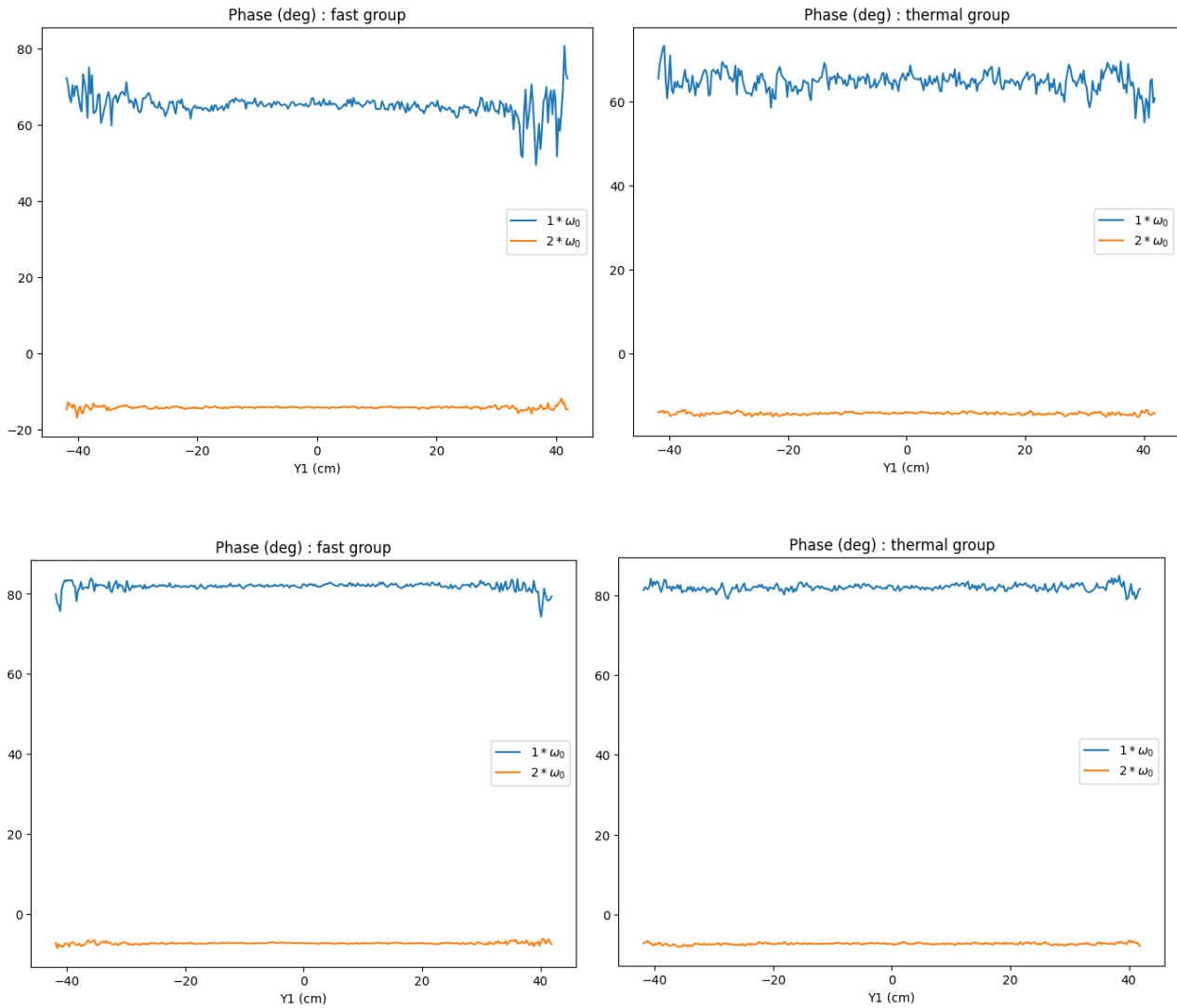


**Figure 52: Comparison between the second harmonic component of the phase of the neutron noise field (cut at the center of the core) for the fast (left) and thermal (right) energy group. Top: vibration at amplitude 1.5 mm and frequency 0.1 Hz (2nd campaign, experiment 7). Bottom: vibration at amplitude 1.5 mm and frequency 0.97 Hz (2nd campaign, experiment 8).**

## 5.5 APOLLO3® – IPK modelling

The APOLLO3® – IPK model has been used to simulate the experiments carried out in the first COLIBRI campaign. The analysis of experiments 12 and 13 is discussed and includes the comparison between calculations and measurements, the effect of higher frequencies on the calculated noise amplitude, and the difference between a realistic and a simplified modelling of the COLIBRI oscillations.

### 5.5.1 Comparison between simulations and measurements for experiments 12 and 13 in COLIBRI campaign 1

The comparisons of  $CPSD_{x,5}$  amplitudes estimated between the generic detector  $x$  and detector 5 (or equivalently  $CPSD_{5,x}$  amplitudes) in experiments 12 and 13 of the first COLIBRI campaign show an overall good agreement between computed and experimental values, see Figure 53a and Figure 53b, respectively. The model slightly underestimates the amplitude of the signals for experiment 12, possibly as a consequence of the high sensitivity of the reactor transfer function at low frequencies [36], showing that small deviations from the determined oscillation frequency  $\omega_c$  may induce larger variations in the intensity of the signal. The model computes higher responses as the distance from COLIBRI decreases, showing that the spatial dependence of the results is consistent to what is



expected from physics. In order to comment some experimental outcomes, we can say the following: detectors 3 and 10 are about the same distance from COLIBRI and one should expect to see almost the same response, as obtained by the simulation. However, this is not necessarily true for the measurements. Again, comparing detectors 3 and 4, one expects that the signal should be higher in detector 3 because of its proximity to the noise source, but also in this case the model and the experiment are in contradiction. Further investigations are ongoing. Again, it is worth making a comment on the reported uncertainties: the estimated error bar is of the order of  $10^{-6}$  for a relative measured reaction rate variation value of the order of  $10^{-5}$ . By the rule of thumb, since the CPSD is the product of two signals of the same order of magnitude, it follows that the amplitude of the single detector signal is around  $\sim 10^{-2}$  and its uncertainty  $\sim 10^{-3}$ . With these numbers in mind, one may question the capability of the detector to provide such accuracy with such a small measured value. Unfortunately, the datasheets of the installed detector are not available. Finally, when looking at the signal phases relative to the one of the detector pair 6-5, see Figure 54, by supposing that this pair is in phase with COLIBRI, we expect to see an increasing delay as the distance from the reference point. The only exception is represented by detector 8, the closest to the COLIBRI boundary, which may suffer from some spectral effects [37]. For the others, the expected behavior is captured by the simulations, while the experiments show some unexpected deviations, currently under investigation. Nevertheless, we can say that the IPK model provides results in an acceptable agreement with respect to the measurements, confirming thus the good capability of the code.

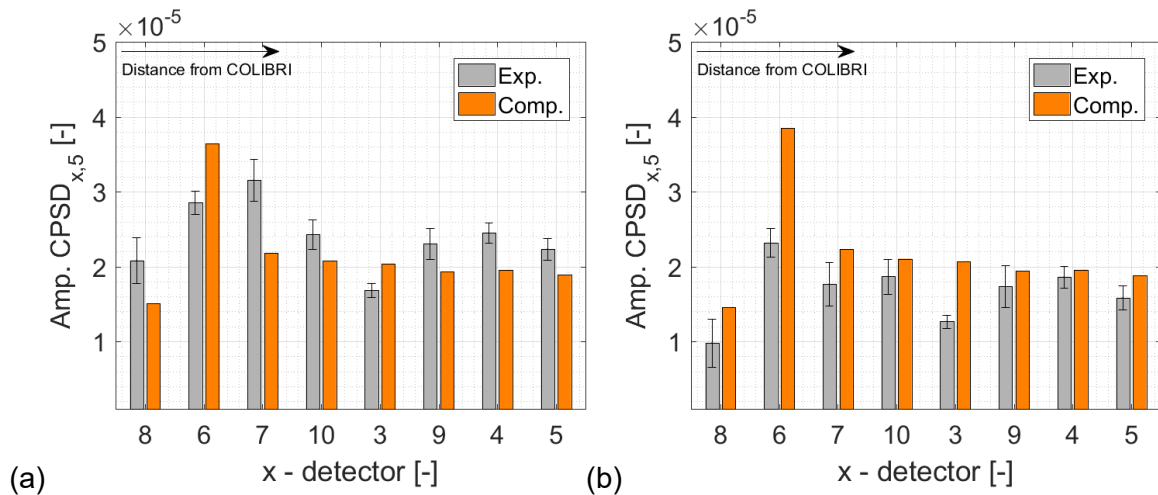


**Figure 53 :  $CPSD_{x,5}$  amplitudes for experiments 12 (a) and 13 (b).**

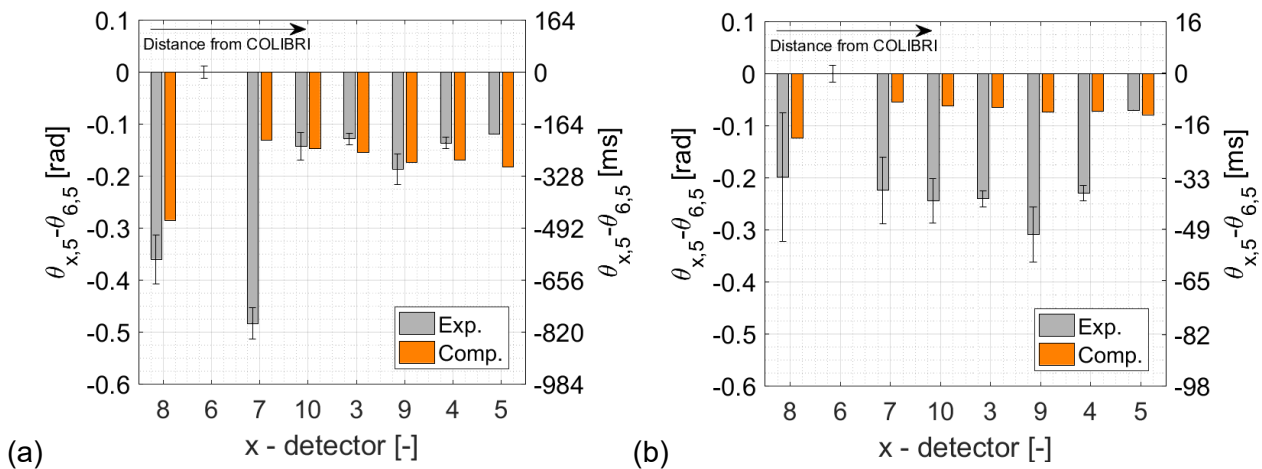


**Figure 54:  $CPSD_{x,5}$  relative phases for experiments 12 (a) and 13 (b).**

### 5.5.2 Effects of the higher frequency on noise amplitude

The amplitude of neutron noise depends on the oscillations of the delayed neutron source  $F_d \vec{C}$ , since, in the IPK model, this is the only term coupled in time by means of the quadrature formula used [20]. Therefore, it is worth investigating the effects of various frequencies of oscillations  $\omega_c$  on this operator. Consider that the period of oscillation is discretized in  $M$  time steps and suppose to sit on one of such given time instants, say  $t_k$ : if one computes explicitly the weights to each time interval  $t_{k'}$ , for a generic precursor family  $i$  with decay constant  $\lambda_i$ , it turns out that with  $1/\omega_c \ll \lambda_i$ , the weights tend to be uniform among all the time steps  $t_{k'}$  with  $k' = 1, \dots, M$ . On the other side, if  $1/\omega_c \gg \lambda_i$ , the weights decrease exponentially as the difference  $t_k - t_{k'}$  increases for  $k = 1, \dots, M$  with  $k \neq k'$ . In fact, looking at the values of the decay constant of delayed neutron precursors, if  $\lambda_i$  is larger than the period of oscillations ( $\lambda_i \gg 1/\omega_c$ ), the precursor concentrations in the system cannot reach their equilibrium during a cycle, which means that they do not decay sufficiently to induce a significant variation of the delayed source. Considering the extreme value for the frequency, i.e.  $\omega_c = \infty$ , one can imagine that the oscillation degenerates on an “intermediate stationary” state with negligible fluctuations of the delayed source. On the opposite, if  $\lambda_i \ll 1/\omega_c$ , during the oscillation period, the concentration for the  $i$ -th family may reach equilibrium, so it may decay significantly contributing to the fluctuations of the delayed source and therefore of the neutron flux. According to [34, 37], when using the classical point-kinetics transfer function, if the frequency of oscillation increases by one order of magnitude, the amplitude of the transfer function  $G(j\omega)$ , is reduced by a factor (almost) two, see Figure 55. In addition, it is clear that the largest amplitude reduction occurs when passing from 0.1 Hz to 2.0 Hz, while beyond this threshold the reactor transfer function starts to flatten. The IPK model captures the expected behavior of the transfer function. In fact, once a COLIBRI displacement is fixed and the simulations are performed considering various  $\omega_c$ , the amplitudes of  $CPSD_{x,5}$  decrease as the  $\omega_c$  increases up to an asymptotic value that corresponds to the frequency values where the transfer function starts to flatten. The computed results show that the amplitude decreases in the frequency range from 0.1 Hz to 2.0 Hz, according to what is expected from the theory, the CPSDs amplitudes are reduced by a factor  $\sim 1.76$  (on average), see Figure 56, while beyond the 2.0 Hz threshold, the reactor dynamics is less sensitive to the increase of  $\omega_c$ .

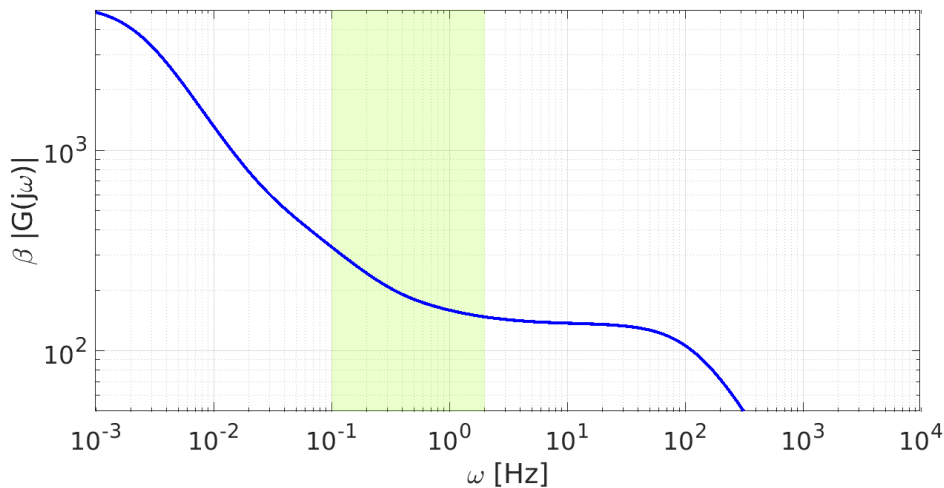


**Figure 55: Magnitude of critical CROCUS reactor transfer function, when using classical point-kinetics with parameters from [39]. The frequency range of interest (0.1 Hz – 2.0 Hz) is highlighted in green.**



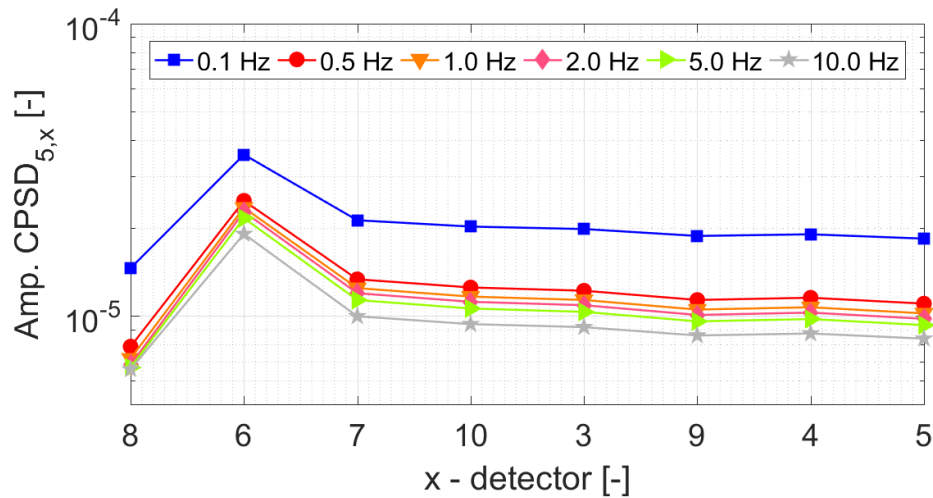


**Figure 56:**  $CPSD_{x,5}$  with various  $\omega_c$  and a fixed oscillation amplitude of 1.85 mm.

### 5.5.3 Analysis and reconstruction of COLIBRI movement

In the domain of numerical simulations, the quality of the output results highly depends on the quality of the input parameters, and in this case, it is the oscillation amplitude. The fuel pins oscillate thanks to a crankshaft mechanism that moves the top COLIBRI plate, connected to the bottom one by an aluminum rod. Since the two plates are not rigidly jointed in the translational movement, some de-synchronization due to inertia effects may arise between the two. Moreover, due to the mechanical limitations of the machine, the imposed movement is not an ideal sine curve, see Figure 57, but it shows a flattened region on the top and bottom boundaries. The spectral analysis of this “almost-sinusoidal” movement, see Figure 58, shows that higher frequencies, which can be either natural harmonics ( $\omega = n\omega_c, n \in \mathbb{N}^+$ ) or not, give indeed a contribution to the global movement. Therefore, it turns out that a simulation with an ideal sine curve may be a rude approximation causing some discrepancies.

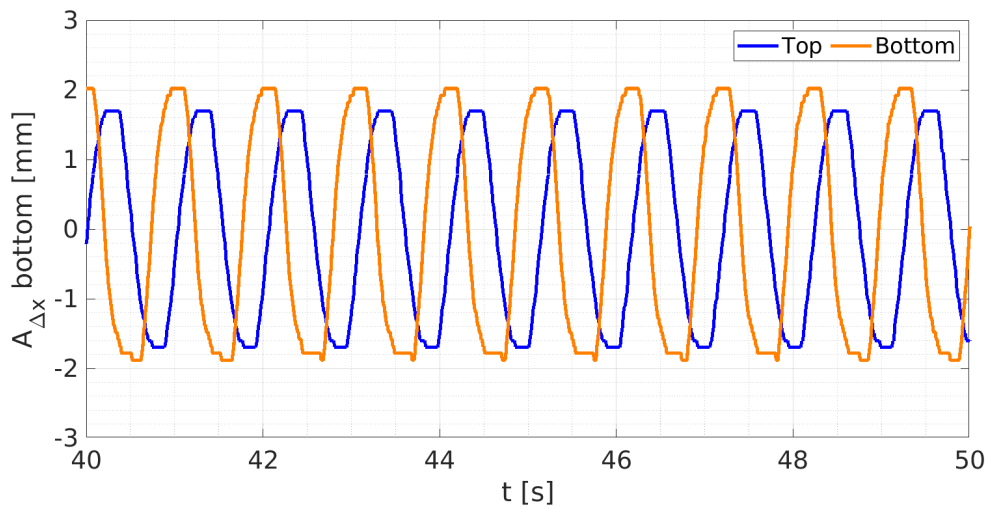


**Figure 57.** Time segments of raw top (blue) and bottom (orange) COLIBRI plates signals for experiment 13 in the first campaign ( $A = 2.0$  mm,  $\omega_c = 0.972$  Hz).

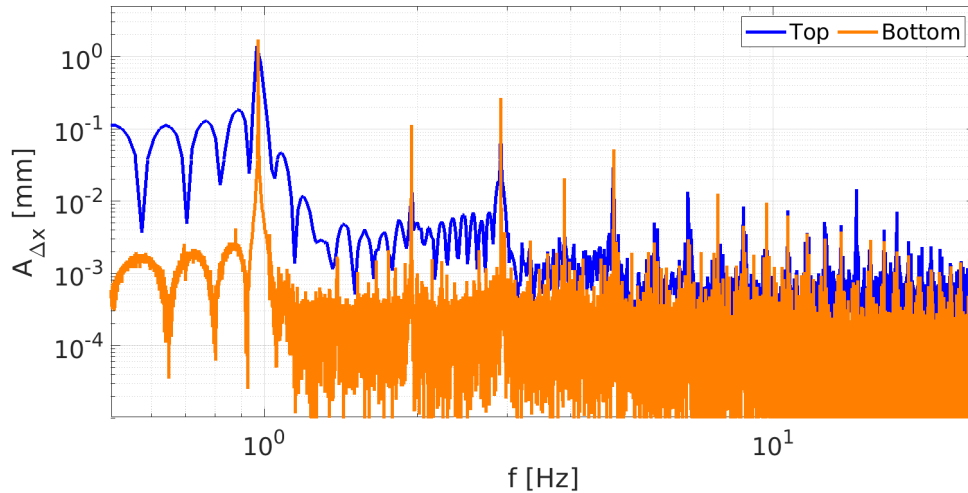


**Figure 58.** Frequency spectrum of top (blue) and bottom (orange) COLIBRI plates signals for experiment 13 in the first campaign ( $A = 2.0$  mm,  $\omega_c = 0.972$  Hz).

To improve the representativeness of the imposed shift, rather than the ideal/monochromatic approximation used so far, a reconstructed/polychromatic signal has been built. For conservative reasons, the bottom plate signal is chosen as reference and the new displacement has been obtained by superimposing the first  $N_k = 10$  harmonics of the signal Fourier spectrum as:

$$A_{\Delta x}(t) = \sum_{k=1}^{N_k} A_k \cdot \cos(2\pi k \omega_c) \quad (26)$$

where  $A_{\Delta x}(t)$  is the reconstructed shift of the pins and  $A_k$  is the amplitude corresponding to the  $k$ -th harmonic.

Then, as done for the simulation using the monochromatic displacement, a set of  $N$  discrete time equally spaced points are identified on the reconstructed signal, see Figure 59, and these are used as reference to compute the static flux distributions necessary to the IPK model.

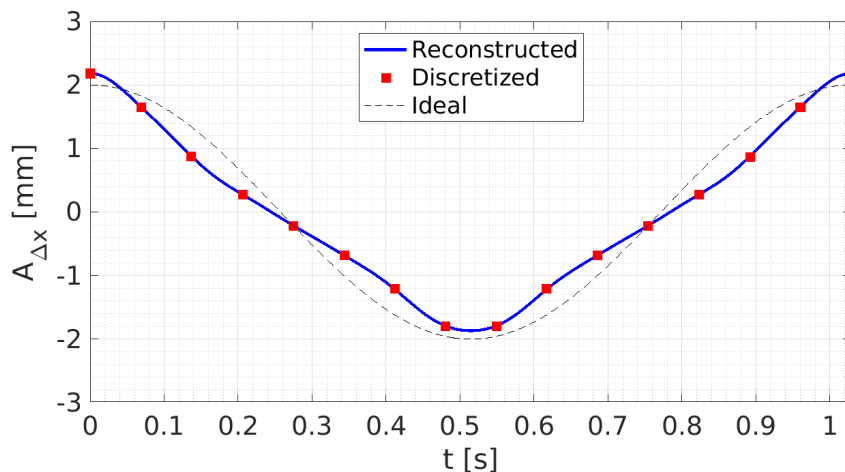


**Figure 59.** Bottom plate reconstructed (blue solid line) and monochromatic (dashed black line) signals for experiment 13 in COLIBRI campaign 1. Equally spaced discrete points are included (red squares).

Using the reconstructed COLIBRI signal, the computed results show a good agreement for the computed results of the CPSDs amplitudes and phases for experiment 12 and 13 of the 1<sup>st</sup> COLIBRI campaign, see Figures 60 and 61. From the experimental point of view, the outcomes of EPFL and CEA analyses give consistent results. On the computational side, instead, both simulations with the

ideal mechanical displacement, return slightly lower signal amplitude, possibly due to the sensitivity of the point-kinetics transfer function with  $\omega_c < 2\text{Hz}$  [36], see also section 5.5.2. The relative phase is within the error bars for experiment 12, with the exception of detector 7 showing an unexpected behavior currently under investigation. For experiment 13 with the higher frequency of oscillation, the relative phase measures few milliseconds, and the computed results fall mostly inside the error bars, or they are outside the uncertainty intervals of few milliseconds.

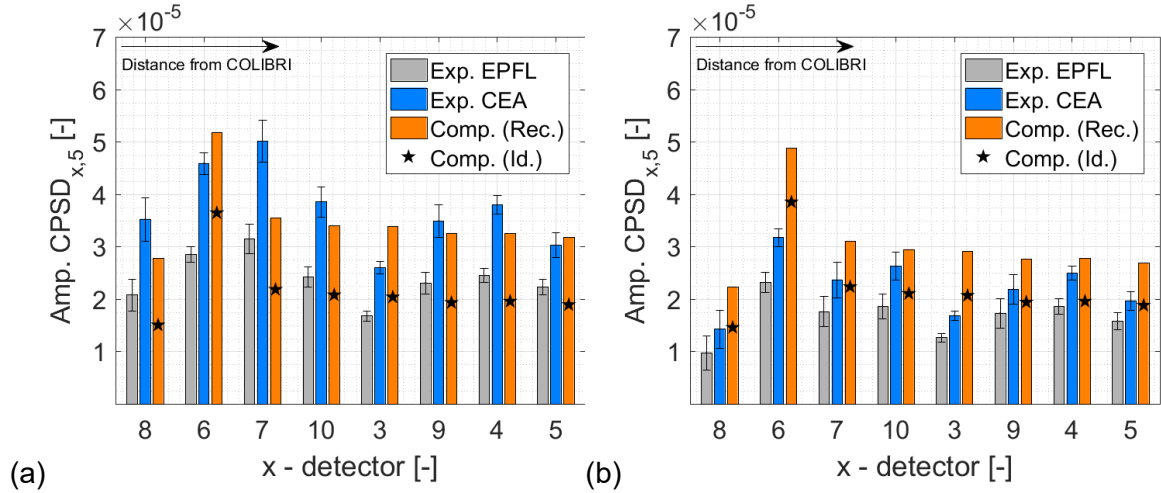


**Figure 60. Comparison of measures and computed CPD<sub>x,5</sub> amplitudes for experiment 12 (a) and 13 (b). Results obtained from reconstructed and ideal signal [23] are reported as orange bars and black stars, respectively.**

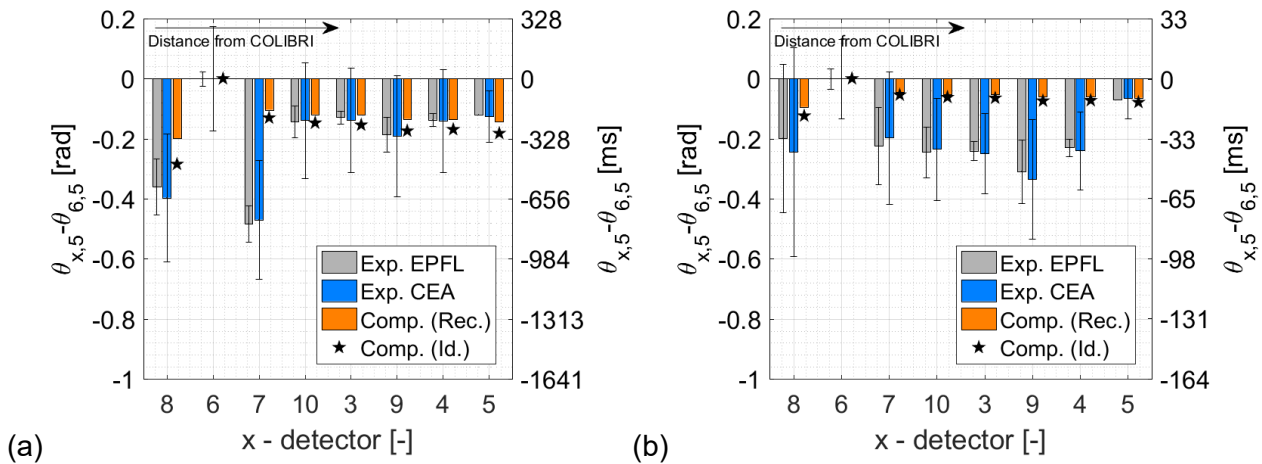


**Figure 61. Comparison of measures and computed relative (to pair 6&5) CPD<sub>x,5</sub> phases for experiment 12 (a) and 13 (b). Results obtained from reconstructed and ideal signal [23] are reported as orange bars and black stars, respectively.**

Concerning the simulation with the reconstructed COLIBRI signal, in principle, this should be a better representation of the actual shift. The absolute CPDs show higher detector responses with respect to the case with the monochromatic displacement [23] and the reason behind this difference may lay behind the fact that the shapes used in the IPK model are those obtained from the static stimulations and that, differently from the traditional approaches [22], these are not updated at the end of the iterations using a correction algorithm of the kind presented in [20]. Concerning the phases, no major differences are observed when using the monochromatic or reconstructed COLIBRI signal, as the shape update would rather modify its normalization, therefore the overall level of the signal, rather than the spatial distribution.

## 5.6 NOISE-SN modelling

The model for the NOISE-SN simulations of the COLIBRI experiments is very similar to the CORE SIM+ model described in section 5.2. The computational grid has minor differences. The same set of 2-energy group macroscopic cross sections associated with the 5 homogenized regions is used, see Figure 43. For the angular discretization, the order of discrete ordinates is chosen equal to 16. The model of the neutron noise source is again based on the  $\varepsilon/d$  method [33-34].

## 5.7 Comparison between simulations and measurements

COLIBRI experiments have been selected for the comparison between the results obtained from the different solvers and the measurements.

Experiments 12 and 13 are used from the first campaign. In these experiments, 18 fuel rods are oscillated via the COLIBRI device with an amplitude equal to  $\pm 2$  mm and frequency of 0.1 Hz (experiment 12) or 1.0 Hz (experiment 13).

Experiments 7 and 8 are considered in the second campaign, where the neutron noise is induced by oscillating 18 fuel rods with an amplitude equal to  $\pm 1.5$  mm and frequency of 0.1 Hz (experiment 7) or 0.97 Hz (experiment 8).

### 5.7.1 Results for the 1<sup>st</sup> campaign

In the first COLIBRI campaign, the comparison is based on the APSD amplitude for the generic detector  $i$  divided by the amplitude of the CPSD with respect to detector 5, and on the phase of the CPSD with respect to detector 5 (see section 2 for details about APSD and CPSD). In the plots, the detectors are ordered from the closest detector to the perturbation, to the farthest detector (see, e.g., Figure 41 for the position of the detectors).

The results are summarized in Figures 62 and 63 for experiment 12 and in Figures 64 and 65 for experiment 13. For a simpler visualization, Figures 62 and 64 include TRIPOLI4®, NOISE-SN, APOLLO3®-IPK, CORE SIM+ and FEMFFUSION, and Figures 63 and 65 include the diffusion-based solvers CORE SIM+, FEMFFUSION, PARCS and FEMFFUSION-SP3, which is a solver available in FEMFFUSION and based on the SP3 approximation [13].

The solvers predict a similar behaviour of the neutron noise, i.e., an increase of amplitude close to the oscillating fuel rods (from detector 8 to detector 6) and a decrease of amplitude in other locations that are farther from the perturbation (from detector 6 to detector 5). The neutron noise phase with respect to detector 5 is estimated to be very small. Similar trends are obtained from the measured neutron noise. The agreement in values between calculated and experimental noise amplitudes is not satisfactory in experiment 12, but relatively good in experiment 13, although large discrepancies are found for detector 8 (neutron transport and spectral effects may be challenging to simulate at such a location, very close to the perturbation) and detector 3 (whose measurements may have been affected by a bias).

The results calculated with diffusion-based solvers such as CORE SIM+, FEMFFUSION and PARCS are similar and agree with NOISE-SN (based on a discrete ordinates method) and with FEMFFUSION-SP3. These simulations make use of analogous reactor models (with 5 homogenized regions and 2-energy group macroscopic cross sections).

The model used for the APOLLO-3®-IPK simulations consists of a detailed description of the system in terms of geometry and cross sections (see section 5.5 and [23]) and leads to significant differences close to the perturbation (detectors 8 and 6) with respect to the other solvers.

The TRIPOLI-4® simulations provides a lower neutron noise for all the detectors in experiment 12 and for the detectors close to the oscillating fuel rods in experiment 13. The results obtained from the integral and thermal neutron flux are similar and differ at the position of detector 8 (which is nearest the noise source).

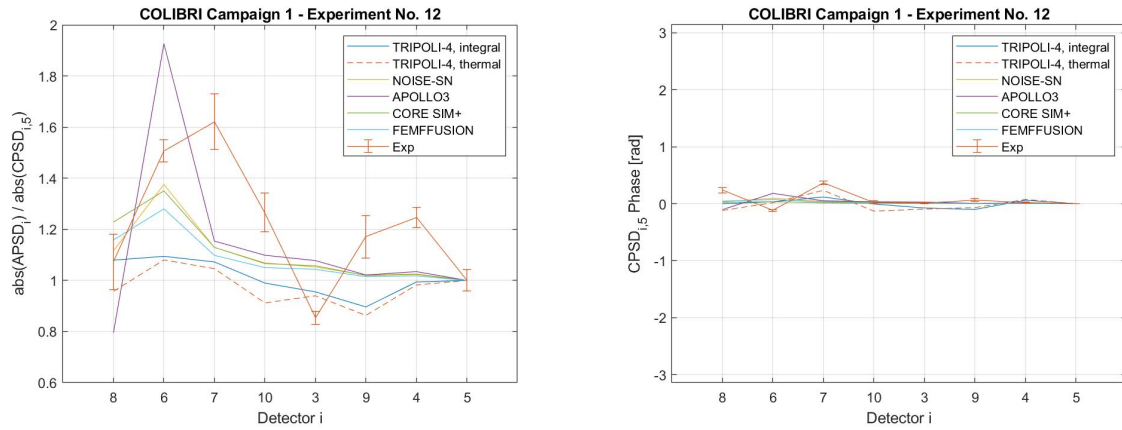


**Figure 62: Experiment 12 in the 1<sup>st</sup> COLIBRI campaign; relative noise amplitude (left) and noise phase (right). The detector 5 is used as reference.**

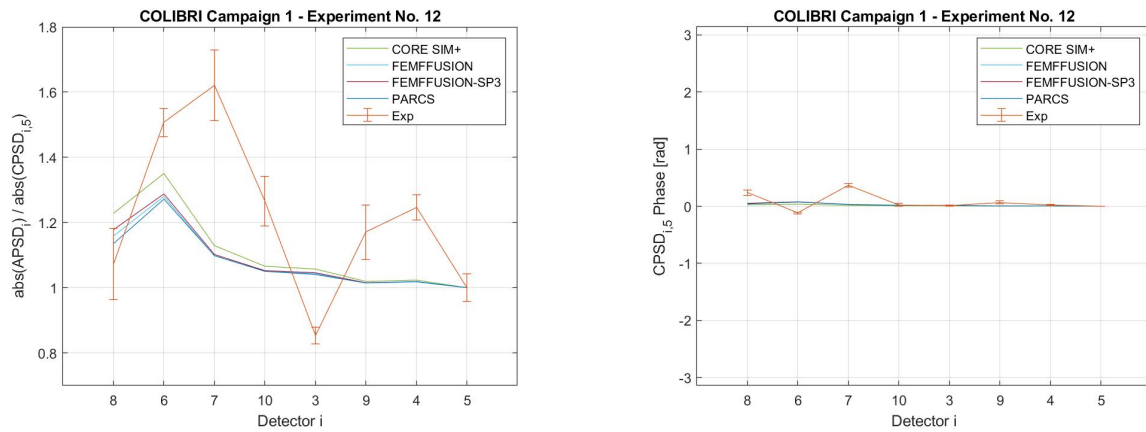


**Figure 63: Experiment 12 in the 1<sup>st</sup> COLIBRI campaign; relative noise amplitude (left) and noise phase (right) predicted by diffusion-based solvers and FEMFFUSION-SP3. The detector 5 is used as reference.**

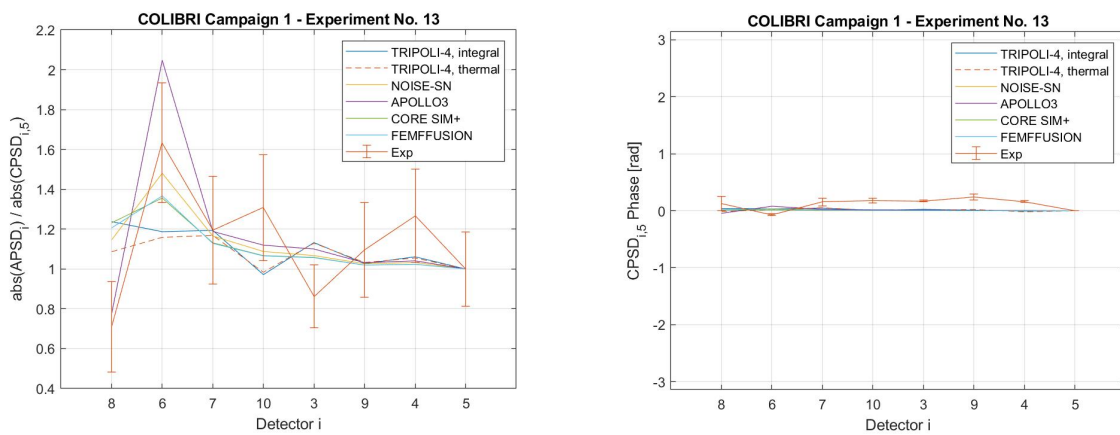


**Figure 64: Experiment 13 in the 1<sup>st</sup> COLIBRI campaign; relative noise amplitude (left) and noise phase (right). The detector 5 is used as reference.**

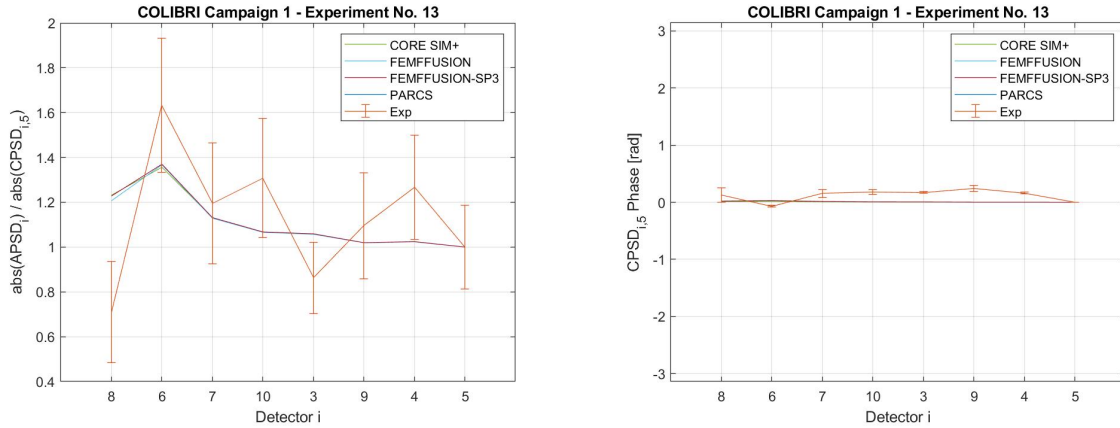


**Figure 65: Experiment 13 in the 1<sup>st</sup> COLIBRI campaign; relative noise amplitude (left) and noise phase (right) predicted by diffusion-based solvers and FEMFFUSION-SP3. The detector 5 is used as reference.**

### 5.7.2 Results for the 2<sup>nd</sup> campaign

In the second COLIBRI campaign, the comparison is based on the APSD amplitude for the generic detector  $i$  divided by the amplitude of the CPSD with respect to detector 12, and on the phase of the CPSD with respect to detector 12 (see section 2 for details about APSD and CPSD). In the plots, the detectors are ordered from the closest detector to the perturbation, to the farthest detector (see Figure 28 for the arrangement of the detectors in the reactor).

The results are summarized in Figures 66 for experiment 7 and in Figures 67 for experiment 8. Although discrepancies are found near the noise source, the simulations and the measurements provide a similar behaviour of the neutron noise.

The TRIPOLI-4® results show a decrease of neutron noise amplitude from detector 8 to detector 14, an increase from detector 14 to detector 2, and a decrease from detector 2 to detector 1, which are consistent with the measured noise amplitude. For the noise phase, a minimum value at the location of detector 14 is found in both TRIPOLI-4® calculations and measurements.

The diffusion-based solvers CORE SIM+ and FEMFFUSION calculate a peak of the noise amplitude at the location of detector 2 and a decrease of the noise level from detector 2 to detector 1, which resemble the experimental trend. Possible discrepancies close to the noise source (e.g., at the locations of detectors 8 and 14) may be due to limitations of diffusion theory to reproduce neutron transport effects.

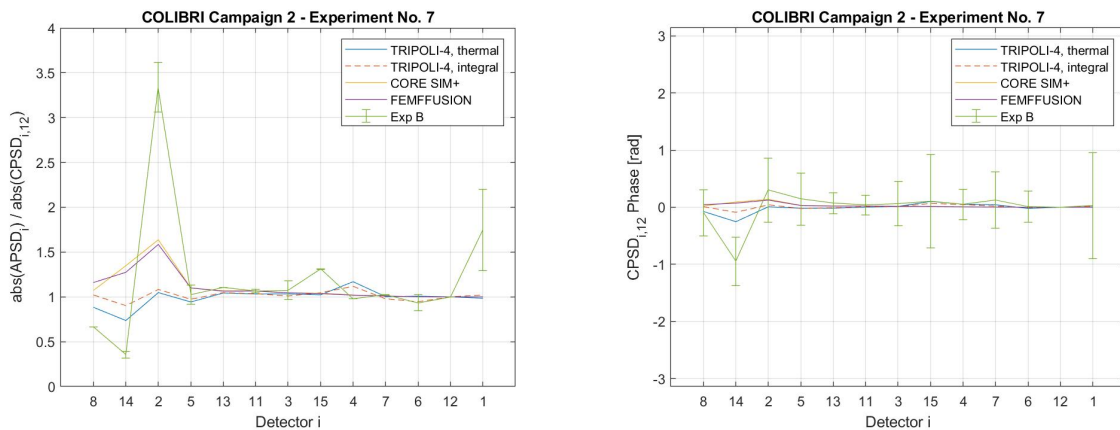


**Figure 66: Experiment 7 in the 2<sup>nd</sup> COLIBRI campaign; relative noise amplitude (left) and noise phase (right) predicted by diffusion-based solvers and FEMFFUSION-SP3. The detector 12 is used as reference.**



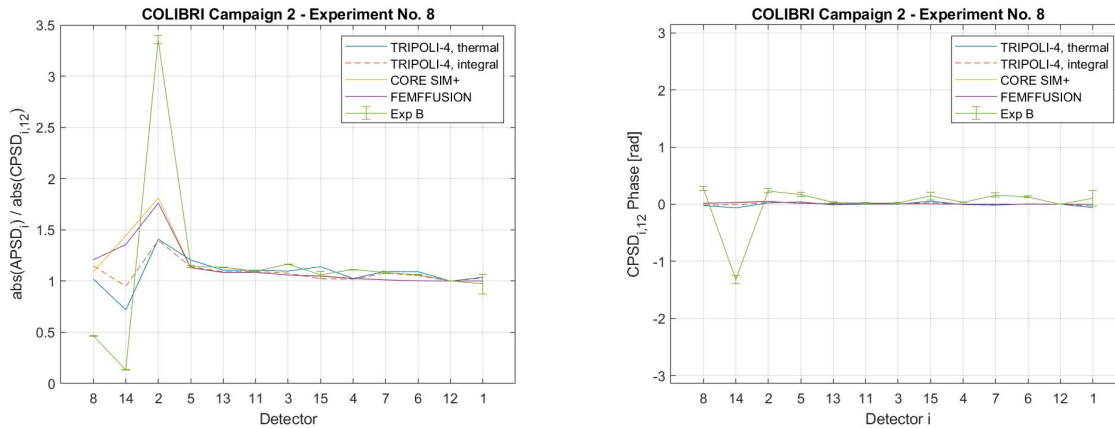


**Figure 67: Experiment 8 in the 2<sup>nd</sup> COLIBRI campaign; relative noise amplitude (left) and noise phase (right) predicted by diffusion-based solvers and FEMFFUSION-SP3. The detector 12 is used as reference.**

## 5.8 Uncertainty analysis for the CORE SIM+ simulations

The uncertainty analysis for the CORE SIM+ simulations of the COLIBRI experiments follows the identical procedure used for the CORE SIM+ simulations of the AKR-2 neutron noise experiments (see section 4.5). Since the model of CROCUS is relatively simpler than the model of AKR-2, the computational cost of the calculations is less. Therefore, the total number of code runs for uncertainty analysis has been increased to produce more precise tolerance intervals. Here, the uncertainty propagation is based on the 4<sup>th</sup> order Wilks' formula for two-sided limits [30]. In this case, if the 95%/95% criterion is taken, the number of code runs needs to be 260 in order to estimate the higher and the lower tolerance limit with the 4<sup>th</sup> largest and the 4<sup>th</sup> smallest values in the output samples, respectively.

### 5.8.1 Results for the 1<sup>st</sup> campaign

The analysis for the first COLIBRI campaign is focused on experiments 12 and 13 (see section 5.7). Based on the physical processes related to the vibration of fuel rods and the modelling of the reactor core used for the simulation, 776 parameters that may be influential on the neutron noise are selected, see Table 15. These parameters include the design and operating parameters, the noise source uncertainties associated with the amplitude, the frequency and the location of the vibration, and the nuclear data uncertainties. The uncertainties of the design and operating parameters are based on the actual manufacturing tolerances and the operational condition [39]. The uncertainties of the noise source are arbitrary following an expert's judgement. The 748 nuclear data correspond to the microscopic cross sections for  $^{235}\text{U}$ ,  $^{238}\text{U}$ ,  $^1\text{H}$  and  $^{16}\text{O}$ . The procedure for the generation of the uncertainties of the 2-energy group macroscopic nuclear data needed for the CORE SIM+ calculations is identical to the procedure used for the case of the AKR-2 reactor (see section 4.5).

Figure 68 shows the uncertainty of the neutron noise calculated with CORE SIM+ for experiment 12 and experiment 13. These uncertainties are small and as such cannot explain the discrepancies between computational and measured quantities of interest (compare Figure 68 to Figures 63 and 66).

**Table 15: Selected input and modelling parameters and their uncertainties for the simulations of the experiments in the 1<sup>st</sup> COLIBRI campaign**

No.	Parameter		Distribution	Unit	Nominal value	Standard deviation <sup>1,2</sup> (Lower/Upper limit)
1	Water level		Normal	cm	95.22	0.01
2	Initial pool temperature		Normal	°C	20.0	0.02
3	Initial pool density		-	g/cm <sup>3</sup>		<2>
4	Fuel density	UO <sub>2</sub>	Normal	g/cm <sup>3</sup>	10.556	0.034
5		U <sub>metal</sub>	Normal	g/cm <sup>3</sup>	18.677	0.044
6	Nuclide mass fraction	U-235 of UO <sub>2</sub>	Normal	-	1.806E-2	7E-6
7		U-238 of UO <sub>2</sub>	-	-		<6>
8		U-235 of U <sub>metal</sub>	Normal	-	9.470E-3	7E-6
9		U-238 of U <sub>metal</sub>	-	-		<8>
10	Active fuel length		Normal	cm	100.0	0.02
11	Relative axial location	Bottom of upper Grid	-	cm		<10>
12		Bottom of Upper Cd	-	cm		<10>
13		Top of Upper Cd	-	cm		<10>
14		Top of Upper Grid	-	cm		<10>
15		Fuel rod top spring	-	cm		<10>
16	Fuel diameter	Fuel rod outer surface of UO <sub>2</sub>	Normal	cm	0.526	8.5E-4
17		Cladding outer surface of UO <sub>2</sub>	Normal	cm	0.63	5E-3
18		Fuel rod outer surface of U <sub>metal</sub>	Normal	cm	0.85	1E-3
19		Cladding outer surface of U <sub>metal</sub>	Uniform	cm	0.965	0.965 / 0.97
20	Cladding thickness	UO <sub>2</sub>	Normal	cm	0.085	5E-3
21		U <sub>metal</sub>	Normal	cm	0.1	5E-3
22	Inner surface of cladding	UO <sub>2</sub>	-	cm		<17>, <20>
23		U <sub>metal</sub>	-	cm		<19>, <21>
24	Square pitch	UO <sub>2</sub>	Normal	cm	1.837	2E-4
25		U <sub>metal</sub>	Normal	cm	2.917	2E-4
26 ~773	Nuclear data uncertainties <sup>3</sup>					
774	Amplitude of fuel rod oscillation		Normal	cm	0.185 <sup>3</sup>	5%
					0.2 <sup>4</sup>	5%
775	Frequency of fuel rod oscillation		Normal	Hz	0.097 <sup>3</sup>	5%
					0.972 <sup>4</sup>	5%
776	Location of noise source		Uniform	Mesh	Ideal oscillating boundary	-1/+1 <sup>5</sup>

1: This column shows the value of lower and upper limit in the case of a parameter with uniform distribution.

2: This column shows the correlated parameters which are composing the corresponding parameter in the case of no specific distribution information (<k> represents the parameter consistently with the ID numbers given in the first column).

3: This information corresponds to the case of Experiment 12. Nuclear data uncertainties are treated in a distinct manner, as already explained in Section 4.5.

4: This information corresponds to the case of Experiment 13.

5: -1/+1 corresponds to -0.2/+0.2 cm.

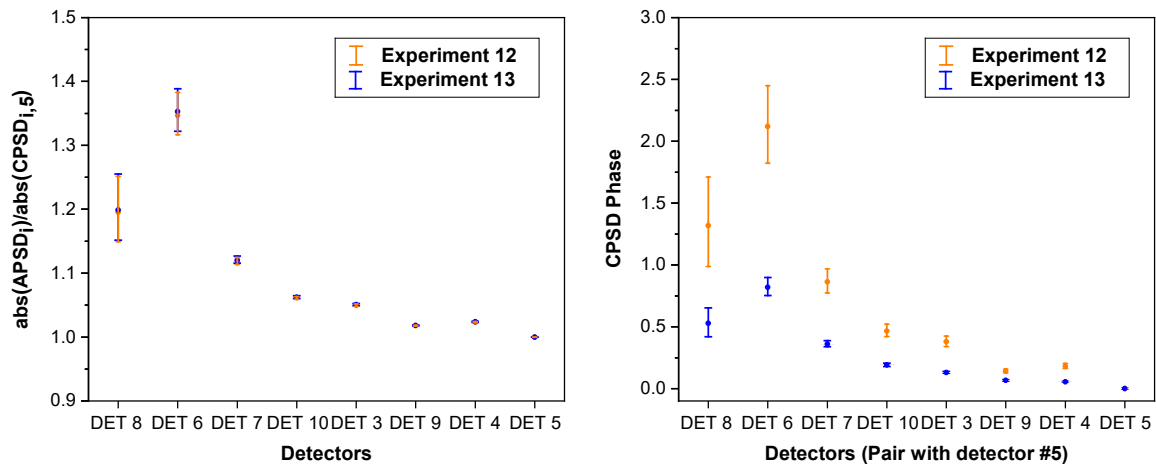


**Figure 68: Experiments 12 (red) and 13 (blue) in the first COLIBRI campaign; neutron noise relative amplitude (left) and phase (right).**

### 5.8.2 Results for the 2<sup>nd</sup> campaign

The uncertainty analysis for the simulations in the 2<sup>nd</sup> COLIBRI campaign follows the procedure used for the 1<sup>st</sup> COLIBRI campaign, and it is focused on experiment 7 and experiment 8 (see section 5.7). The input and modelling uncertainties are the same as the ones for the 1<sup>st</sup> COLIBRI campaign (see Table 15), except for the amplitude and frequency of fuel rod oscillations. For these two quantities, the uncertainty is reported in Table 16.

Figure 69 shows the uncertainties of the neutron noise calculated with CORE SIM+ for the experiments 7 and 8. These uncertainties are small and as such cannot explain the discrepancies between computational and measured quantities of interest (compare Figure 69 to Figures 66 and 67).

**Table 16: Parameters for the neutron noise source and their uncertainties for the simulations of the 2<sup>nd</sup> COLIBRI campaign**

No.	Parameter	Distribution	Unit	Nominal value	Standard deviation
774	Amplitude of fuel rod oscillation	Normal	cm	0.15	5%
775	Frequency of fuel rod oscillation	Normal	Hz	0.1 <sup>1</sup>	5%
				0.97 <sup>2</sup>	5%

1: Experiment 7.

2: Experiment 8.

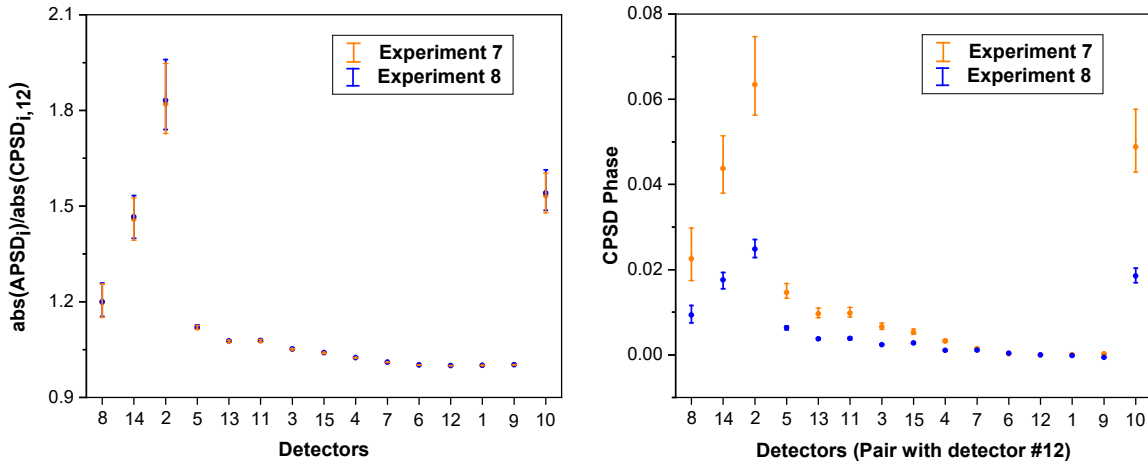


**Figure 69: Experiments 7 (red) and 8 (blue) in the 2<sup>nd</sup> COLIBRI campaign; neutron noise relative amplitude (left) and phase (right).**

## 5.9 Sensitivity analysis of the CORE SIM+ model

A sensitivity analysis is carried out to estimate the relative importance of the input and modeling parameters in the output uncertainty associated with CORE SIM+ simulations. This is helpful to understand which input parameter is responsible for the output uncertainties under the current computational scheme. As an example, experiment 13 from the 1<sup>st</sup> COLIBRI campaign is considered.

### 5.9.1 Methodology for sensitivity analysis – sensitivity indices

In the current work, Pearson's Correlation Coefficient (PCC) is selected for sensitivity measures because of its simplicity. Given two variables and a set of possible values for each of them, PCC is a measure of the linear correlation between the two variables and is equal to the covariance of the two variables divided by the product of their standard deviations [40-41]. Since the uncertainty estimated in section 5.8 are small, the correlation may be assumed to behave linearly, and the application of PCC may be reasonable.

Additionally, a Z test is carried out in order to determine whether the obtained correlation coefficients are statistically significant. Here, we set a significance level, which is a threshold of probability to accept or reject the null hypothesis. Following a general guideline, the significance level is taken as 5%, that leads to a critical value equal to 0.06 for a sample size of 1000 according to the Z test [42-43]. If the absolute value of the calculated PCC based on 1000 samples is larger than 0.6, the null hypothesis that the input and output variables are 'correlated', can be not true with a 5% probability, which gives a level of confidence of 95%.

As a last step, the calculated coefficient is squared to represent the 'sensitivity index', which expresses what fraction of the variation of the dependent variable is explained by the variation of the independent variable [44].

### 5.9.2 Methodology for sensitivity analysis – grouping parameters

A methodology is used to measure the effect of a large number of correlated input nuclear parameters efficiently, through the determination of a multiple correlation coefficient [45]. Accordingly, this multiple correlation coefficient for a group of input nuclear parameters ( $X_{(1)} = (X_1, \dots, X_k)$ ) with respect to an output  $Y$  is calculated as:

$$R_{(1)}^2 = (r_p(Y, X_1), \dots, r_p(Y, X_k)) \Sigma_{X_{(1)}}^{-1} (r_p(Y, X_1), \dots, r_p(Y, X_k))^T \quad (27)$$

where  $r_p(Y, X_i)$  is the correlation coefficient between  $Y$  and  $X_i$ , and  $\Sigma_{X_{(1)}}^{-1}$  is the inverse of the Variance-Covariance Matrix (VCM).

### 5.9.3 Results for the CORE SIM+ simulation of a COLIBRI experiment

A sensitivity analysis is performed using the CORE SIM+ model of experiment 13 from the 1<sup>st</sup> COLIBRI campaign (see sections 5.2 and 5.7).

The parameters listed in Table 15 are divided in three groups, i.e., the group of nuclear parameters (which may be correlated, see section 5.9.2), the group of design and operating parameters (which may not be correlated), and the group of noise source data (not correlated). The analysis aims to determine the most influential group on the output quantities such as the APSD amplitude for the generic detector  $i$  divided by the amplitude of the CPSD with respect to detector 5, and the phase of the CPSD with respect to detector 5.

Two different approaches are used. One approach is simplified and compares the relative size of the uncertainties propagated from the three different groups to the results. Here, the uncertainty is determined by the simultaneous perturbation of the parameters which belong to a given group, while the parameters included in the other groups are kept fixed, equal to their nominal values. The second approach measures the exact amount of contribution of each group to the neutron noise by means of the sensitivity index.

In the simplified approach, the uncertainty analysis is based on 1<sup>st</sup> order Wilks' formula for two-sided limits. Figure 70 show the different contributions to the uncertainty of the calculated noise at the locations of the detectors. The group of design and operating parameters plays a negligible role. For detectors 8 and 6 (near the noise source), the output uncertainties are strongly driven by the group of noise source data and the group of nuclear data. For the other detectors, the uncertainty associated with the amplitude is more affected by the nuclear data than the noise source data, while the uncertainty of the phase is more affected by the noise source data (however, this contribution is comparable to the contribution from the nuclear data).

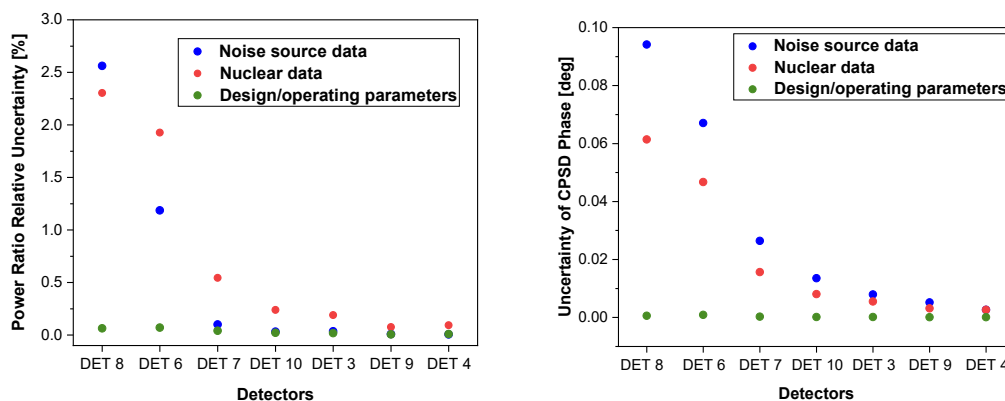


**Figure 70: Experiment 13 in the 1st COLIBRI campaign; comparison of neutron noise uncertainties obtained from the different groups of input and modelling parameters (left: APSD amplitude, and right: CPSD phase).**

In the next step of the analysis, sensitivity indices are estimated to identify the most contributing single parameters. Based on the outcome of the simplified approach, the design and operating parameters are excluded. The analysis is performed with 1000 data sets, which are obtained by the simultaneous perturbation of nuclear data and noise source data. Figure 71 shows the calculated sensitivity indices of seven parameters: the nuclear data for the isotopes  $^1\text{H}$ ,  $^{16}\text{O}$ ,  $^{235}\text{U}$  and  $^{238}\text{U}$  and the three noise source data, i.e., the oscillating amplitude, the oscillating frequency, and the location of the noise source. In the case of the noise amplitude, the location of the noise source is the most influential parameter close to the noise source (detectors 8 and 6). When the detectors are located further from the noise source, the effect of the location of the noise source becomes negligible and the nuclear data related to  $^{235}\text{U}$  and  $^{238}\text{U}$  are the most dominant parameters. In the case of the phase, a similar behavior with respect to the distance of the detectors to the noise source is found. For detectors 8 and 6, the location of the noise source has a dominant effect. For the other detectors, the oscillating frequency is the most important parameters.

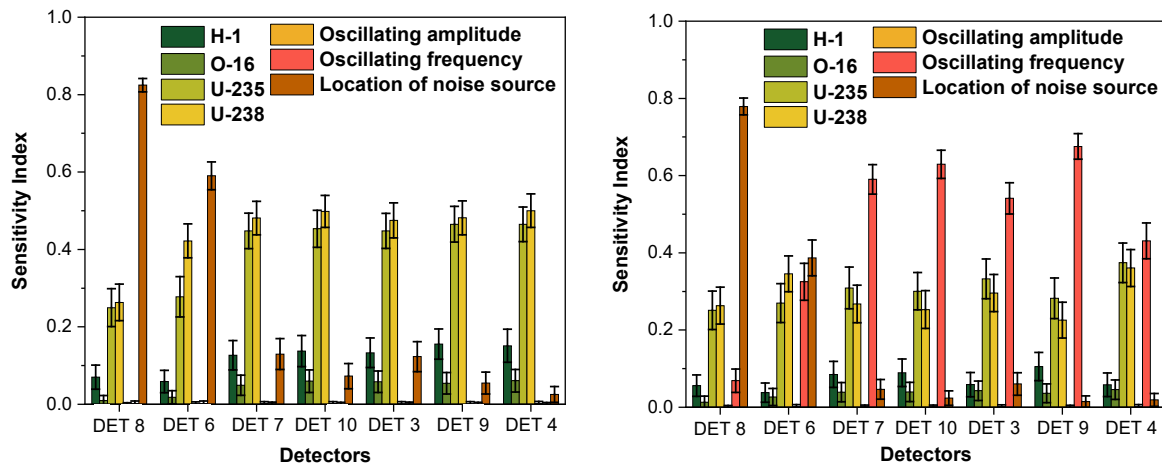


**Figure 71: Experiment 13 in the 1st COLIBRI campaign; sensitivity indices and the 95% confidence intervals between the noise source data and the noise APSD amplitude (left) and CPSPD phase (right) at the detector locations.**

## 6 Conclusions

Models for various solvers have been developed to simulate the neutron noise experiments carried out in the research reactors AKR-2 and CROCUS. The results calculated with these models have been compared with the neutron noise estimated from the measurements.

Experiments from the neutron noise campaigns at AKR-2 have been simulated using the diffusion-based solver CORE SIM+ and the stochastic solver developed by KU within the MCNP code. For the experiments with a rotating absorber, the neutron noise amplitudes predicted with MCNP and estimated from the measurements follow similar trends. For the experiments with a vibrating absorber, significant differences are found between measurements and calculations in the first campaign, while the neutron noise amplitudes obtained from the measurements and the MCNP calculation are more consistent in the second campaign. The results calculated with the solver CORE SIM+ suggest that diffusion theory may be adequate to predict the neutron noise in the AKR-2 experiments when the spatial variation of the neutron noise is not too strong.

COLIBRI experiments, in which neutron noise is induced by oscillating fuel rods in CROCUS, have been simulated using the Monte Carlo code TRIPOLI-4®, the deterministic transport code APOLLO-3®, the discrete ordinates solver NOISE-SN, the diffusion-based solver CORE SIM+, the diffusion-based solver FEMFFUSION, the diffusion-based code PARCS, and the solver FEMFFUSION-SP3 (based on the SP3 approximation). The solvers can predict a behaviour of the neutron noise amplitude that resembles the behaviour reconstructed from the signals of the detectors. However, discrepancies between calculations and measurements are found close to neutron noise sources, which require further investigations.

An uncertainty and sensitivity analysis has been performed using the solver CORE SIM+. Uncertainties associated with input and modelling parameters have been propagated to the output quantities of interest and the uncertainty for the calculated neutron noise has been quantified. The uncertainty for the neutron noise calculated in the CORE SIM+ simulations of the AKR-2 experiments is relatively small. The results obtained from the simulations of the COLIBRI experiments show that the calculated neutron noise is affected by larger uncertainties at locations that are closer to the neutron noise source. The sensitivity analysis based on the CORE SIM+ simulation of a COLIBRI experiment in CROCUS shows that the most influential parameters depend on the spatial position within the reactor core. The uncertainty in the location of the noise source plays a dominant role in the prediction of the neutron noise near the noise source, the uncertainty in nuclear data is more important when the neutron noise is taken far from the noise source, and the uncertainty in the frequency of the noise source affects mainly the neutron noise phase far from the noise source.



## 7 References

- [1] C. Demazière, P. Vinai, M. Hursin, S. Kollias and J. Herb, "Overview of the CORTEX project," in Proc. Int. Conf. Physics of Reactors– Reactor Physics paving the way towards more efficient systems (PHYSOR2018), Cancun, Mexico, (April 2018).
- [2] P. Stulik et al., CORTEX D3.3: Development of advanced signal processing techniques and evaluation results, 2019.
- [3] S. Kollias et al., CORTEX D3.4: Development of machine learning techniques and evaluation of analysis results, 2019.
- [4] G. Alexandridis et al., CORTEX D4.4: Results of the application and demonstration calculations, 2020.
- [5] A. Vidal-Ferrándiz et al., CORTEX D1.3: Modelling of the neutron flux response to vibrating fuel assemblies, 2020.
- [6] P. Vinai et al., CORTEX D1.4: Development and comparisons of higher-order solvers for reactor noise analysis, 2021.
- [7] V. Lamirand et al., CORTEX D2.1: Experimental report of the 1st campaign at AKR-2 and CROCUS, 2018.
- [8] V. Lamirand et al., CORTEX D2.2: Experimental report of the 2nd campaign at AKR-2 and CROCUS, 2021.
- [9] V. Lamirand et al., CORTEX D2.4: Experimental report of the 3rd campaign at AKR-2 and CROCUS, 2021.
- [10] A. Mylonakis, P. Vinai and C. Demazière, "CORE SIM+: A flexible diffusion-based solver for neutron noise simulations," Annals of Nuclear Energy, 155, 1 June 2021, 108149.
- [11] A. Mylonakis, P. Vinai, and C. Demazière. Numerical solution of two-energy-group neutron noise problems with fine spatial meshes. Annals of Nuclear Energy, 140, 107093, 2020.
- [12] A. Mylonakis, P. Vinai, and C. Demazière. Two-level multigrid preconditioning of a neutron noise diffusion solver. In International Conference on Mathematics and Computational Methods applied to Nuclear Science and Engineering - M&C, 2019.
- [13] A. Vidal-Ferrándiz, A. Carreño, D. Ginestar and G. Verdú. "Repository of FEMFFUSION: a finite an open finite element code for nuclear reactor modelling" <https://www.femffusion.imm.upv.es> (2020).
- [14] A. Vidal-Ferrándiz, A. Carreño, D. Ginestar, C. Demazière and G. Verdú, "A time and frequency domain analysis of the effect of vibrating fuel assemblies on the neutron noise," Annals of Nuclear Energy, 137, 107076 (2020).
- [15] Purdue University, Purdue Advanced Reactor Core Simulator, (2014).  
<https://engineering.purdue.edu/PARCS>
- [16] A. Rouchon, A. Zoia and R. Sanchez, "A new Monte Carlo method for neutron noise calculations in the frequency domain," Annals of Nuclear Energy, 102, April 2017, Pages 465-475 (2017).
- [17] A. Rouchon, W. Jarrah and A. Zoia, "The new neutron noise solver of the Monte Carlo code TRIPOLI-4®," Proceedings of Mathematical and Computational Methods Applied to Nuclear Science and Engineering (M&C 2019), Portland, OR, USA, August 25–29, 2019, pp. 332-341 (2019).
- [18] T. Yamamoto, "Monte Carlo method with complex-valued weights for frequency domain analyses of neutron noise," Annals of Nuclear Energy, 58, August 2013, Pages 72-79 (2013).
- [19] T. Yamamoto, "Implementation of a frequency-domain neutron noise analysis method in a production-level continuous energy Monte Carlo code: Verification and application in a BWR," Annals of Nuclear Energy, 115, February 2018, Pages 494-501 (2018).
- [20] A. Gammicchia, S. Santandrea, I. Zmijarevic, R. Sanchez, Z. Stankovski, S. Dulla and P. Mosca, "A MOC-based neutron kinetics model for noise analysis," Ann. Nucl. Energy, vol. 137, 2019.
- [21] A. F. Henry, Nuclear-Reactor Analysis, Cambridge (MA): The MIT Press, 1986.
- [22] S. Dulla, E. H. Mund and P. Ravetto, "The quasi-static method revisited," Prog. Nucl. Energ., vol. 50, no. 8, pp. 908-920, 2008.

- [23] A. Brighenti, S. Santandrea, I. Zmijarevic and Z. Stankovski, "Validation of a time-dependent deterministic model for neutron noise on the first CROCUS experimental measurements," submitted to Ann. Nuc. Ener.
- [24] S. Santandrea, L. Graziano, I. Zmijarevic and B. Vezzoni, "A Leakage synthetic algorithm and a Krylov approach for thermal iterations in APOLLO3 code in support to industrial applications," submitted to ANS M&C 2021 Conference.
- [25] H. Yi, P. Vinai and C. Demazière, "On neutron noise simulations using the discrete ordinates method," Annals of Nuclear Energy, Volume 164, 15 December 2021, 108570 (2021).
- [26] V. Lamirand, F. Vitullo, K. Ambrožič, O. Pakari, L. Braun, and D. Godat, CORTEX D2.3: Development of fibre-based neutron scintillators, 2021.
- [27] J. Leppänen, M. Pusa, T. Viitanen, V. Valtavirta, and T. Kaltiaisenaho, The Serpent Monte Carlo code: Status, development and applications in 2013. Ann. Nucl. Energy, 82, 142-150, 2013.
- [28] C. Demazière, V. Dykin, K. Jareteg, "Development of a point-kinetic verification scheme for nuclear reactor applications", Journal of Computational Physics, 339, 396-411, 2017.
- [29] M. Kloos and E. Hofer, "SUSA - PC, a personal computer version of the program system for uncertainty and sensitivity analysis of results from computer models, version 3.2," user's guide and tutorial, Gesellschaft für Anlagen- und Reaktorsicherheit, Garching, Germany (1999).
- [30] N. W. Porter, "Wilks' Formula Applied to Computational Tools: A Practical Discussion and Verification," Sandia National Laboratories Report, SAND2019-1901J (2019).
- [31] S. Yum et al., CORTEX D1.1: Methodology for uncertainty and sensitivity analysis, 2019.
- [32] A. Rais, Performance assesement of a 3-D steady-state and spatial kinetics model for the CROCUS reactor. Ph.D. thesis, École Polytechnique Fédérale de Lausanne (2017).
- [33] I. Pazsit and J. Karlsson, "On the perturbative calculation of the vibration noise by strong Absorbers," Annals of Nuclear Energy, volume 24(6), pp. 449 – 466, 1997.
- [34] C. Demazière and A. Dokhane, CORTEX D1.3: Description of scenarios for the simulated data, 2019.
- [35] A. Zoia, A. Rouchon, B. Gasse, C. Demazière, P. Vinai, "Analysis of the neutron noise induced by fuel assembly vibrations," Annals of Nuclear Energy, 154, pp. 108061 (2021).
- [36] D. L. Hetrick, Dynamics of Nuclear Reactors, The University of Chicago Press, 1971.
- [37] A. G. Mylonakis, C. Demazière, P. Vinai, V. Lamirand, A. Rais, O. Pakari, P. Frajtag, D. Godat, M. Hursin, G. Perret, A. Laureau, C. Fiorina and A. Pautz, "CORE SIM+ simulations of COLIBRI fuel rods oscillation experiments and comparison with measurements," in PHYSOR 2020: Transition to a Scalable Nuclear Future, Cambridge, United Kingdom, March 29th-April 2nd, 2020.
- [38] G. R. Keepin, Physics of Nuclear Kinetics, Addison-Wesley Publishing Co., 1965.
- [39] OECD/NEA-4440, "Benchmark on the kinetics parameters of the CROCUS reactor," Physics of Plutonium Recycling, Volume 9, 2007. ISBN 978-92-64-99020-3.
- [40] W. J. Conover, "Practical Nonparametric Statistics," 3<sup>rd</sup> ed., John Wiley & Sons, New York (1980).
- [41] SPSS Tutorials: Pearson Correlation, URL: <https://libguides.library.kent.edu/SPSS>
- [42] P. H. Ramsey, "Critical Values for Spearman's Rank Order Correlation," Journal of Educational Statistics, **14(3)**, pp.245-253 (1989).
- [43] S. Kajuri, "Application of Hypothesis Testing and Spearman's rank correlation coefficient to demystify Suicides worldwide," (2018) URL <https://towardsdatascience.com/application-of-hypothesis-testing-and-spearman-s-rank-correlation-coefficient-to-demystify-b3a554730c91>
- [44] A. G. Bluman, "Elementary Statistics: A Brief Version," 7<sup>th</sup> Edition, New York: McGraw-Hill (2009).
- [45] M. Hursin et al., "Determination of Sobol Sensitivity Indices for Correlated Inputs with SHARK-X," PHYSOR 2018, Cancun, Mexico, April 22-26 (2018).